STUDYING THE FUNCTION OF LONG-RANGE PROJECTING VIP-EXPRESSING NEURONS IN THE FACIAL MOTOR NUCLEUS

Nima Raman

Thesis submitted to the University of Ottawa

in partial fulfillment of the requirements for the

Doctor of Philosophy in Neuroscience

February 2026

Department of Cellular and Molecular Medicine

Faculty of Medicine

University of Ottawa

ABSTRACT

The vestibular system is critical for regulating balance and postural maintenance in many vertebrates. The medial vestibular nuclei (MVN) in the brainstem are known to serve as a hub for receiving and relaying sensory information that is important for vestibular function. While considerable research has been dedicated to understanding how MVN regulate gaze stabilization and spatial orientation/perception, little is known about its connections with other brainstem nuclei that play critical roles for fine-tuning posture and balance. In this thesis, we identified a population of vasoactive intestinal peptide (VIP)-expressing neurons in the facial motor nucleus (FMN) of the brainstem that provide long-range inputs to MVN. Lower motoneurons in FMN have been shown to mediate specific orofacial and vibrissal muscle movements, but these FMN^{VIP} neurons have never been described. We employed advanced viral tracing methods, *in vivo* fiber photometry, and cell-type specific ablation and chemogenetic manipulations to study whether and how FMN^{VIP} neurons contribute to vestibular-mediated balance maintenance. Ablation or acute silencing of FMN^{VIP} neurons altered the animals' balance performance without affecting their gaze stabilization. Intriguingly, we found that these FMN^{VIP} neurons are cholinergic, rather than glutamatergic or GABAergic, and using anterograde monosynaptic labeling, we further identified that the major postsynaptic targets of FMN^{VIP} neurons are the GABAergic neurons in MVN. *In vivo* Ca^{2+} imaging of FMN^{VIP} neurons and ACh sensor recordings in MVN demonstrated that FMN^{VIP} neurons are activated only when the animal's balance is challenged, and they release ACh to modulate MVN neuronal activity and fine-tune body posture for balance maintenance. Lastly, cell-type specific rabies tracing revealed that the major input regions to FMN^{VIP} neurons arise from the reticular formation, a phylogenetically old brain structure that is known to regulate balance. Altogether, the work from

this thesis unveils a new brainstem circuit pathway that bridge the reticular with vestibular nuclei to regulate balance and postural maintenance.

Table of Contents

Acknowledgement

I would like to begin by expressing my deepest gratitude to my supervisor, Dr. Simon Chen, for his exceptional mentorship, intellectual generosity, and unwavering support throughout this journey. Working under your supervision has been a privilege. Your rigor, and high standards shaped not only my scientific thinking, but also my approach to scholarship and integrity. I am profoundly grateful for the trust you placed in me and for the freedom you gave me to grow into an independent scientist.

I am sincerely grateful to the members of my thesis advisory committee, Dr. Jean-Claude Béïque, Dr. Tuan Bui, and Dr. Maxime Rousseaux, for their thoughtful guidance, critical insight, and constructive feedback at every stage of this work. Your questions consistently sharpened my thinking and strengthened this thesis. Thank you for your time, generosity, and commitment to my development.

As Khalil Gibran wrote, “Your children are not your children… They come through you but not from you… You may strive to be like them, but seek not to make them like you.” With that in mind, I owe a special debt of gratitude to my parents, Farzad Raman and Mina Hosseinzadeh Mehdikhani. You gave me far more than encouragement; you gave me perspective. You taught me to look beyond what is familiar, to resist the ordinary, and to trust motion over comfort. Like a bow that does not cling to the arrow but releases it with purpose, you gave me direction, tension, and faith, and then let me fly toward distances you had prepared me to reach. Everything I am able to pursue rests on the values you instilled in me.

My deepest thanks go to my best friend and partner, Dr. Narges Atrak. Your patience, strength, and quiet resilience carried me through years of distance, uncertainty, and absence. You stood beside me even when “beside” meant across borders and time zones. Thank you for believing in this path when it was difficult, for tolerating its costs, and for being a constant source of grounding, love, and clarity. This work is inseparable from your presence in my life. Love you to the moon and back my JoJo ~~~

I am also grateful to the colleagues, collaborators, and friends who made this journey intellectually rich and personally meaningful. Your discussions, encouragement, and companionship turned long days and late nights into something shared and human. This thesis reflects not only individual effort, but also a community that made learning generous and discovery joyful.

Contributions

All experiments in this thesis were designed and performed by the author under the supervision of Dr. Simon Chen, who provided scientific guidance, mentorship, and critical feedback throughout. The author wrote the thesis, which were revised with edits and comments from Dr. Chen.

Specific contributions were as follows. Nathaniel Jones wrote MATLAB code to compute body-part angle metrics for HBT traversal. Matthew Loukine wrote MATLAB code to compute body-part angle metrics for HBT perturbation. Hritvic Chaudhary performed image analysis quantifying FMN-taCasp ablation efficiency, and Chloe Logan conducted whole-brain rabies image analysis. Jayda Felix helped to set up fiber photometry and prepared the photometry trace analysis pipeline. Dr. Candice Lee shared statistical approaches. Dr. Xuming Yin assisted with initial identification of FMN ^{VIP} neurons, and Liwen Cai managed mouse colonies. Dr. Jungwo Yang prepared AAV plasmid packaging, and Irina Morozov trained DeepLabCut, implemented Arduino TTL synchronization, and made HBT apparatus setup. Dr. Alex Laliberte (Dr. Tuan Bui's lab) trained the authors in spinal cord dissections. Yingtian He (Dr. Baohua Liu's lab, University of Toronto Mississauga) performed OKR experiments for FMN and MVN ablation. Dr. Julie Lefebvre (The Hospital for Sick Children, Toronto) shared TRACR viral tools and enabled pilot testing in our system.

Abbreviation List

1. Brain Regions

Abbreviation	Full name
AOS	Accessory optic system
BNST	Bed nucleus of the stria terminalis
BötC	Bötzinger complex, brainstem respiratory nucleus
CVLM	Caudal ventrolateral medulla
DL	Dorsolateral facial motor nucleus (FMN) subnucleus
DpMe	Deep mesencephalic nucleus
DRN	Dorsal raphe nucleus
DVN / SpVe	Descending (spinal) vestibular nucleus
FMN	Facial motor nucleus
Gi	Gigantocellular reticular nucleus
IRt	Intermediate reticular nucleus
LC	Locus coeruleus
LVN / LVe	Lateral vestibular nucleus / Deiters' nucleus
MAe	Medial amygdala
MARN	Magnocellular reticular nucleus
MdD	Dorsal medullary reticular formation
MVN / MVe	Medial vestibular nucleus
OP2	Parietal operculum area OP2
PARN	Parvicellular reticular nucleus
PCRt	Parvocellular reticular nucleus (historical grouping of PARN + MARN)
PIVC	Parieto-insular vestibular cortex
PMRF	Pontomedullary reticular formation
S2	Secondary somatosensory cortex

SpC	Spinal trigeminal nucleus (general complex label)
SpV	Spinal trigeminal nucleus (general term)
SpVIr	Spinal trigeminal nucleus, interpolaris, rostral division
SpVO	Spinal trigeminal nucleus, oral division
SuVe / SVN	Superior vestibular nucleus
V4	Floor of the fourth ventricle
VN	Vestibular nuclei complex (MVN, LVN/LVe, SVN/SuVe, DVN/SpVe)
VP (thalamus)	Ventroposterior thalamic nucleus
VPL	Ventral posterolateral thalamic nucleus
VST	Vestibulospinal tracts

2. Tracts & Reflexes

Abbreviation	**Full name**
APRs	Automatic postural responses
MVST	Medial vestibulospinal tract
NREM	Non-rapid eye movement sleep
OKR	Optokinetic reflex
REM	Rapid eye movement sleep
SEP	Smooth pursuit eye movements
VCR	Vestibulocollic reflex
VOR	Vestibulo-ocular reflex
VRT	Vestibular rehabilitation therapy
VSR	Vestibulospinal reflex
VVOR	Visually enhanced vestibulo-ocular reflex

3. Cell Populations & Physiological Classes

Abbreviation	Full name
ES	Eye-movement-sensitive neuron class in MVN
EH	Eye-head-sensitive neurons
FMN^{VIP}	VIP-expressing neurons in the facial motor nucleus
FTN	Flocculus-target neurons
PVP	Position-vestibular-pause sensitive neurons
VO	Vestibular-only neuron class in MVN
vMN(s)	Vibrissa motoneuron(s)

4. Neurotransmitters, Peptides, Receptors & Molecular Markers

Abbreviation	Full name
ACh	Acetylcholine
AChE	Acetylcholinesterase
Ca^{2+}	Calcium ion
ChAT	Choline acetyltransferase
GABA	γ-Aminobutyric acid
GABAA	GABA-A receptor
GABAB	GABA-B receptor
GAD1 / GAD67	Glutamate decarboxylase 1 / 67 kDa isoform
M2	Muscarinic acetylcholine receptor subtype M2
M3	Muscarinic acetylcholine receptor subtype M3
VAChT	Vesicular acetylcholine transporter
VGAT	Vesicular GABA transporter
VGLUT	Vesicular glutamate transporter family
VIP	Vasoactive intestinal peptide
VPAC1	Vasoactive intestinal peptide receptor type 1
VPAC2	Vasoactive intestinal peptide receptor type 2

5. Viral Vectors, Constructs & Rabies Components

Abbreviation	Full name
AAV	Adeno-associated virus
EnvA	Envelope A glycoprotein for rabies pseudotyping
EnvA-RVΔG-mCherry	EnvA-pseudotyped glycoprotein-deleted rabies expressing mCherry
oG	Optimized rabies glycoprotein
pAAV	Plasmid AAV backbone
RVΔG	Glycoprotein-deleted rabies virus
TVA	Tumor virus receptor A
WPRE	Woodchuck hepatitis virus post-transcriptional regulatory element

6. Sensors, Reporters & Indicators

Abbreviation	Full name
GCaMP8m	Genetically encoded calcium indicator, variant 8m
GRAB-ACh3.0	GPCR-activation-based fluorescent acetylcholine sensor

7. Chemogenetics & Pharmacology

Abbreviation	Full name
hM4Di	Human M4 muscarinic inhibitory DREADD
JHU	JHU37160, DREADD agonist
PG97-269	Selective VPAC1 receptor antagonist
PG99-465	Selective VPAC2 receptor antagonist

8. Behavioral Tasks, Assays & Metrics

Abbreviation	Full name
HBT	Horizontal beam test
OKR	Optokinetic reflex
ROI	Region of interest
Rotarod	Accelerating rotarod assay
SF	Spatial frequency
SMI	Spiral Motion Intensity
TF	Temporal frequency
VPT	Vertical pole test

9. Coordinate Systems, Hardware & Recording Setup

Abbreviation	Full name
AP	Anterior-posterior axis
C5	Cervical spinal segment 5
DV	Dorsoventral axis
EB	End-of-beam landmark
H	Head landmark
IR	Infrared
LED	Light-emitting diode
ML	Mediolateral axis
S	Sacrum landmark
SB	Start-of-beam landmark
TTL	Transistor-transistor logic trigger

10. Histology, Reagents & Tissue Processing

Abbreviation	Full name
BSA	Bovine serum albumin

HRP	Horseradish peroxidase
OCT	Optimal cutting temperature compound
PBS	Phosphate-buffered saline
PFA	Paraformaldehyde

11. Software, Frameworks

Abbreviation	**Full name**
CCFv3	Allen Mouse Brain Common Coordinate Framework, version 3
DLC	DeepLabCut markerless pose estimation toolkit
ilastik	Machine-learning toolkit for image segmentation
MATLAB	Numerical computing environment (MathWorks)
Nutil	Atlas-based quantification utility
QuickNII	Atlas registration software
VisuAlign	Atlas alignment refinement tool

12. Signal Processing & Statistical Terms

Abbreviation	**Full name**
MAD	Median absolute deviation
trapz	MATLAB trapezoidal numerical integration function
ΔAUC	Delta area under the curve
ΔF/F	Change in fluorescence over baseline
ΔPeak	Delta peak amplitude

CHAPTER 1: INTRODUCTION AND LITERATURE REVIEW

1. Why balance matters

Most human tasks rely on continuous adjustment of sensory inputs to coordinate posture, balance, and self-orientation (1). Imagine a person that is walking across a river on a shaky narrow tree log. In this situation, the brain combines somatosensory signals from the feet about how narrow the support surface is, vestibular inputs about head motion and gravity as the body moves on the unstable log, and visual information about the distance to the opposite bank. If the log moves unexpectedly, the postural system makes compensatory balance responses to avoid a fall (1). These inputs are primarily integrated in brainstem circuits and the cerebellum. There are two foundational brainstem systems for balance: the reticular and vestibular systems. Reticular control is organized around the pontomedullary reticular formation (PMRF) in the pons and medulla (2,3). Vestibular control is mediated by the vestibular nuclei (VN) in the dorsolateral medulla (4,5). Together, these systems provide core descending drive to the spinal cord to keep the body ready to respond to balance perturbations. Cerebellar circuits fine-tune the magnitude (gain) and the timing of postural and locomotor commands, particularly during anticipatory and predictive balance control (6,7). Within the spinal cord, premotor interneuron networks integrate the descending commands with local sensory feedback to generate the final muscle activation pattern, which motoneuron pools then relay to muscles (8).

The vestibular system provides the primary sensory drive for balance and postural control (9,10). Otolith organs encode head tilt and linear acceleration relative to gravity, whereas the semicircular canals encode angular head velocity. Their signals converge in VN, where neurons in the medial and superior regions integrate vestibular inputs with proprioceptive feedback from neck and body sensors. As a result, VN activity reflects head and body motion rather than a single sensory modality (11–13). These neurons encode the direction and magnitude of self-motion, defining the postural error that must be corrected when information

about head and body position is mismatched. When posture is disturbed, VN neurons provide excitatory drive via vestibulospinal tracts (VST) to axial and proximal extensor motoneurons and through vestibulo-reticular projections to premotor neurons in PMRF (5,14). These premotor neurons in PMRF are the pontomedullary reticulospinal neurons whose descending axons form the reticulospinal tract and contribute to spinal motor output. They adjust muscle tone according to behavioral state, limb loading, and surface compliance by integrating vestibular signals from VN with proprioceptive input from muscle spindles, Golgi tendon organs, and joint receptors (15,16). During perturbations, vestibulospinal pathways provide strong, directionally appropriate extensor drive to initiate rapid stabilization, while reticulospinal neurons then shape the immediate gain, timing, and multi-joint distribution of these short-latency responses across spinal motor pools (2,5,17). These brainstem circuits generate fast, automatic corrections, and cerebellar networks provide a third layer of control that adjusts their overall gain and context dependence and resolves sensory conflicts by comparing predicted self-motion with vestibular and visual inputs in the vestibulocerebellum (6,18–20). Together, the vestibular, reticular, and cerebellar systems act as a fast automatic subcortical controller for balance, providing the short-latency motion encoding and descending drive from vestibular nuclei, the synergy sequencing and gain scaling mediated by reticulospinal pathways, and the predictive calibration contributed by cerebellar circuits that together enable immediate postural stabilization. Under more steady conditions, basal ganglia and cerebellar signals refine posture and gait through reciprocal loops with cortex and brainstem, where sensory reweighting adjusts the relative influence of each cue (2,21,22). In rodents, electromyography and single-unit recordings reveal short-latency postural responses on the order of tens to hundreds of milliseconds, consistent with brainstem-spinal rather than corticospinal transmission (2,16). At slower, higher levels of posture processing, the thalamus and parieto-insular vestibular cortex integrate vestibular-nucleus output with optic flow and somatosensory feedback to form conscious estimates of verticality and self-motion that are required for later optimization of posture (23,24).

2. Multisensory integration

Henry Head described the body schema as a dynamic system in which spatial and temporal features are continuously updated (1). To maintain equilibrium and automatic posture control, the nervous system integrates many sensory modalities; each modality contributes a different part of the environmental estimate. Vestibular organs provide fast reactions to head motion, proprioceptors encode body configuration and load, and vision contributes to detailed spatial and contextual signals (9,18). The context of the behavior determines which sensory stream dominates postural control. During quiet stance on firm ground, vestibular drive is relatively low because head motion and vestibular signalling are minimal, so vision and proprioceptive cues usually dominate the small, tonic adjustments needed to maintain stance (25). On an unsteady surface, proprioceptive reliability decreases and vestibular influence increases as stance excursions grow larger. In darkness, where visual inputs are minimal, or during rapid head turns, vestibular cues take precedence because they provide short-latency signals on the order of a few milliseconds, well before slower visual feedback can contribute to coordinated trunk and limb corrections (25,26). Because no single stream is reliable in every condition, the nervous system reweights and combines them to maintain an accurate estimate of body orientation and movement (19,22). Much of this fast reweighting occurs in VN, where semicircular-canal and otolith inputs converge with proprioceptive and visual signals. A simple example is head rotation with or without accompanying body motion. When the head rotates on a stable torso, semicircular canals and neck proprioceptors signal different motions, and VN neurons increase the weight of vestibular input to represent head motion in space. When the head and body rotate together, the same canal signals are now accompanied by strong neck and trunk proprioception, and VN neurons shift their gain so that neck and body signals contribute more strongly to the motion estimate (11–13). This VN-level reweighting is mediated by local inhibitory circuitry and cerebellar Purkinje-cell input, which allows the system to distinguish head-on-body

rotation from whole-body motion and to route the appropriate postural response (27). Through such networks, the brain forms a single reliability-weighted estimate of body orientation that remains stable even when individual inputs are noisy or conflicting (1). This integrated estimate provides the sensory foundation for detecting postural errors to keep the center of mass within safe limits of balance.

3. Vestibular Afferent Coding

The vestibular sensors of the inner ear detect angular and linear acceleration (28). The semicircular canal hair cells act as directional mechanotransducers. Deflection of their stereocilia toward the tallest process, the kinocilium, depolarizes the cell and increases glutamate release onto vestibular afferent terminals, whereas deflection away from the kinocilium hyperpolarizes the cell and reduces transmitter release. This rapid synaptic transmission converts head motion into electrical signals that reach the brain within a few milliseconds (29). The afferent fibers arise from bipolar first-order vestibular neurons whose somata form Scarpa's ganglion near the inner ear. These neurons relay hair-cell signals centrally via the vestibular branch of cranial nerve VIII to the vestibular nuclear complex (VN) and flocculonodular cerebellum, with additional collaterals to the reticular formation (28,30). Primary vestibular afferents are classified as regular or irregular based on how constant their interspike intervals are. Regular fibers provide a steady signal during slow or constant head motion, whereas irregular fibers give brief, high-sensitivity responses to rapid or unpredictable movements. Together,they encode both steady and sudden head motion (31). Because of these distinct properties, regular and irregular afferents project to different subclasses of second-order neurons within VN and provide parallel streams that favor different VN functions. Within VN, neurons can be classified as type I or type II, based on their response dynamics and directional tuning. In rodents, irregular horizontal-canal afferents preferentially contact 'phasic' type I VN neurons that mediate short-latency vestibulo-ocular reflexes, whereas regular afferents target 'tonic' type II neurons that sustain posture-related

signals (5). These pairings match the fast, high-gain responses of irregular afferents to type I neurons that support rapid gaze stabilization, and the stable, low-noise encoding of regular afferents to type II neurons that provide tonic posture-related signals, allowing VN circuits to support both precise gaze control and continuous postural regulation (5,31). Importantly, vestibular afferents operate continuously. When the head is still, most vestibular afferents maintain a spontaneous resting discharge (~70-100 spikes per second), which provides a tonic baseline for encoding deviations from rest (18,32,33). During head rotation, the discharge on the ipsilateral side increases proportionally to angular velocity, while the firing on the contralateral side decreases. This push-pull organization doubles the coding range and allows the system to detect both direction and speed of motion (24). By virtue of this continuous baseline and push-pull architecture, changes in head motion are encoded almost immediately, supplying the earliest drive for reflex stabilization. These signals reach vestibular nucleus neurons within a few milliseconds and initiate the earliest corrective responses, highlighting the temporal precision of vestibular processing. Responses that emerge within about 6-10 ms after head acceleration are fast enough to generate vestibulo-ocular reflex-mediated eye movements well before visual feedback can help stabilize gaze. In behaving monkeys, single-unit recordings showed that neurons in the medial vestibular nucleus (MVN) mirror this rapid timing and fire within the same ~10 ms window during both passive and self-generated head turns in darkness (25,30). This near-instant canal to vestibular relay forms an ultrafast brainstem controller that stabilizes gaze and posture when rapid responses are required. Within parallel microcircuits, VN excitatory and inhibitory neurons integrate inputs from semicircular canals, otolith organs, neck proprioceptors, the cerebellum, and reticular pathways, allowing the vestibular nucleus to generate either graded tonic output or brief burst-like responses. These outputs drive oculomotor and spinal motor pools to stabilize gaze and balance during voluntary or unexpected movements (34).

4. Central vestibular system

The vestibular nerve projects ipsilaterally to four principal nuclei (VN), including the superior (SVN/SuVe), medial (MVN/MVe), lateral (LVN/LVe/Deiters'), and spinal/descending (DVN/SpVN) vestibular nuclei, along with smaller cell groups such as X and Y cells along the fourth ventricle in the dorsal pons and medulla (1,35). Primary ascending fibers of the eighth vestibular cranial nerve carry information from the semicircular canals and otolith organs to the SVN, MVN, and LVN, whereas additional descending vestibular fibers project to the LVN and DVN. These vestibular neurons receive convergent inputs from the inner-ear structures, cerebellum, spinal cord, and visual pathways, making them central multisensory hubs for motion and spatial orientation (36). As a group, the vestibular nuclei give rise to widespread efferent projections to oculomotor nuclei, cerebellum, reticular formation, spinal cord, and thalamus, but the density and organization of these pathways differ across individual nuclei, supporting distinct roles in gaze stabilization and postural control (37,38). Classic studies in cats and non-human primates show the rostral SVN and rostral MVN (magnocellular division of MVN) are enriched for premotor neurons of the vestibulo-ocular pathways that coordinate eye and head movements, whereas the caudal MVN (parvocellular MVN) together with LVN and DVN give rise to many of the descending vestibulospinal pathways that support posture and balance (10,17). In rodents, anatomical and genetic mapping studies point instead to an intermingled "hodological mosaic" for VN. In rodent MVN and adjoining vestibular column, neurons projecting to ocular and spinal targets arise from overlapping rhombomeric domains and are distributed along the rostro-caudal extent of the nucleus rather than forming neatly segregated columns. Within VN complex, MVN integrates canal and otolith inputs from both sides and sends bilateral commands through two main descending routes: direct vestibulospinal projections that influence neck and axial motoneurons, and indirect pathways via reticular formation neurons that give rise to reticulospinal output (39,40). Through these connections, MVN neurons help to recalibrate body posture. LVN complements this role by driving ipsilateral extensor and axial motor pools through the lateral

vestibulospinal tract (17). Distinct LVN neurons coordinate sequential phases of postural recovery after perturbation, driving an initial rapid activation of antigravity musculature followed by a brief co-activation of opposing muscle groups to restore whole-body stability (41). DVN and other caudal vestibular nuclei are strongly modulated during static tilts and rotations in vertical planes, indicating that neurons in this caudal complex are preferentially engaged by gravity-referenced changes in body orientation rather than routine steady-state control (42–44). A complementary vestibulospinal pathway arising from DVN projects to sacral segments that innervate tail muscles, and its recruitment during challenging balance conditions shows that tail motion can serve as a reactive postural strategy (45).

VN contribute to balance control through two major output pathways: ascending routes that carry information about head and body movement to the thalamus and cortex, and descending routes that send rapid balance commands from the brainstem to the spinal cord. Ascending projections from the vestibular nuclei reach the ventral posterior thalamic nuclei, which relay to cortical regions involved in vestibular function (vestibular cortical regions), including the parieto-insular vestibular cortex, posterior insula, parietal operculum, and multisensory somatosensory and parietal areas. These cortical vestibular regions, therefore, combine vestibular, visual, and somatic inputs to represent head and body motion, body orientation, and the gravitational vertical (19,46). At the descending level, vestibulospinal tracts provide a direct projection from VN to spinal interneurons and motoneurons, while VN-updated reticulospinal tracts complement the vestibulospinal pathway for postural control (2,14). For the fastest balance corrections, direct vestibular projections to the spinal cord provide the shortest-latency route, preceding the slower thalamocortical and visual pathways (2,5,17). Lesions of cortical vestibular regions, including the parieto-insular vestibular cortex and posterior insula, reliably tilt the perceived visual vertical and disturb self-orientation, yet often spare posture in the acute phase (23,47). By contrast, experimental disruption of VN function produces immediate postural ataxia and impaired compensatory responses to imbalance, underscoring the critical role of vestibular

nuclear output in the earliest stages of balance control (41,48,49). Classic lesion studies in rats show that damage to the lateral or superior vestibular nuclei causes severe postural asymmetry and complete failure on balance-beam tests. Selective optogenetic activation of glutamatergic vestibular nuclei neurons in mice likewise produces immediate and reversible postural imbalance, characterized by a markedly widened base of support (50). When vestibular function is more broadly compromised, detailed posturo-locomotor analyses on narrow beams reveal slower gait, widened stance, asymmetric weight shifts, more frequent pauses, and enlarged head-trunk oscillations (51–55). The role of vestibulospinal output is conserved across vertebrates. In larval zebrafish, targeted lesions of the vestibulospinal nucleus destabilize posture and disrupt fin-trunk coordination, demonstrating a shared balance architecture through evolution (56). These findings emphasize the hierarchical division in which cortical centers interpret movements, whereas the VN network executes the core reflexive balance responses that stabilize gaze and posture. Although second-order neurons in VN mediate automatic balance control and gaze stabilization, the organization and function of their underlying circuits remain incompletely understood (18).

4.1. The medial vestibular nuclei (MVN)

In the vestibular nuclei, MVN serves as the main hub for dynamic reflex control. MVN is distinguished by its size, cellular diversity, and breadth of connections. This vestibular complex contributes to (**a**) gaze control and stabilization, (**b**) balance and postural maintenance, and (**c**) broader vestibular-related processes such as spatial navigation, perception, memory, voluntary movement planning, and autonomic regulation (9,57). MVN contains inhibitory and excitatory interneurons plus long-range projection neurons, enabling early brainstem computations that transform head-motion signals into coordinated ocular and postural commands (58,59). Semicircular canal afferents, especially from the horizontal canals, dominate MVN, while otolith-sensitive second-order neurons are concentrated mainly in the lateral and descending VN. This bias reflects MVN's

principal function in processing angular head velocity, which directly triggers reflexes that keep the eyes and head steady during movement. Canal-driven MVN neurons descend bilaterally through the medial vestibulospinal tract (MVST) to cervical and upper-thoracic segments for head and neck stabilization and axial muscle activity (40,60,61). Furthermore, through projections to the oculomotor, trochlear, and abducens nuclei, MVN forms a core relay for stabilizing gaze during head motion. Reciprocal links between MVN and the cerebellar flocculus, nodulus, and fastigial nucleus continuously calibrate reflex gain and phase so that eye, head, and body movements can remain precisely aligned (2,9). Electrophysiological and tracing studies in rodents and cats show MVN activity rises during unpredictable balance perturbations or active gaze shifts and decreases during steady, self-generated locomotion (62). In summary, MVN integrates multiple sensory inputs, and this serves as the mechanistic foundation for MVN's contributions to everyday functions such as balance and gaze control.

4.1.1. Balance maintenance by MVN

Vestibular end organs provide the first and most precise estimate of head motion, and their afferents target MVN and nearby nuclei that transform these signals into descending motor commands. MVN neurons project bilaterally to the spinal cord through MVST, which travels in the medial longitudinal fasciculus to the medial ventral horn of cervical and upper-thoracic premotor and motor pools. MVST forms a short two- to three-synapse chain that mediates the vestibulocollic reflex (VCR), and MVN neurons also contribute to a lesser extent to components of the vestibulospinal reflex (VSR) (10,63–65). Almost immediately after a perturbation, VCR provides the first line of balance defense by stabilizing the head and upper trunk. Since the head is the central site of detection for the rest of the body, this stabilization sets a reliable spatial reference frame that the body can use for postural adjustments. Vestibulospinal reflex (VSR) pathways run in parallel to redistribute muscle tone throughout the body, particularly in the trunk and lower limbs (63,66–69). Within MVN

microcircuits, glutamatergic neurons deliver excitatory vestibular drive to the spinal cord and provide the main descending command for VCR and VSR. Consistent with this role, selective optogenetic stimulation of VGluT2-expressing vestibular nucleus neurons, which include MVN glutamatergic cells, induces immediate and reversible posturo-locomotor imbalance (50). MVN is also heavily embedded in the vestibular commissural inhibitory network. This system links the two hemispheres and is crucial for keeping vestibular drive symmetric and for vestibular compensation after unilateral damage. Functionally, the inhibitory network shapes and rebalances VCR and VSR outputs rather than driving a new reflex. A PV-expressing GABAergic population in MVN has been shown to mediate commissural rebalancing after unilateral vestibular loss. Chemogenetic activation of this group accelerated postural recovery, whereas its inhibition prolonged imbalance and delayed compensation (70).

MVN's wide connectivity allows complex balance computations within this central hub. Vestibulocerebellar Purkinje cells, particularly those in the flocculus, nodulus, and uvula, provide GABAergic inhibition to the vestibular nuclei, including MVN. MVN in turn projects back to the cerebellar cortex and to the fastigial nucleus. Fastigial neurons then project to vestibular and reticular nuclei and onward to the spinal cord. Through these closed-loop connections, the cerebellum tunes the gain and timing of VCR outputs and helps coordinate multi-segment posture, refining the hard-wired vestibulospinal pathways (71,72). In a complementary ascending pathway, vestibular signals from MVN reach the ventral posterolateral (VPL) and ventroposterior (VP) thalamic nuclei, where thalamocortical neurons reshape the input to give a cleaner, less noisy estimate of how the head is moving in space (self-motion). This refined motion signal is then relayed to cortical vestibular regions (73). A distributed cortical network contributes to vestibular processing, with the parieto-insular vestibular cortex (PIVC) and posterior insular area (OP2) forming core hubs that connect to secondary somatosensory cortex (S2) and parietal areas 2v, 3a, and the ventral intraparietal area (VIP). These visuovestibular regions project to premotor and motor-related parietal fields, where integrated self-

motion and orientation signals shape motor planning and attention (74–76). Cortical outputs that influence posture descend mainly from premotor and primary motor cortex (M1) via the corticoreticular pathway (CRP) to PMRF. Reticulospinal neurons project bilaterally to axial and proximal limb motor pools and work in parallel with vestibulospinal pathways to support balance and gait (14,77–79). In parallel, neurons in MVN and other VN project to medial zones of the PMRF that contain reticulospinal neurons, forming a vestibulo-reticulo-spinal pathway that relays vestibular signals to spinal interneurons and motoneurons alongside the direct vestibulospinal tracts (5,63,80). PMRF neurons also project back to MVN and other VN, creating a reciprocal vestibulo-reticulo-vestibular loop that adjusts vestibular neuron gain and shapes VCR and VSR output (81–83). On an unstable surface or after a perturbation, MVN-driven VCR first stabilizes the head and upper trunk. VSR then stiffen axial and extensor synergies to generate early-latency automatic postural responses (APRs), while the thalamus relays processed vestibular signals to cortical vestibular areas. Through CRP and reticulospinal projections, cortical networks reweight gains, select postural strategies, and add goal-directed components that refine voluntary adjustments to optimize posture (84,85).

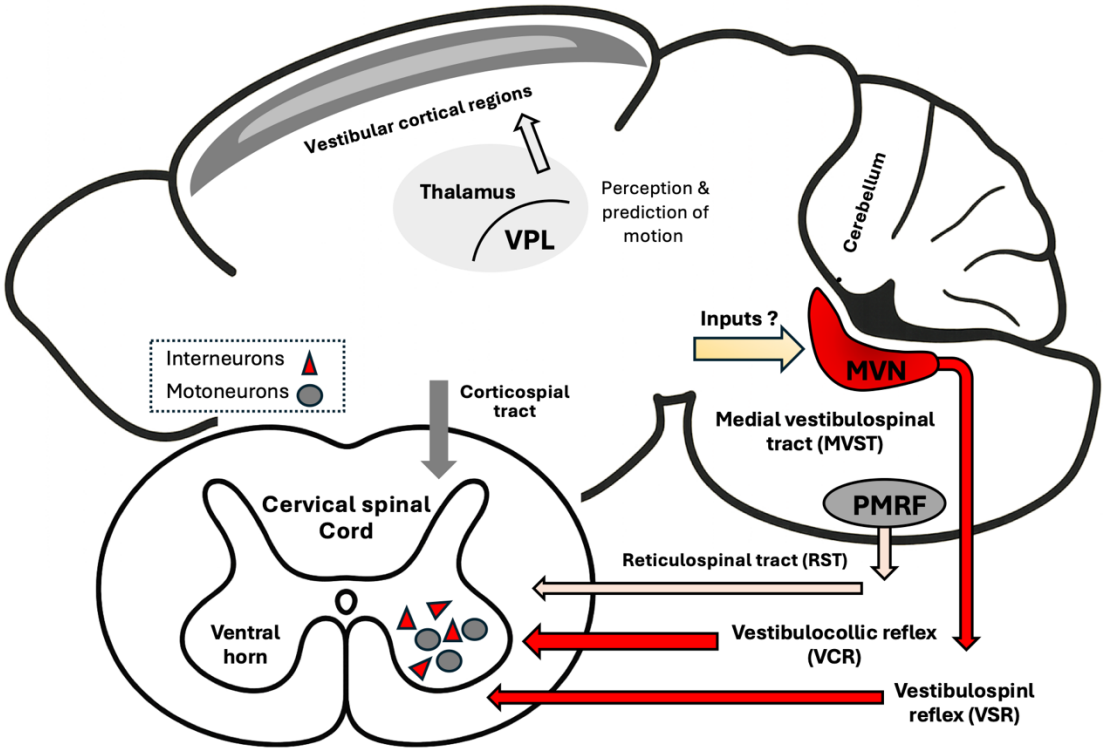

Figure I. MVN vestibulospinal outputs supporting balance and posture. Schematic of descending medial vestibular nucleus (MVN) pathways to the spinal cord (red arrows). MVN projections via the medial vestibulospinal tract (MVST) target cervical segments to drive the vestibulocollic reflex (VCR) for head and neck stabilization. Vestibulospinal reflex (VSR) pathways extend to lower spinal levels to regulate axial and limb muscle tone for postural control. MVN output also recruits pontomedullary reticular formation (PMRF) circuitry and reticulospinal pathways to coordinate broader postural responses.

4.1.2. Gaze stabilization by MVN

In addition to MVN's key role in balance, it also contributes critically to eye stabilization mechanisms. Eye movements are governed by three partially overlapping mechanisms, including the vestibulo-ocular reflex (VOR), the optokinetic reflex (OKR), and smooth pursuit eye movements (SEP). These pathways converge in VN and their cerebellar partners (9,25). VOR is a vestibular-driven brainstem circuit that stabilizes gaze during head movement. It uses inner-ear initiated vestibular inputs and carries information about the angular and linear head accelerations transmitted via the eighth cranial nerve (CN VIII) to VN, particularly MVN (28). From there, signals project to the abducens (cranial nerve VI) and oculomotor nuclei (cranial nerve III) and drive extraocular muscles in the opposite direction of head motion to maintain stable vision (40). VOR is especially important in the dark when visual feedback is not available, and the vestibular inputs are the only reference points. OKR instead provides complementary gaze stabilization based solely on visual input. It is triggered when the entire visual field drifts across the retina, as when tracking the landscape from a moving train. This motion, called retinal slip, is encoded by wide-field retinal ganglion cells and relayed to the accessory optic system (AOS) and pretectal nuclei (86,87). These visual motion signals are then relayed to both VN and the vestibulocerebellum, where they are integrated and converted into premotor eye commands (88,89). As the third gaze function mediated by MVN, SEP is a voluntary, attention-dependent tracking response used to follow small foveal targets, such as the tip of a moving pen. The pursuit pathway originates in extrastriate visual cortex, relays through the pontine nuclei, and converges on MVN to help generate the appropriate eye-movement commands (90).

The VOR and OKR circuits are closely interconnected. In mice, roughly one-third of VN neurons, mainly those that carry VOR-related eye movement signals, are modulated by full-field optokinetic stimulation. In macaques, neurons in the rostral VN and rostral fastigial nucleus that participate in VOR pathways also respond to optokinetic stimulation, but this visual modulation disappears when optic flow no

longer drives eye movements, indicating that these cells encode a combined vestibular-oculomotor signal rather than pure visual motion (91). This overlapping tuning helps to explain perceptual confusions between visual motion and self-motion, known as vection (such as the sensation of moving while watching ocean waves). When both sensory streams (visual and vestibular) are activated, MVN combines them to produce a visually enhanced vestibulo-ocular reflex (VVOR) for optimal gaze stabilization. Similar patterns of optokinetic modulation have been reported in other species, in which neurons in VN that carry vestibular signals for eye movements are also driven or modulated by full-field visual motion, indicating mixed visual-vestibular encoding within gaze-stabilizing circuits in goldfish and rabbits (92,93).

Taken together, VN functions as a complex premotor hub where vestibular, optokinetic, and pursuit signals are integrated, weighted, or vetoed under cerebellar supervision before being relayed to abducens and oculomotor motoneurons. The result is a flexible, frequency-dependent control system that minimizes retinal slip across diverse combinations of head, scene, and target motion.

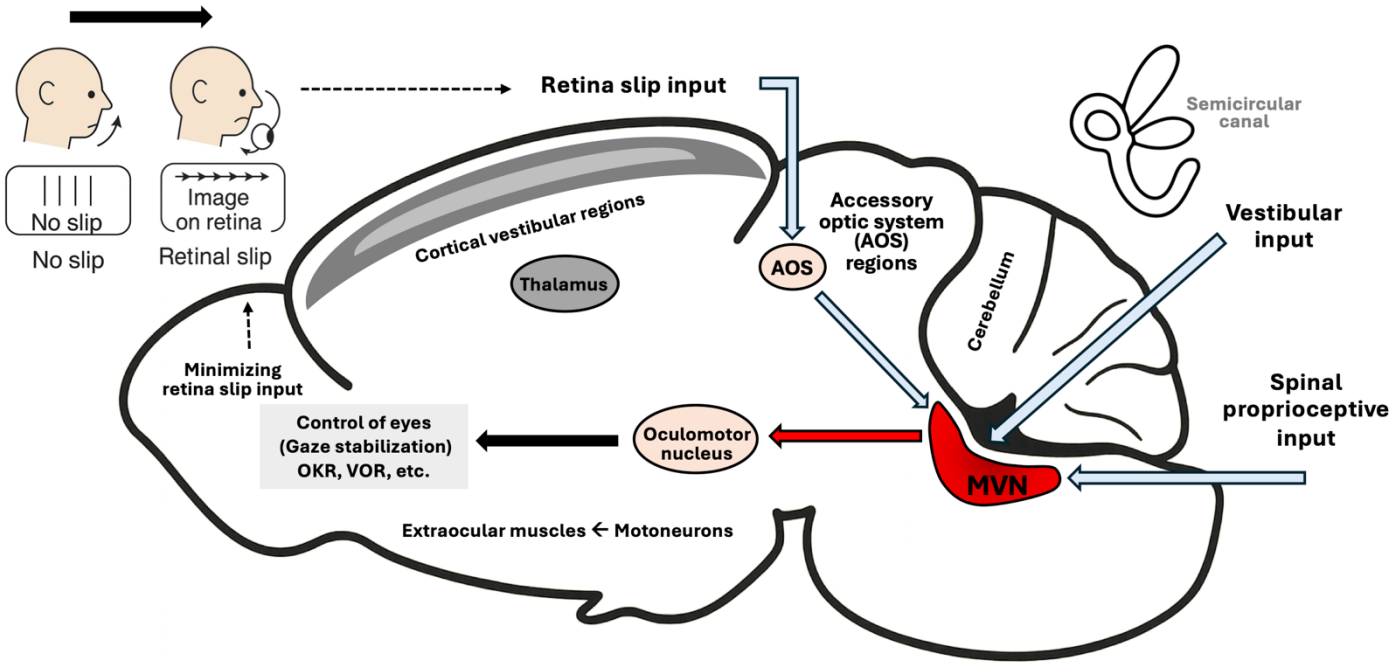

Figure II. MVN-centered gaze-stabilization circuitry driven by retinal slip and vestibular inputs. Schematic of gaze-stabilization pathways converging on the medial vestibular nucleus (MVN). Retinal slip signals, relayed via the accessory optic system (AOS), together with vestibular inputs from semicircular canals and proprioceptive feedback, are integrated in MVN. MVN outputs (red arrows) project to oculomotor nuclei to drive extraocular motoneurons, supporting optokinetic and vestibulo-ocular reflexes (OKR, VOR) that minimize retinal slip and stabilize gaze during head and body motion.

4.1.3. Other functions mediated by MVN

Beyond MVN's roles in posture and gaze maintenance, it participates in sleep regulation. Patients with vestibular disorders frequently report poor sleep quality and insomnia symptoms (94,95). Within MVN, distinct subsets of GABAergic neurons make different contributions to sleep control. Neurotensin-expressing GABAergic neurons in MVN promote NREM sleep and suppress REM sleep, whereas a separate population of laterally located GABAergic neurons helps to stabilize wakefulness and control transitions into REM sleep (96). MVN is further embedded in a broader sleep-arousal network. It receives monosynaptic inputs from canonical arousal and sleep nodes, including the locus coeruleus (LC), dorsal raphe (DRN), ventrolateral periaqueductal gray (VLPAG), and deep mesencephalic nucleus (DpMe) (97).

Additionally, MVN sends efferent projections to autonomic centers, including direct inputs to the caudal ventrolateral medulla (CVLM), providing a route for vestibular control of sympathetic outflow. Within this pathway, MVN GABAergic neurons participate in the vestibulosympathetic reflex, helping to stabilize arterial pressure during gravity-dependent postural changes such as standing or reorientation (98,99).

4.2. Functional neuronal classification of MVN

The heterogeneous cellular organization of MVN further complements its function as a multiplex hub, capable of mediating diverse functions. Classic primate single-unit recordings classified VN neurons into four response-defined classes based on visual and vestibular modulation: (**a**) position-vestibular-pause (PVP), (**b**) eye-head (EH), (**c**) vestibular-only (VO), and (**d**) flocculus-target neurons (FTN).

PVP neurons project to contralateral oculomotor nuclei and are the main premotor cells for the horizontal VOR. They encode head velocity during passive whole-body rotation and also carry oculomotor signals related to eye position or eye velocity when the head is still. This oculomotor component is a copy of

the motor command to move or hold the eyes, in contrast to a sensory response to visual motion. PVP neurons show little or no modulation by optic flow or retinal image slip, so they lack true visual-motion encoding. As a result, they do not contribute to smooth pursuit or OKR and are specialized instead for generating compensatory eye movements during head movements (VOR) (25,100).

EH neurons differ in that they encode both head velocity and oculomotor signals related to eye position and eye velocity. They fire strongly during smooth pursuit and provide major excitatory drive to abducens motoneurons during voluntary gaze shifts and visual tracking. Since they receive vestibular and visual-oculomotor inputs, EH neurons act as the primary premotor input to extraocular motoneurons during SEP, while making much smaller contributions to the VOR and to VCR that stabilize the head through neck muscles (101,102).

VO neurons are modulated by passive head rotations but not by eye movements. They selectively encode externally applied head motion, such as when the head is moved by an outside force, like a brief tilt of the surface underneath the animal or movement over shaky ground, rather than self-generated head motion. These neurons directly innervate spinal targets and contribute to head stabilization in space via VCR (101).

FTN neurons constitute a cerebellum-brainstem interface, as they receive direct GABAergic Purkinje-cell inhibition from the cerebellar flocculus, as well as primary vestibular and commissural inputs. During VOR adaptation, FTNs alter their vestibular sensitivity. Reversible flocculus inactivation reveals monosynaptic inhibition of FTNs and dissociates floccular versus non-floccular components of their tuning (103). This recalibration is engaged whenever actual head and body motion diverge from predicted visual feedback, for example when a person stands on an escalator that suddenly starts moving while they keep their head turned toward a fixed target. In this context, the VOR must adjust its gain to maintain stable gaze despite the unexpected body translation.

Although rodent vision differs from primate vision, the mice VN show a related organizational logic with two main classes identified in alert animal recordings: vestibular-only (VO) and eye-movement-sensitive (ES) neurons. In rodents, two-thirds of neurons behave as VO cells, responding robustly to passive vestibular (and often proprioceptive) stimulation with little or no modulation by eye position. These resemble primate VO neurons and are thought to support postural reflexes through VCR and VSR (12). The remaining ES neurons encode combined head-velocity and eye-position signals, and roughly one-fifth display response properties similar to primate PVP neurons that participate in the direct VOR pathway. An EH-like class, however, cannot be identified in mice because the behaviors required to define EH neurons in primates (smooth pursuit and VOR cancellation) do not exist in a similar form in rodents (104).

In a simplified model, work in primates suggests that PVP and EH neurons in the vestibular nuclei provide premotor drive to extraocular motoneurons via the abducens nucleus, whereas many VO neurons lack eye-movement sensitivity and instead contribute to vestibulospinal and other non-ocular pathways. Rodent data reveal the same broad division, with ES neurons contributing to ocular premotor circuits and VO neurons driving vestibulospinal pathways (30). Thus, the visual gaze-stabilization circuits mediated by MVN diverge somewhat across species and are more elaborate in primates. By contrast, the VO pathways that mediate balance correction through VCR and VSR are broadly conserved. As a result, these species differences are less consequential for interpreting MVN's role in postural control.

4.3. Neurochemistry of MVN

MVN is not only organized into response-defined physiological classes but is also built from a rich diversity of neurochemical cell types. Within the same anatomical nucleus, distinct populations of glutamatergic, GABAergic/glycinergic, and cholinergic neurons coexist, and these neuronal classes receive convergent modulatory inputs from serotonergic, noradrenergic, and cholinergic systems (71,98,105). This molecular

specialization allows overlapping subsets of MVN neurons to be recruited by different combinations of fast synaptic input and slower neuromodulatory signals, so that balance, gaze, autonomic tone, and arousal can be multiplexed through partially shared microcircuits. Cell-type specific viral tracing from VGLUT-Cre and VGAT-Cre mice demonstrated that glutamatergic and GABAergic neurons are distributed across VN, including medial and lateral divisions, where they form dense local inhibitory circuits and long-range excitatory efferent (99,106). Choline acetyltransferase (ChAT) immunohistochemistry combined with retrograde HRP tracing from the cerebellar uvula-nodulus identified a small cluster of ChAT-positive neurons in the caudal third of MVN that give rise to a cholinergic mossy-fiber projection to the vestibulocerebellum (107). Together, this organization establishes MVN as a multi-functional integrator, capable of synchronizing bilateral vestibular activity and coordinating the fine balance between postural control and ocular stabilization.

From a transmitter-defined perspective, MVN efferents are organized around broad glutamatergic and inhibitory projection pathways. Vestibulospinal neurons in MVN, many of which express VGLUT, provide excitatory drive to spinal circuits mediating VCR and VSR (105). Excitatory glutamatergic neurons also project to ocular premotor nuclei mediating OKR and VOR. In parallel, within MVN, GABAergic and glycinergic neurons form a dense local inhibitory network that controls the firing of these projection neurons through feed-forward and feedback inhibition (71,108). This intra-nuclear inhibition adjusts the gain and timing of vestibular signals and stabilizes the encoding of head motion for posture and gaze control (109). After unilateral vestibular lesions, changes in inhibitory synaptic efficacy and in $GABA_A$ and $GABA_B$-receptor function within the vestibular nuclei are key components of vestibular compensation (52,109–111). On the autonomic side, GABAergic vestibulo-sympathetic reflex (VSR) pathway neurons in the caudal medial and spinal vestibular nuclei, including caudal MVN, project predominantly to the caudal ventrolateral medulla (CVLM). These neurons form part of the vestibulo-sympathetic reflex that helps stabilize blood pressure during postural change (98). Furthermore, anterograde tracer studies combined with choline acetyltransferase

(ChAT) and glutamate immunolabeling show that MVN projects to the cerebellum via cholinergic and glutamatergic fibers, providing secondary vestibular input used by the vestibulocerebellum to adjust postural and cardiovascular reflexes (37,107,112). Functionally, these pathways allow MVN to simultaneously command spinal motoneurons, eye-movement control systems, cerebellar gain networks, and autonomic tone, each via neurotransmitter-matched channels.

From a transmitter-defined input perspective, MVN neurons receive convergent inhibitory and excitatory afferents. GABAergic neurons in MVN mediate vestibular compensation through commissural projections to the contralateral MVN. These neurons shape the spinal outputs through commissural inhibition and pathway-specific gating, selectively enabling or suppressing reflex circuits according to behavioral context. These inhibitory mechanisms, together with gain modulation of excitatory vestibulospinal neurons, stabilize posture and support compensation after vestibular loss (113–115). GlyT2-GFP reporter mice reveal glycinergic fastigial projections to ipsilateral vestibular and reticular targets and glutamatergic fastigial projections to contralateral VN (116). Purkinje cells in the cerebellar flocculus provide GABAergic inhibition onto FTNs in MVN, adjusting the gain and tuning of vestibular afferent signals.

Beyond fast glutamatergic and GABA/glycinergic transmission, MVN neurons are embedded in a dense neuromodulatory network that tunes their excitability and reflex gain according to behavioral state. Serotonergic (5-HT) inputs from the dorsal raphe nucleus and raphe obscurus densely innervate MVN (117). Consistent with this anatomy, chemogenetic activation of MVN-projecting 5-HT neurons or local 5-HT/5-HT_1A receptor manipulation in MVN impairs negative geotaxis, balance beam, and rotarod performance in rats (118). Acute 5-HT application into MVN produces similar deficits in these vestibular-dependent tasks, linking serotonin to MVN-mediated postural control. Histaminergic projections from the tuberomammillary nucleus directly depolarize MVN neurons, linking arousal to balance and gaze reflex enhancement (119). Noradrenergic projections from the locus coeruleus modulate vestibulospinal reflex amplitude to match

environmental demands (120). Cholinergic neurons in the pedunculopontine and laterodorsal tegmental nuclei also project to MVN, as shown by retrograde tracing with ChAT and AChE immunolabeling. These acetylcholine inputs, acting via nicotinic and muscarinic receptors, modulate spontaneous firing and gate glutamatergic afferent input and spike timing in MVN neurons (121,122). In summary, MVN functions as a multiplexed control hub. Excitatory neurons drive the core balance and gaze reflexes, while local excitation and inhibition set the operating range, and commissural inhibition preserves bilateral symmetry and supports vestibular compensation. Cerebellar circuits encode task-specific gains via glutamatergic and GABAergic inputs, and neuromodulatory systems tune MVN excitability to behavioral state.

5. Clinical relevance

After spinal cord injury, basic antigravity extensor tone and partial weight support can persist via spinal circuits, but automatic vestibulospinal balance reactions below the lesion are markedly impaired, indicating that stable posture depends on intact supraspinal (especially vestibular-reticulospinal pathways) rather than spinal circuitry alone (123–125). Disorders that affect this network can be peripheral, such as benign paroxysmal positional vertigo (BPPV), where displaced inner-ear crystals trigger brief spinning with certain head positions, or vestibular neuritis, where acute inflammation of the vestibular nerve causes vertigo and imbalance. Central lesions, including brainstem and cerebellar strokes as well as demyelinating disease, arise from more complex etiologies and produce more diverse patterns of deficit. Such lesions often cause distinctive symptoms, including blurred vision during head motion (oscillopsia), vertigo from asymmetric vestibular signals, and a wide-based, unsteady gait resulting from weakened vestibulospinal control (126). Clinically, vestibular implants have improved gait, posture, and quality of life within 6-12 months despite hearing trade-offs (127). Vestibular rehabilitation therapy (VRT) remains the first line of care, consistently reducing dizziness and improving gaze and stance, though outcomes vary and may not lead to full recovery

(128). Considering that regeneration of vestibular end organs is limited, recovery depends largely on central compensation. The heterogeneity of vestibular deficits demands a network-based triage. A better understanding of the vestibular network will allow clinicians to map which nuclei or tracts are damaged. Assessing the efficiency of axial (neck and trunk) and appendicular (limb) pathways, and pinpointing failure points such as left-right commissural inhibitory imbalance or cerebellar gain errors, will be a crucial first step in addressing the disorder. This approach may enable pathway-specific treatment with higher efficacy and fewer off-target effects. For example, recent rodent work shows that PV-positive GABAergic neurons in MVN mediate commissural inhibition and shape vestibular rebalancing after unilateral loss (70). Therapeutically targeting such central neuron classes may provide actionable mechanisms for targeted neuromodulation or pharmacotherapy during the symptomatic window.

6. The facial motor nucleus (FMN)

6.1. Functions mediated by FMN

The facial motor nucleus (FMN/FN) lies in the caudal pons, just caudal to the trigeminal motor nucleus. It contains the lower motoneurons of the facial nerve (cranial nerve VII) that innervate facial muscles, neck muscles in primates, and the whisker pad in rodents (1). Facial muscles support many complex behaviors. About thirty bilateral muscle pairs span the skull and neck. Their nuanced activation by branches of cranial nerve VII enables respiration and feeding in fish, rhythmic whisking of sensory vibrissae in rodents, and expressive and speech-related movements in humans. Damage to this nerve causes facial paralysis and synkinesis (involuntary movements such as eye twitching when smiling), which is socially disabling and remains a clinical challenge. In mammals, FMN is subdivided into medial (M), intermediate (I), dorsolateral (DL), and lateral (L) subnuclei, and each motor pool innervates a single facial muscle. In mice specifically, non-overlapping motor pools in FMN form discrete groups whose axons project to individual facial muscles

and show minimal cross-innervation (129). This organization mirrors the motor-pool arrangement described in the primate facial nucleus and follows the same general principle seen in spinal motor pools, where neurons are grouped in columnar clusters that each control a specific muscle or muscle set (130).

FMN activity directly generates whisker movements, with the lateral FMN containing whisker-specific cholinergic motoneurons (vibrissa motoneurons/vMNs). vMNs innervate extrinsic muscles (to drive backward movements of multiple whiskers) and intrinsic muscles (to drive forward movements of single whiskers) (1). This supports a sophisticated system in which rodents use whiskers for active touch in wall tracking, object or landmark localization, and texture discrimination (131). Behavioral studies show that mice rely more on whisker input rather than vision to shape forelimb trajectories during high-speed obstacle stepping. They select distinct kinematic strategies from rapid, whisker-derived estimates of obstacle location, and performance degrades when whisker cues are absent (132). Daily whisker trimming from the third postnatal day impairs early sensorimotor coordination, including cliff avoidance and huddling (133). Studies further show that whisker control matures in parallel with locomotion. Whisking emerges alongside coordinated body movements to guide limb placement and maintain stability during exploration (134). During plus-maze navigation, mice coordinate eye movements with whisker positioning, and whisker asymmetry predicts turn direction earlier than eye movements, demonstrating a coupled sensorimotor strategy that stabilizes gaze and body trajectory during motion (135). In short, FMN integrates diverse premotor drives to generates facial expression and to orchestrate whisker protraction and retraction for active touch, assisting complex behaviors aimed at object detection, navigation, and exploration, as well as fundamental functions in feeding, breathing, and airway control. This organization makes FMN a hub that links sensorimotor context to precise, behavior-relevant actions.

6.2. Neuronal population identity of FMN

FMN is composed predominantly of cholinergic motoneurons that express choline acetyltransferase (ChAT) and the vesicular acetylcholine transporter (VAChT), which serve as reliable markers of cranial motoneurons (136). Within the adult brainstem, mapping studies reported that motor nuclei (including FMN) lack GAD67-expressing cell bodies, indicating a low presence of GABAergic interneuron populations. Inhibitory drive to facial motoneurons arises from premotor GABAergic and glycinergic neurons located in adjacent reticular regions that project into the nucleus (137–139). Facial motoneurons express functional $GABA_A$/$GABA_B$-receptors and ionotropic glutamate receptors, and these receptor profiles remodel after facial nerve injury, demonstrating both inhibitory and excitatory control at the motoneuron level.

6.3. Network of FMN

FMN provides the principal motor outflow to facial and orofacial muscles, coordinating their activity according to ongoing sensory input and internal state. FMN sends its main efferent peripherally via cranial nerve VII to muscles. Centrally, FMN intranuclear interneurons, whose axons do not exit the brainstem, provide inputs to key brainstem networks. In rats, anterograde tracing after selective facial motoneuron degeneration showed that interneurons within FMN send bilateral projections to the nucleus tractus solitarius, nucleus ambiguus, and ventrolateral reticular formation. They also project ipsilaterally to the parabrachial and Kölliker-Fuse respiratory complexes (140). These pathways engage with respiratory and premotor autonomic networks to coordinate airway and cardiorespiratory adjustments. The neurotransmitter phenotype of these interneurons remains undefined. This places FMN within brainstem circuits that couple orofacial motor activity to breathing and airway control and supports a model in which FMN interneurons, rather than the motoneurons themselves, provide the principal intracerebral output of FMN.

Regarding the input organization, FMN afferents vary markedly across species. In rodents, retrograde tracing identifies only sparse cortical neurons in the lateral agranular and orofacial motor cortices that project directly to FMN (141). Anterograde studies confirm that most cortical influence reaches FMN indirectly through dense projections to reticular and trigeminal premotor nuclei, principally the intermediate reticular formation (IRt) and the spinal trigeminal oral (SpVO) and interpolar (SpVIr) nuclei (142). The indirect cortical projections to FMN provide higher-order modulation of this nucleus. In contrast, non-human primates possess extensive monosynaptic corticofacial pathways from ventrolateral primary motor cortex (M1) and premotor cortices. This enables fine voluntary facial control and recovery after cortical injury through reorganization of surviving corticofacial projections (143–146). While direct cortical pathways to FMN moderately diverge across species, the brainstem inputs to FMN remain conserved (144). Within the brainstem, FMN receives its strongest inputs from PMRF that coordinate cranial motor and respiratory patterns and give rise to reticulospinal pathways controlling neck, head, and postural adjustments during balance-demanding movements (15,65,147–149). Further, classical tract-tracing in rats showed that FMN receives brainstem inputs from trigeminal sensory nuclei and VN. Through its convergent ascending and descending links, FMN is embedded in a reticulo-vestibular framework that enables this nucleus to integrate sensory, autonomic, and motor streams for a diverse number of functions.

7. Rationale

This thesis identifies a previously overlooked population of VIP-expressing neurons in the facial motor nucleus (FMN^{VIP}) and tests whether these neurons modulate medial vestibular nucleus (MVN) circuits to regulate balance. We use modern circuit dissection tools, chemogenetics, DeepLabCut-based behavioral analysis, and *in vivo* Ca^{2+} and neuromodulator sensor photometry to examine the behavioral role of FMN^{VIP} neurons. First, we map the FMN^{VIP} to MVN pathway using anatomical tracing to confirm its connectivity. We

then define the neurotransmitter identity of FMN^{VIP} neurons and their downstream MVN targets. To understand the function of this population, we record neural activity of FMN^{VIP} neurons and neuromodulator release dynamics in MVN during balance tasks and correlate them with the timing and magnitude of postural responses. Finally, we test causality by ablating or acutely silencing FMN^{VIP} and MVN neurons to probe their contributions to balance control. Together, these experiments are designed to determine whether FMN^{VIP} neurons modulate MVN output during balance control and to provide new insight into the circuit basis of posture stabilization.

8. Central hypothesis

By screening VIP-Cre::Ai14 transgenic mice, we identified a population of VIP-expressing neurons in FMN (FMN^{VIP} neurons) whose axons extend over milimetre distances toward MVN. FMN is classically defined as a motor nucleus that mainly drives orofacial actions (150). Based on this anatomical observation, we hypothesize that FMN^{VIP} neurons form a long-range modulatory pathway that targets specific MVN microcircuits and plays a critical role in regulating vestibular-related behaviors, such as gaze stabilization and balance control.

CHAPTER 2: RESULTS

1. Identifying a population of neurons in FMN

We identified a group of vasoactive intestinal peptide (VIP)-expressing neurons in the facial motor nucleus (FMN; FMN^{VIP}) of the brainstem while we screened across different cortical interneuron subtype reporter mouse lines: parvalbumin (PV-) Cre::Ai14, somatostatin (SST-) Cre::Ai14, and VIP-Cre::Ai14 in the brainstem (FMN^{VIP} neurons, Fig. 1A). There was also clear labeling of VIP-expressing neurons in nearby regions such as the bed nucleus of the stria terminalis and hypothalamus, consistent with what has been reported in the literature (151–153). In contrast, PV-Cre::Ai14 and SST-Cre::Ai14 animals did not show any labeled neurons in FMN (VIP: 43.90 ± 8.35; SST: 0.00 ± 0.00; PV: 2.15 ± 0.32; VIP vs SST: $p = 0.0006$; VIP vs PV: $p = 0.0006$; Fig. S1A-C). Interestingly, we also observed an axonal tract extending from the caudal pons at FMN into the rostral medulla at the pontomedullary junction and terminated near the floor of the fourth ventricle within the ventral medial vestibular nucleus (MVN, Fig. 1A). To test whether these MVN-projecting fibers arose specifically from FMN^{VIP} neurons rather than other VIP populations in the VIP-Cre::Ai14 animals, we injected a Cre-dependent GFP-expressing AAV (AAV-DIO-GFP) into the right FMN of VIP-Cre::Ai14 animals (Fig. 1B). Histological analysis revealed a dense GFP-positive axonal tuft in the ipsilateral MVN that was closely matched to the tdTomato-labeled axons in the reporter line. The GFP-expressing cell bodies also co-localized with the tdTomato-positive neurons in FMN, confirming selective targeting of FMN^{VIP} neurons and that the MVN-projecting axons arose from FMN^{VIP} neurons. We then quantified the distribution of FMN^{VIP} neurons along the anterior-posterior (AP) axis by counting tdTomato-labeled cell bodies in serial coronal sections at defined distances from bregma. VIP-expressing neurons were distributed throughout FMN, with an anterior peak at -5.55 mm from bregma (46.43 ± 7.74; Fig. 1C). Although VIP

expression in FMN has been reported in proteomic and atlas studies (154,155), the identity of these VIP-expressing cells as a distinct FMN subpopulation and their function, circuit role, and transmitter phenotype remain uncharacterized. Moreover, the dense projecting axons of these neurons to the sensorimotor vestibular region, MVN, also raise the question whether these FMN^{VIP} neurons play a distinct brainstem role in the vestibular system.

2. FMN^{VIP} neurons are not required for OKR in intact gaze stabilization

Having identified a FMN^{VIP} neuronal population that sends projections to MVN, we next asked whether these neurons contribute to MVN-dependent functions. MVN is located at the core of major brainstem pathways that are involved in stabilizing gaze and postural maintenance (1,30,156). We first examined the contribution of FMN^{VIP} neurons to the optokinetic reflex (OKR), a major MVN-mediated gaze stabilization mechanism. To do this, our collaborators (Dr. Baohua Liu's lab, University of Toronto Mississauga) employed a Cre-dependent taCasp3-TEVp ablation strategy and examined the animals with a standard OKR assay. In this approach, an engineered pro-caspase-3 (taCasp3) is co-expressed with TEV protease, and upon TEVp cleavage, it activates taCasp3 and triggers cell-autonomous apoptosis. VIP-Cre::Ai14 animals received bilateral FMN injections of AAV-DIO-taCasp3-TEVp to ablate FMN^{VIP} neurons (FMN-taCasp), and the sham control received the AAV-DIO-GFP injections (Fig. 1G). Post hoc analysis confirmed ~68% loss of FMN^{VIP} neurons (68.26% ± 5.33%; $p < 0.0002$, Fig. S1D-F). OKR was measured using full-field "virtual drum" gratings (SF = 0.16 cpd, TF = 0.1-6.4 Hz), while eye movements were tracked with infrared video-oculography in head-fixed animals (Fig. 1G), and OKR gain was defined as eye velocity divided by grating velocity. Surprisingly, taCasp animals did not show changes in OKR gain compared to sham animals at any tested frequency (Sham: 0.43 ± 0.03; FMN-taCasp: 0.38 ± 0.03; $p = 0.21$; Fig. 1H). Next, the Liu Lab tested whether

ablating neurons in MVN would affect OKR. Wild-type (WT) C57BL/6J animals received bilateral intracranial injections of AAV-DIO-taCasp3-TEVp (MVN-taCasp) or AAV-DIO-GFP (sham) together with AAV-Cre in MVN (Fig. 1E). Consistent with earlier studies that MVN neurons play a key role in OKR (33), the OKR gain was significantly reduced in MVN-taCasp animals compared with sham animals at low stimulus frequencies, but not at higher frequencies (Sham: 0.51 ± 0.03; MVN-taCasp: 0.36 ± 0.05; $p = 0.03$; Fig. 1F). Considering that the rodent optokinetic system is most effective at low temporal frequencies, and OKR gain drops as frequency increases (157,158), these findings strongly support the critical premotor role of MVN in visually driven OKR (159,160). Thus, although MVN is essential for OKR modulation, FMN^{VIP} neurons do not appear to contribute to the MVN-dependent pathway for gaze stabilization.

3. FMN^{VIP} ablation disrupts sensorimotor but not general motor performance

Considering that MVN is also involved in sensory input integration and transforms it into postural motor commands, we next asked whether FMN^{VIP} neurons contribute to sensorimotor coordination and balance. We tested both MVN and FMN^{VIP} ablated animals in the vertical pole test (VPT), a well-established and sensitive measure of sensorimotor coordination and vestibular performance (Fig. 1I) (161,162). In the dark environment, animals were placed atop a vertical pole (20 mm diameter, 95 cm height) and allowed to freely descend. Behavior was video recorded and assessed for animals' descending kinematics. We noticed that sham animals always descended smoothly toward the home box along a straight vertical path. In contrast, MVN-taCasp animals showed a pronounced phenotype, in which they consistently rotated around the pole in a spiral motion while descending the pole. To specifically quantify the torsional instability, we counted spiral turns, defined as rotations (half turn, ≥180°; full turn, ≥360°). We then computed a spiral motion intensity index (SMI) as the number of spiral rotations per trial normalized to the mean rotation count in sham animals. MVN-

taCasp animals showed a significantly higher SMI than sham animals ($p = 0.0071$; Fig. 1J). These observations align with evidence that vestibulospinal neurons in MVN transform sensed instability into commands that preserve balance and antigravity support (56,163). We next tested FMN-taCasp animals and their sham controls in VPT. FMN-taCasp animals also exhibited a clear spiral-descending phenotype similar to that of MVN-taCasp animals. Quantitative analysis demonstrated a significant increase in SMI compared to sham animals ($p = 0.0003$; Fig 1K). The intriguing similar behavioral deficit seen with MVN and FMN^{VIP} ablations suggests that these populations could be behaviorally linked, and FMN^{VIP} neurons may act upstream of the MVN circuits.

To determine whether this phenotype is a result of general motor impairments rather than vestibular impairments, we evaluated motor performance of FMN-taCasp animals and their sham controls using three standard motor assays: accelerating rotarod, forelimb grip strength, and open field (Fig. S1G-I). On the accelerating rotarod, FMN-taCasp animals showed intact gait and motor coordination that were comparable to sham animals (Sham: 300.66 ± 36.00; FMN-taCasp: 260.87 ± 26.95; $p = 0.33$; Fig. S1G) (164). The forelimb grip strength test also showed similar muscle strength between the two groups (Sham: 117.94 ± 8.95; FMN-taCasp: 110.19 ± 6.53; $p > 0.99$; Fig. S1H) (165). Lastly, the overall locomotor activity in the open field measurements (motion velocity) was comparable across the groups, indicating unaltered baseline gait despite FMN^{VIP} ablation (Sham: 5.87 ± 0.49 cm/s; FMN-taCasp: 4.25 ± 0.41 cm/s; $p = 0.065$; Fig. S1I, (166)). Taken together, these assays demonstrate that FMN^{VIP} ablation does not impair gross motor functions, and FMN^{VIP} could be part of the MVN circuits that are involved in regulating vestibular-sensorimotor coordination.

4. FMN^{VIP} neurons contribute to vestibular balance

To specifically probe the involvement of FMN^{VIP} neurons in balance control and postural stability, we adapted a horizontal beam test (HBT) (41). This assay challenges animals to traverse a narrow beam, providing a vestibular-dependent measure of balance compared with walking on a stable surface. In this task, animals crossed a metal horizontal beam (5 mm wide, 40 cm long) from a fixed starting platform toward their home box. A camera mounted above the beam recorded each traversal epoch from a top-down view, and videos were subsequently processed with DeepLabCut® (DLC) to label and track body motion during balance traversal (Fig. 1L). To assess animals' general performance, we calculated the task's success rate as the proportion of trials in which animals completed the beam traversal. FMN-taCasp animals did not differ from sham animals in traversal success rates, indicating unaltered locomotion and navigation (Sham: 72.0% ± 17.43%; FMN-taCasp: 54.69% ± 10.74%; $p = 0.45$; Fig. 1O). We observed that FMN-taCasp animals exhibited a more unstable, wobbly traversal. Hence, we quantified the animal's postural instability by calculating postural-angle variance, which was defined as the variance of the angle formed by the start of the beam (SB), the animal's head (H), and the sacrum (S) during traversal (Fig. 1L). We found that FMN-taCasp animals showed markedly higher postural-angle variance while traversing the narrow beam compared to sham animals ($p = 0.004$; Fig. 1P). Since both MVN and FMN^{VIP} ablated animals showed similar sensorimotor coordination deficits on VPT, we next asked whether ablating neurons in MVN would also produce similar behavioral performance on HBT. MVN-taCasp animals showed comparable traversal success rates as sham animals (Sham: 76.21% ± 8.87%; MVN-taCasp: 69.28% ± 10.93%; $p = 0.78$; Fig. 1M). However, they also exhibited similarly unstable, wobbly traversal as FMN-taCasp animals with markedly higher postural-angle variance during beam traversal ($p = 0.04$; Fig. 1N). Since neuronal ablations can lead to long-term changes in the circuits and affect the behavioral outputs (167), we next validated the FMN^{VIP} neuronal function by acutely inhibiting their activity using a

chemogenetic approach with Designer Receptors Exclusively Activated by Designer Drugs (DREADDs). VIP-Cre animals received bilateral injections of AAV-DIO-hM4Di-mCherry into FMN to selectively express the inhibitory Gi-coupled receptor in FMN^{VIP} neurons (Fig. 1Q). After three weeks of expression, animals were tested on both VPT and HBT. Each animal completed two sessions (24 hours apart), in which one session involved saline administration and the other involved the DREADDs agonist JHU-37160 (JHU, 0.5 mg/kg^{-1}, IP). JHU-37160 is a high-potency, brain-penetrant DREADDs agonist with substantially reduced off-target receptor activity compared to commonly used the chemical Clozapine N-oxide (CNO) (168). In VPT, saline-treated animals descended the pole in a straight, axis-aligned trajectory, whereas JHU-treated animals showed elevated SMI with increased descending spiral motions during the descent ($p < 0.0001$; Fig. 1R-S). We next asked whether this manipulation also affected the balance traversal in HBT (Fig. 1T). Similar to the ablation results, JHU treatment did not affect HBT traversal success rate (Saline: 90.0% ± 6.83%; JHU: 96.66% ± 3.33%; $p = 0.72$; Fig. 1U), but the animals also showed unstable, wobbly traversals with increased postural-angle variance after FMN^{VIP} inhibition ($p = 0.019$; Fig. 1V). The chemogenetic inhibition experiments showed that acute inhibition of FMN^{VIP} neurons was sufficient to recapitulate VPT and HBT phenotypes seen in FMN^{VIP} ablation. Moreover, the traversal impairment on HBT complements the VPT sensorimotor deficits and further demonstrates that FMN^{VIP} neurons contribute to MVN-mediated vestibular circuits for balance control rather than oculomotor gaze stabilization.

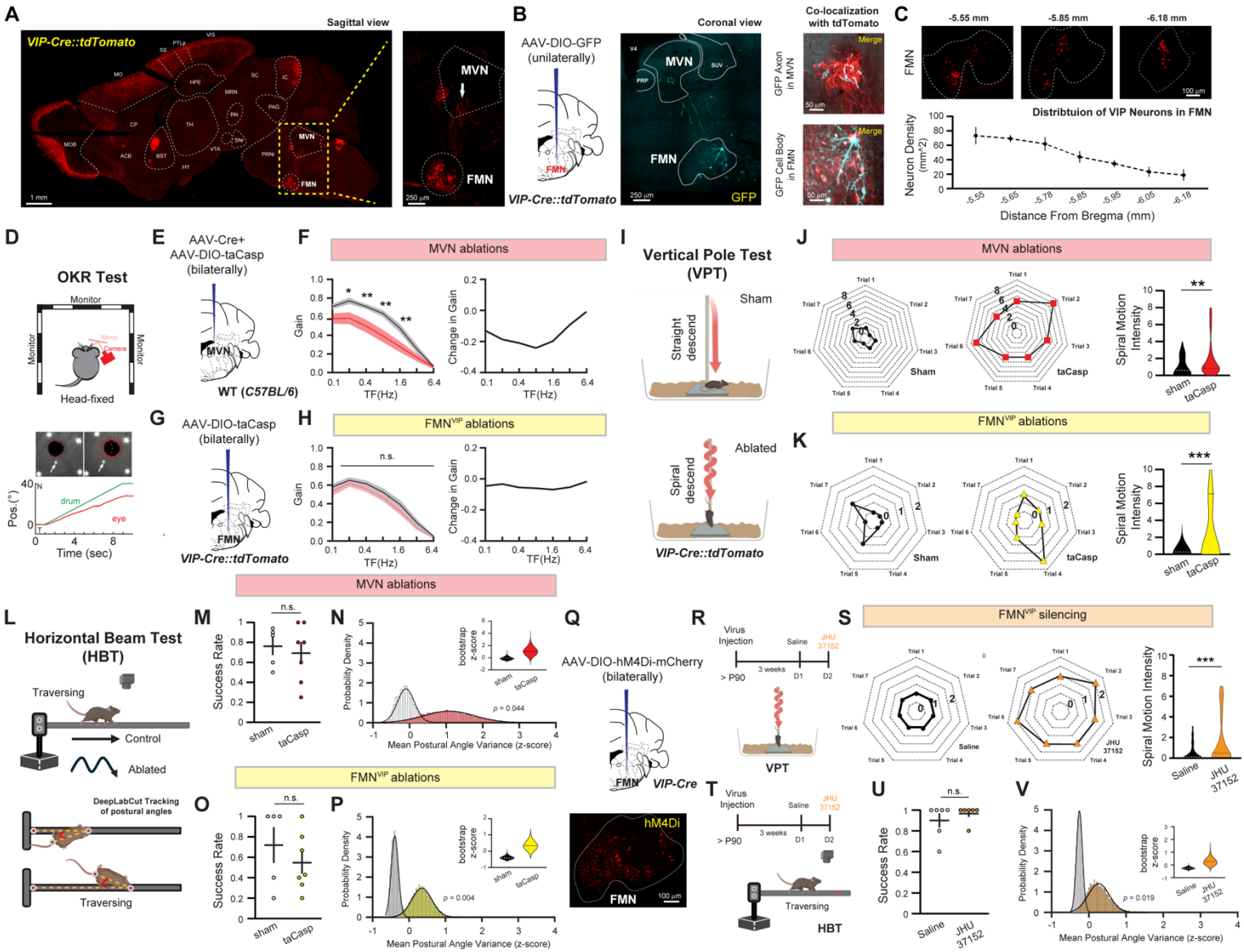

Figure 1. Ablation or chemogenetic inhibition of FMN^{VIP} neurons impairs postural maintenance without altering optokinetic reflex (OKR).

(A-C) Identification and anatomical mapping of FMN^{VIP} neurons: (A) Identifying FMN^{VIP} neurons and their axonal projections. Left: Sagittal brain section (~1.10 mm lateral from the midline) from VIP-Cre::Ai14 animal shows tdTomato-labeled VIP-expressing cells in the facial motor nucleus (FMN) and their long-range projections toward the medial vestibular nucleus (MVN). Right: A higher-magnification view of the yellow dashed region on the left. The arrow points to a tdTomato-labeled FMN^{VIP} axonal tuft within MVN. **(B)** Coronal view of AAV-DIO-GFP labeling in VIP-Cre::Ai14 animals. Left: schematic of unilateral FMN injection. Middle: A representative section at anteroposterior

(AP) -5.9 mm from bregma shows GFP-expressing FMN^{VIP} neurons and a dense GFP-expressing axonal tuft within MVN beneath the fourth ventricle. Right: higher-magnification images of GFP-expressing FMN^{VIP} axons co-localized with tdTomato-labeled axons in MVN (top), and tdTomato-labeled FMN^{VIP} cell bodies overlapped with GFP-expressing cell bodies (bottom). **(C)** Rostro-caudal (AP) distribution of FMN^{VIP} neurons. Top: representative coronal sections at -5.55, -5.85, and -6.18 mm from bregma show tdTomato-labeled VIP-expressing cells within FMN. Bottom: Quantification of VIP-labeled cell densities across multiple FMN levels (AP: -5.55 to -6.18 mm, n = 21 samples).

(D-H) Optokinetic reflex (OKR) after MVN and FMN^{VIP} ablations: (D) Top: Head-fixed animals viewed drifting sinusoidal gratings on three monitors while the eye position was recorded with infrared video-oculography via a mirror-camera system. Bottom: example pupil images show the tracked contour (red dashed circle), and representative traces illustrate drum motion (green) and eye motion (red). OKR gain is defined as eye velocity divided by stimulus velocity. **(E)** Wild-type (WT) C57BL/6J animals received bilateral injections of AAV-Cre + AAV-DIO-taCasp into MVN (MVN-taCasp), and animals injected with AAV-Cre + AAV-DIO-GFP served as sham controls. **(F)** Left: MVN-taCasp animals showed reduced OKR gain at low and mid temporal frequencies (TFs). Right: summarized plot of change-in-gain shows the difference between MVN-taCasp and sham across TFs (sham: N = 14 animals; MVN-taCasp: N = 12 animals; one-sided Wilcoxon rank-sum tests). **(G)** Left: VIP-Cre::Ai14 animals received bilateral AAV-DIO-taCasp injections into FMN (FMN-taCasp), and sham animals received AAV-DIO-GFP. **(H)** Left: FMN-taCasp animals did not show any changes in OKR gain at any tested TF compared to sham animals. Right: summarized plot of change-in-gain shows no difference between FMN-taCasp and sham animals across TFs (sham: N = 10 animals; FMN-taCasp: N = 10 animals; one-sided Wilcoxon rank-sum tests). Solid lines denote the mean, and shaded regions the SEM. **$P < 0.01$, *$P < 0.05$, n.s., not significant.

(I-K) Vertical pole test (VPT) after MVN and FMN^{VIP} ablations: (I) Schematic of the vertical pole test (VPT). Animals were placed on a rough-surfaced vertical pole and allowed to reorient and descend. **(J)** Representative spider plots of sham (left) and MVN-taCasp (middle) animals. Each point corresponds to a single trial, and the radial distance indicates the spiral motion intensity (SMI). Right: MVN-taCasp animals exhibited higher SMI than sham animals (sham: N = 10 animals; MVN-taCasp: N = 7 animals; two-tailed Mann-Whitney U test). **(K)** Representative spider plots of sham (left) and FMN-taCasp (middle) animals. Right: FMN-taCasp animals also showed elevated SMI compared to sham animals (sham: N = 6 animals; FMN-taCasp: N = 8 animals; two-tailed Mann-Whitney U test). Dashed horizontal lines indicate group means. ***$P < 0.001$, **$P < 0.01$.

(L-P) Horizontal beam test (HBT) after MVN and FMN^{VIP} ablations: **(L)** Schematic of the horizontal beam test (HBT). Animals traversed across a narrow-elevated beam, and camera captured body posture movements from the top **(M)** Traversal success rate after MVN ablation. Scatter plot shows the fraction of successful traversals, and no significant

difference between the two groups (sham: N = 5 animals; MVN-taCasp: N = 7 animals; two-tailed Mann-Whitney U test). **(N)** Probability density plots of mean bootstrap (10,000x) z-scored postural-angle variance. Inset violin plots show the distributions of the bootstrapped means. MVN-taCasp animals exhibited significantly elevated postural-angle variance and wobbly-like traversal (sham: N = 5 animals, MVN-taCasp: N = 7 animals; one-sided empirical test). **(O)** Traversal success rate after FMN^{VIP} ablation. Scatter plot shows the fraction of successful traversals, and no significant difference between the two groups (sham: N = 5 animals; FMN-taCasp: N = 7 animals; two-tailed Mann-Whitney U test). **(P)** Probability density plots of mean bootstrap (10,000x) z-scored postural-angle variance. Inset violin plots show the distributions of the bootstrapped means. FMN-taCasp animals also exhibited significantly elevated postural-angle variance and wobbly-like traversal (sham: N = 5 animals, FMN-taCasp: N = 7 animals; one-sided empirical test). Dashed horizontal lines indicate group means. n.s., not significant.

(Q-V) Chemogenetic silencing of FMN^{VIP} neurons followed by the vertical and horizontal beam test performance: **(Q)** Top: bilateral injections of AAV-DIO-hM4Di-mCherry into the FMN in VIP-Cre animals. Bottom: A representative coronal section of FMN with hM4Di-mCherry expression (red). **(R)** Experimental timeline followed by VPT, and animals were tested on consecutive days with Saline (Day 1) and JHU (Day 2). **(S)** Representative spider plots of VPT performance on Saline (left) and JHU (middle) day. Each point corresponds to a single trial, and the radial distance indicates SMI. Right: JHU administration induced higher SMI than Saline (N = 8 animals; two-tailed Mann-Whitney U test). **(T)** Experimental timeline for chemogenetic inhibition followed by HBT, and animals were tested on consecutive days with Saline (Day 1) and JHU (Day 2). **(U)** Traversal success rate after FMN^{VIP} inhibition. Scatter plot shows the fraction of successful traversals, and no significant difference between the two conditions (N = 6 animals; two-tailed Mann-Whitney U test). **(V)** Probability density plots of mean bootstrap (10,000x) z-scored postural-angle variance. Inset violin plots show the distributions of the bootstrapped means. FMN^{VIP} inhibition induced significantly elevated postural-angle variance and a wobbly traversal (N = 6 animals; one-sided empirical test). Dashed horizontal lines indicate group means. ***$P < 0.001$, n.s., not significant.

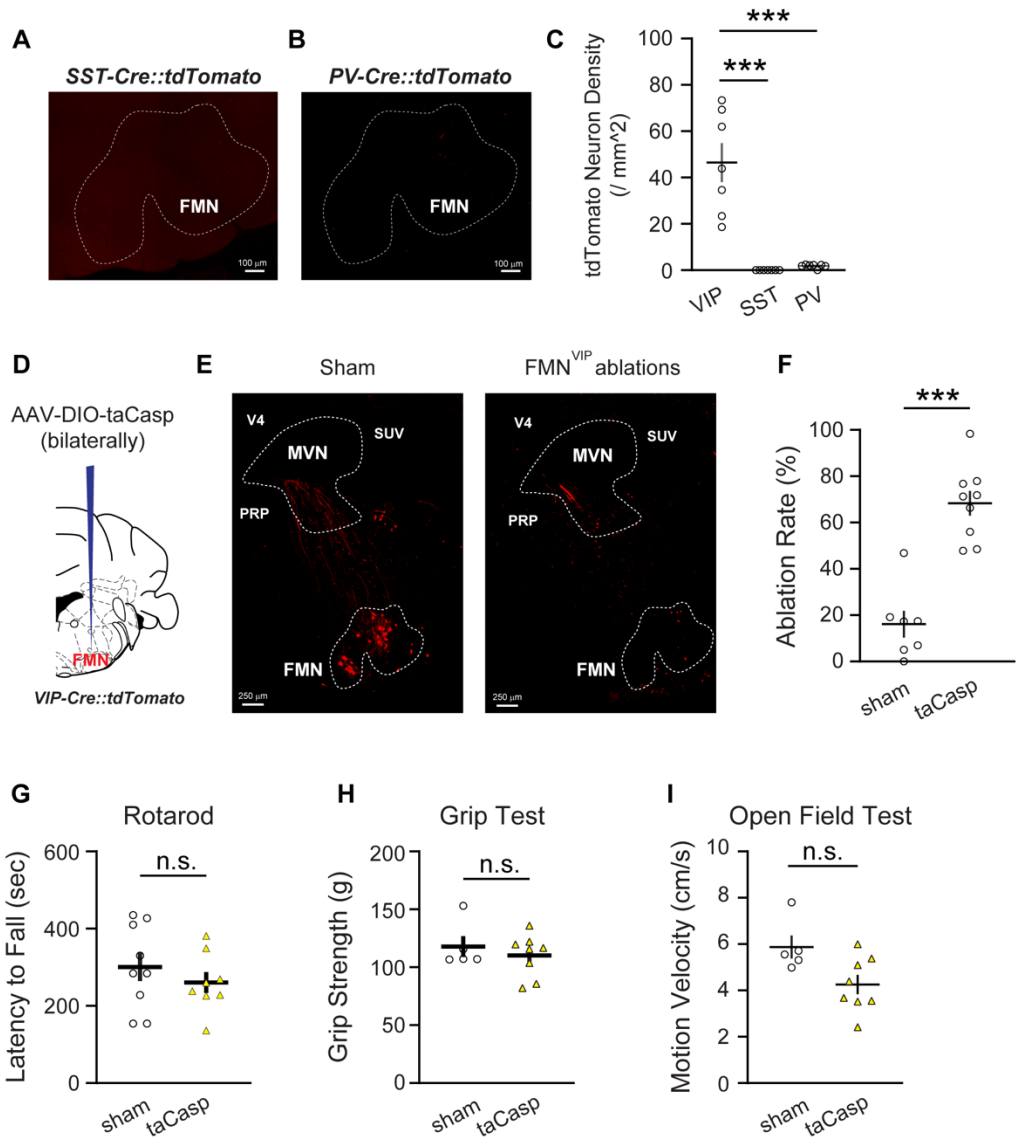

Supplementary Figure 1.

(A-C) Screening reporter mouse lines show sparse SST/PV labeling in FMN: FMN does not contain SST- or PV-expressing cells. **(A-B)** Representative coronal sections of FMN from SST-Cre::Ai14 and PV-Cre::Ai14 animals which only a few SST-expressing or PV-expressing cells were detected within FMN (dashed outline). **(C)** Scatter plot shows significantly higher tdTomato-labeled cells in FMN of VIP-Cre::Ai14 than both SST- and PV-Cre::Ai14 animals (n = 7 regions; two-tailed Mann-Whitney U test). ***P < 0.001.

(D-F) FMN-targeted taCasp ablation eliminates the majority of VIP-expressing cells in FMN: **(D)** Schematic of bilateral FMN injections in VIP-Cre::Ai14 animals; sham animals received AAV-DIO-GFP. **(E)** Representative coronal

sections show tdTomato-labeled VIP cells in sham animals (left), and taCasp ablation (right). **(F)** FMN-taCasp animals showed markedly higher ablation rates than sham animals (sham: N = 7 animals; FMN-taCasp: N = 9 animals; two-tailed Mann-Whitney U test). ***P < 0.001**.**

(G-I) Motor performance does not change after FMN^{VIP} ablation: (G) Latency to fall on the accelerating rotarod did not differ between sham and FMN-taCasp animals (sham: N = 9 animals; FMN-taCasp: N = 8 animals; two-tailed Mann-Whitney test). **(H)** Forelimb grip strength measured with a horizontal-bar force transducer did not differ between sham and FMN-taCasp animals (sham: N = 5 animals; FMN-taCasp: N = 8 animals; two-tailed Mann-Whitney U test). **(I)** Mean locomotor velocity during a 10-min open-field session did not differ significantly between sham and FMN-taCasp animals (sham: N = 5 animals; FMN-taCasp: N = 8 animals; two-tailed Mann-Whitney U test). n.s., not significant.

5. FMN^{VIP} neurons show linked activity dynamics to balance maintenance

Since the behavioral tests pointed to the involvement of FMN^{VIP} neurons in balance control, we next examined whether and how their activity changes during postural balance maintenance on HBT. We unilaterally delivered a Cre-dependent GCaMP-expressing viral construct (AAV-DIO-GCaMP8m) into FMN of VIP-Cre::Ai14 animals and implanted an optic fiber cannula above the targeted region. After three weeks, the animals were tested on HBT while we recorded population Ca^{2+} activity using *in vivo* fiber photometry. We calculated the area under the curve (AUC) from ΔF/F traces to quantify changes in neuronal activity (Fig. 2A-B) (169–171). We found that the AUC during the traversal epoch was significantly higher than the baseline epoch (ΔAUC = traversal - baseline), indicating increased FMN^{VIP} activity when animals were engaged in the balance-demanding beam traversal ($p = 0.0063$; Fig. 2C). Intriguingly, when we examined the postural-angle variance during traversal, we found substantial trial-to-trial variability even within WT animals (Fig. 2D). This observation prompted us to examine whether FMN^{VIP} activity can track the variability of the animal's balance. We, therefore, performed a trial-by-trial correlation analysis between FMN^{VIP} activity (ΔAUC) and postural-angle variance, which revealed a positive correlation between FMN^{VIP} activity and postural instability ($r = 0.37$, $p = 0.0004$, Fig. 2E). This finding further demonstrates that the FMN^{VIP} neurons are not only recruited during balance demands, but the magnitude of FMN^{VIP} activation also depends on the current stability state of the animal during traversal.

We next asked how FMN^{VIP} neurons respond to a sudden and acute balance perturbation, and whether the changes in activity are similar to the narrow beam traversal. To test this, we modified HBT so that when the animals traversed past a fixed point (final three quarters) of the beam, they received an unpredictable balance perturbation (0.8 cm at 95 cm/s; 10 randomly interleaved left or right perturbations; Fig. 2F). We first

quantified the changes in population activity by measuring the peak ΔF/F values immediately before (baseline) and after the perturbation (post-perturbation) and calculated the relative fold change in peak values (Fig. 2G). The balance perturbation evoked an immediate, time-locked rise in FMN^{VIP} activity and resulted in a significant increase in peak value after the perturbation, indicating rapid recruitment of FMN^{VIP} neurons upon sudden balance alterations ($p = 0.01$; Fig. 2H). Notably, we did not see a significant correlation between the post-perturbation peak of FMN^{VIP} activity and the animal's latency to postural recovery after perturbation ($r = -0.18$, $p = 0.39$; Fig. 2I), suggesting that FMN^{VIP} neurons were maximally recruited by the sudden balance perturbation; hence, the activity plateaued and not correlated with the animal's latency to postural recovery in each trial. We then asked whether these neurons were also activated when animals walked on a stable surface during in-cage locomotion. In-cage locomotion epochs were identified by tracking the head position of freely moving animals within their home-cage boundaries (Fig. 2J). For each epoch, we computed AUC during locomotion and compared it with AUC of a random time-matched epoch (ΔAUC = in-cage - random). Intriguingly, we did not observe a significant difference between locomotion and random epochs ($p = 0.24$; Fig. 2K-L), demonstrating that walking on a stable surface does not elicit FMN^{VIP} activity. This is consistent with the behavioral tests, which showed no change in general locomotion after FMN^{VIP} ablation. Together, our *in vivo* recording experiments indicated that FMN^{VIP} neurons are selectively activated during balance-demanding postural controls but not during general locomotion. Moreover, the degree of their activation is correlated with the level of balance required to maintain stability.

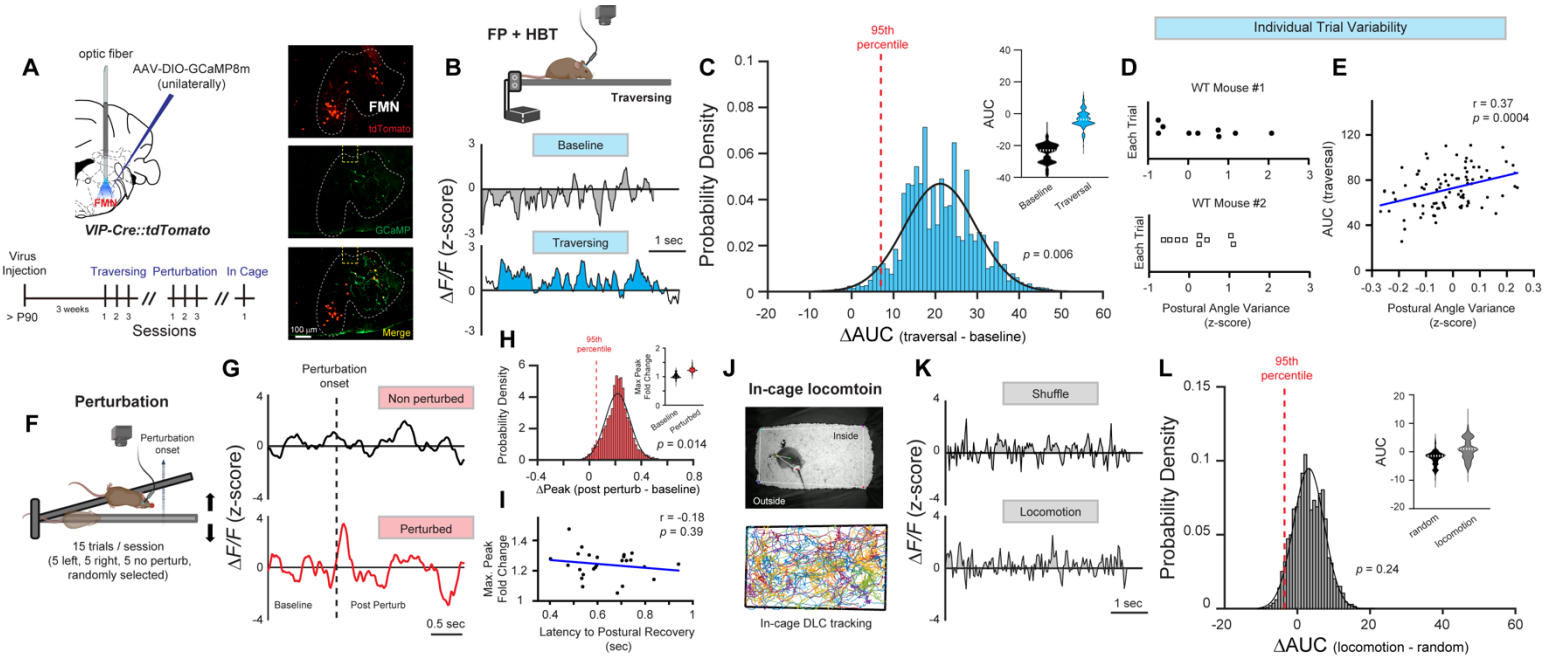

Figure 2. FMN^{VIP} neurons show elevated Ca^{2+} activity during traversal and perturbation but not during general locomotion.

(A) Left: unilateral injection of AAV-DIO-GCaMP8m into the FMN of VIP-Cre::Ai14 animals. An optic-fiber was implanted above the injection site of FMN (top). Experimental timeline (bottom). Right: representative images of FMN coronal section with FMN region outlined by a white dashed border and the yellow rectangular dashed box indicates the position of the optic-fiber. Top: tdTomato-labeled FMN^{VIP} neurons. Middle: GCaMP8m expression (green). Bottom: merged image showing co-localized cells.

(B-E) *In vivo* Ca^{2+} photometry of FMN^{VIP} activity during horizontal beam test traversal (FP + HBT traversal): **(B)** Schematic shows the animal traversing across narrow beam with fiber photometry recording. Representative z-scored ΔF/F traces illustrate the activity of FMN^{VIP} neurons during baseline and traversal epochs; shaded regions indicate the time-matched area under the curves (AUC). **(C)** The AUC during traversal was significantly elevated compared with baseline. Probability density plot shows the distribution of bootstrapped median ΔAUC values (ΔAUC = traversal - baseline, 10,000x, N = 6 animals; one-sided empirical test). The vertical dashed line marks its 95th percentile, and the inset violin plots show the distributions of bootstrapped median AUC values. Dashed horizontal lines indicate group means. **(D)** Representative plots of z-score postural-angle variance from different trials in two representative WT animals. **(E)** FMN^{VIP} population activity during traversal was positively correlated with the postural-

angle variance (Pearson correlation). Scatter plot shows bootstrapped mean of z-scored postural-angle variance and ΔAUC (traversal - baseline).

(F-I) *In vivo* Ca^{2+} photometry of FMN^{VIP} activity during balance perturbation on horizontal beam test (FP + HBT perturbation): (F) A brief horizontal displacement was delivered as an unexpected balance perturbation when the animal crossed a fixed position in the distal portion of the beam. **(G)** Representative z-scored ΔF/F traces illustrate the activity of FMN^{VIP} neurons during non-perturbed and perturbed trials. The vertical dashed line indicates perturbation onset. **(H)** Upon perturbation, Ca^{2+} peak amplitudes were significantly increased relative to baseline. Probability density plot shows the distribution of bootstrapped median ΔPeak values (ΔPeak = perturbation - baseline; 10,000x; N = 6 animals; one-sided empirical test). The vertical dashed line marks its 95th percentile, and the inset violin plots show the distributions of bootstrapped median normalized peak amplitudes for baseline and perturbation epochs. Dashed horizontal lines indicate group means. **(I)** FMN^{VIP} perturbation peak activity did not correlate with the latency to postural recovery (Pearson correlation). Scatter plot shows bootstrapped mean of latency to postural recovery and normalized perturbation peak amplitude.

(J-L) *In vivo* Ca^{2+} photometry of FMN^{VIP} activity during in-cage locomotion (FP + locomotion): (J) Top: in-cage locomotion assay, and white boundary lines mark the rectangular home-cage perimeter. Bottom: DLC-based head-tracking traces with each colored path represents one detected in-cage locomotion epoch. **(K)** Representative z-scored ΔF/F traces illustrate the activity of FMN^{VIP} neurons during random shuffled and in-cage locomotion epochs. Shaded regions indicate the time-matched AUCs. **(L)** Locomotion on a stable surface did not increase FMN^{VIP} population activity. Probability density plot shows the distribution of bootstrapped median ΔAUC values (ΔAUC = locomotion - random, 10,000x, N = 3 animals; one-sided empirical test). The vertical dashed line marks its 95th percentile, and the inset violin plots show the distributions of bootstrapped median AUC values for random and locomotion epochs. Dashed horizontal lines indicate group means. n.s., not significant.

6. Circuit mapping and post-hoc assessments reveal a cholinergic to GABAergic pathway between FMN^{VIP} and MVN neurons

To determine whether FMN^{VIP} neurons form direct synaptic connections with neurons in MVN, we employed a newly developed circuit tracing tool, the Trans-synaptic Anterograde Circuit Readout (TRACR), developed by Dr. Julie Lefbvre's lab, University of Toronto. TRACR allows trans-synaptic anterograde labeling to identify postsynaptic targets of FMN^{VIP} neurons in MVN (Fig. 3A). We unilaterally injected the Receiver virus (AAV-LaG17-SynNotch-FetR) and the Reporter virus (AAV-TRE-mRuby) into MVN of VIP-Cre animals. The Receiver virus drives the expression of an engineered SynNotch transmembrane receptor (carrying an intracellularly tagged FetR) in MVN neurons, and the Reporter virus contains the FetR-On TRE promoter, which drives the expression of mRuby when it is turned on by FetR. At the ipsilateral FMN, the Cre-dependent Sender virus (AAV-DIO-Nrx3b-GFP) was injected to selectively express Nrx3b-eGFP in FMN^{VIP} neurons (Fig. 3A-B). Once the Sender-expressing FMN^{VIP} axons contact the Receiver-expressing MVN neurons, the binding between Nrx3b-GFP and LaG17-SynNotch triggers proteolytic release of FetR from the SynNotch intracellular domain. The released FetR then translocates to the nucleus and activates mRuby expression under the TRE promoter, thereby labeling the postsynaptic neurons in MVN. Six weeks after the viral injections, we observed a significantly higher number of labeled neurons in MVN compared to the control without the Sender virus (Control: 37.3 ± 14.56; Reporter: 189.47 ± 36.89; $p = 0.03$; Fig. 3B-C)(172). Previous studies have reported that MVN contains a high density of inhibitory neurons (173,174); hence, we performed RNAscope *in situ* hybridization in MVN of WT samples using a probe against vesicular GABA transporter (vGAT), a marker of inhibitory neurons, and we confirmed that there was also a large proportion of vGAT-positive cells in MVN coordinate where FMN^{VIP} axons terminate (25.74% ± 4.16%; Fig. S2G-H). We then immunostained the TRACR-labeled samples for γ-aminobutyric acid (GABA) to examine

whether the FMN^{VIP}-targeted cells in MVN are GABAergic neurons. Our analysis showed that the majority of Reporter-labeled MVN neurons were GABAergic (75.07% ± 4.23%, Fig. 3D-E). By performing a shuffle-based analysis, we found that the TRACR-control samples (no Sender virus) showed significantly fewer co-localized cells with GABA than the TRACR-labeled samples ($p < 0.00001$, Fig. 3F). Also notably, the GABA co-localization ratios in the random shuffle were closely matched with the vGAT RNAscope quantification in WT samples (Fig. S2G-H). Altogether, the tracing experiments demonstrate that FMN^{VIP} neurons preferentially form synaptic connections with GABAergic neurons in MVN.

Given the molecular diversity of VIP neurons across the brain, we next asked which neurotransmitter FMN^{VIP} neurons express (175). In the neocortex, most VIP neurons are GABAergic interneurons that participate in disinhibitory microcircuit mechanisms. VIP interneurons, together with PV and SST interneurons, make up the major classes of inhibitory neurons across cortical circuits (153). However, these molecular markers do not always represent the neurotransmitters that the neurons express. PV-expressing neurons in the trigeminal complex have been shown to release glutamate to the thalamus and FMN, while SST-expressing neurons in the medial paralemniscal nucleus also release glutamate to their downstream targets (176). To determine the neurotransmitter identity of FMN^{VIP} neurons, we performed immunostaining for GABA on VIP-tdTomato labeled neurons in FMN. We observed almost no co-localization between FMN^{VIP} neurons and GABA (1.62% ± 0.94%; Fig. 3G-H). To further investigate this, we performed RNAscope for vGAT and glutamate decarboxylase 1 (GAD1) mRNA in FMN of WT animals. We found minimal expression of the inhibitory markers in FMN, despite clear vGAT and GAD1 labeling in adjacent brainstem nuclei and robust VIP mRNA labeling within FMN (VIP: 67.9 ± 8.39, vGAT: 3.77 ± 1.01; $p = 0.002$ (VIP vs vGAT); GAD1: 0.79 ± 0.39; $p = 0.035$ (VIP vs GAD1, Fig. S2A-B)). This pattern was consistent with observations in the GAD1-Cre::GFP transgenic mouse line, in which we also did not observe any labeled neurons in FMN (Fig. S2C-D). Given that glutamate expression has been reported in subsets of PV- and SST-expressing neurons

in subcortical regions, we next asked whether FMN^{VIP} neurons could be glutamatergic. We immunostained VIP-tdTomato labeled neurons in FMN for the excitatory neuronal marker, vesicular glutamate transporter 1 (vGlut1), and also observed very few co-localizations with FMN^{VIP} neurons (3.77% ± 0.70%; Fig 3I-J). We also performed RNAscope for vGlut1 mRNA in WT samples and still found minimal vGlut1 expression in FMN (vGlut1: 2.24 ± 0.82; p = 0.0043 (VIP vs vGlut1); Fig. S2A-B). Hence, we asked whether FMN^{VIP} neurons share the cholinergic identity of most motoneurons in FMN. We examined the expression of the cholinergic marker choline acetyltransferase (ChAT) in FMN^{VIP} neurons, and ChAT immunostaining showed strong co-localization with FMN^{VIP} neurons (91.42% ± 2.68%; Fig. 3K-L). The fraction of ChAT-positive neurons in FMN that expressed VIP only accounted for a small proportion of cholinergic neurons in FMN, indicating that FMN^{VIP} neurons are only a distinct subset of cholinergic neurons within FMN (18.72 ± 2.09; Fig. S2E-F).

6.1. FMN^{VIP} neurons contribute to posture and balance by cholinergic signaling

Having established that FMN^{VIP} neurons express the cholinergic neurotransmitter acetylcholine (ACh), we next asked whether ACh is released in MVN during postural maintenance. We unilaterally injected an ACh sensor-expressing viral construct (AAV-GRAB-ACh3.0) into MVN and implanted an optic fiber immediately dorsal to the injection site at the floor of the fourth ventricle (V4) to monitor ACh levels (Fig. 3M). GRAB-ACh3.0 is a GPCR-activation-based fluorescent reporter derived from the human M3 muscarinic ACh receptor, with a circularly permuted GFP inserted into its third intracellular loop. Upon binding to ACh, the sensor induces a conformational change that increases GFP fluorescence. Three weeks after the injection, we performed *in vivo* fiber photometry recordings while the animals traversed across the narrow beam in HBT (Fig. 3M-N) (177,178). We quantified the AUC of sensor ΔF/F signals during baseline and traversal for each

trial, similar to what is described above for Ca^{2+} imaging. We found that ACh release in MVN was significantly increased during beam traversal compared to the baseline ($p < 0.00001$; Fig. 3O). To further determine whether the amount of ACh release also corresponds to postural instability, we conducted a trial-by-trial correlation between traversal ACh release (ΔAUC) and postural-angle variance. Similar to the FMN^{VIP} population activity, it revealed a positive correlation, in which trials with greater wobbly traversal (higher instability) showed a larger release of ACh in MVN ($r = 0.23$, $p = 0.009$, Fig. 3P). We next tested whether ACh release in MVN is a general feature of locomotion by recording ACh levels in MVN while animals were freely moving in their home cage on a stable surface (in-cage locomotion). Quantifications of in-cage ΔAUC, as described for FMN^{VIP} population activity, showed no changes in ACh levels in MVN during this time ($p = 0.9043$; Fig. S2I). These analyses demonstrated that the increase of ACh release in MVN was not due to general locomotion, but it was specific to balance control.

Lastly, since MVN also receives cholinergic inputs from other regions, including the pedunculopontine tegmental nucleus (PPTg) (179), we next examined whether the balance-evoked ACh release in MVN arises specifically from FMN^{VIP} neurons. We combined ACh sensor recordings in MVN with chemogenetic (DREADDs) inhibition of FMN^{VIP} neurons. We unilaterally injected AAV-DIO-hM4Di-mCherry into FMN and AAV-GRAB-ACh3.0 into ipsilateral MVN of VIP-Cre animals, followed by optic-fiber implantation above the MVN injection site (Fig. 3Q-R). This enabled simultaneous *in vivo* measurement of ACh release in MVN during HBT traversal after inhibiting FMN^{VIP} neuronal activity. Three weeks later, each mouse completed two HBT traversal sessions on consecutive days, with one session following saline administration and the other with JHU treatment. We compared ΔAUC between saline-treated and JHU-treated trials and found that acutely inhibiting FMN^{VIP} neuronal activity significantly reduced the balance-evoked ACh release in MVN ($p = 0.04$; Fig. 3T). Furthermore, inhibition of FMN^{VIP} neuronal activity did not alter

the basal levels of ACh in MVN (Saline: 1.05± 0.21; JHU: 1.10 ± 0.21; p = 0.84; Fig. 3S), indicating that FMN^{VIP} neurons do not contribute to the general ACh levels in MVN when the animal's balance is not challenged. Together, the data suggest that FMN^{VIP} neurons provide a cholinergic drive that stabilizes posture through ACh-dependent signaling in MVN.

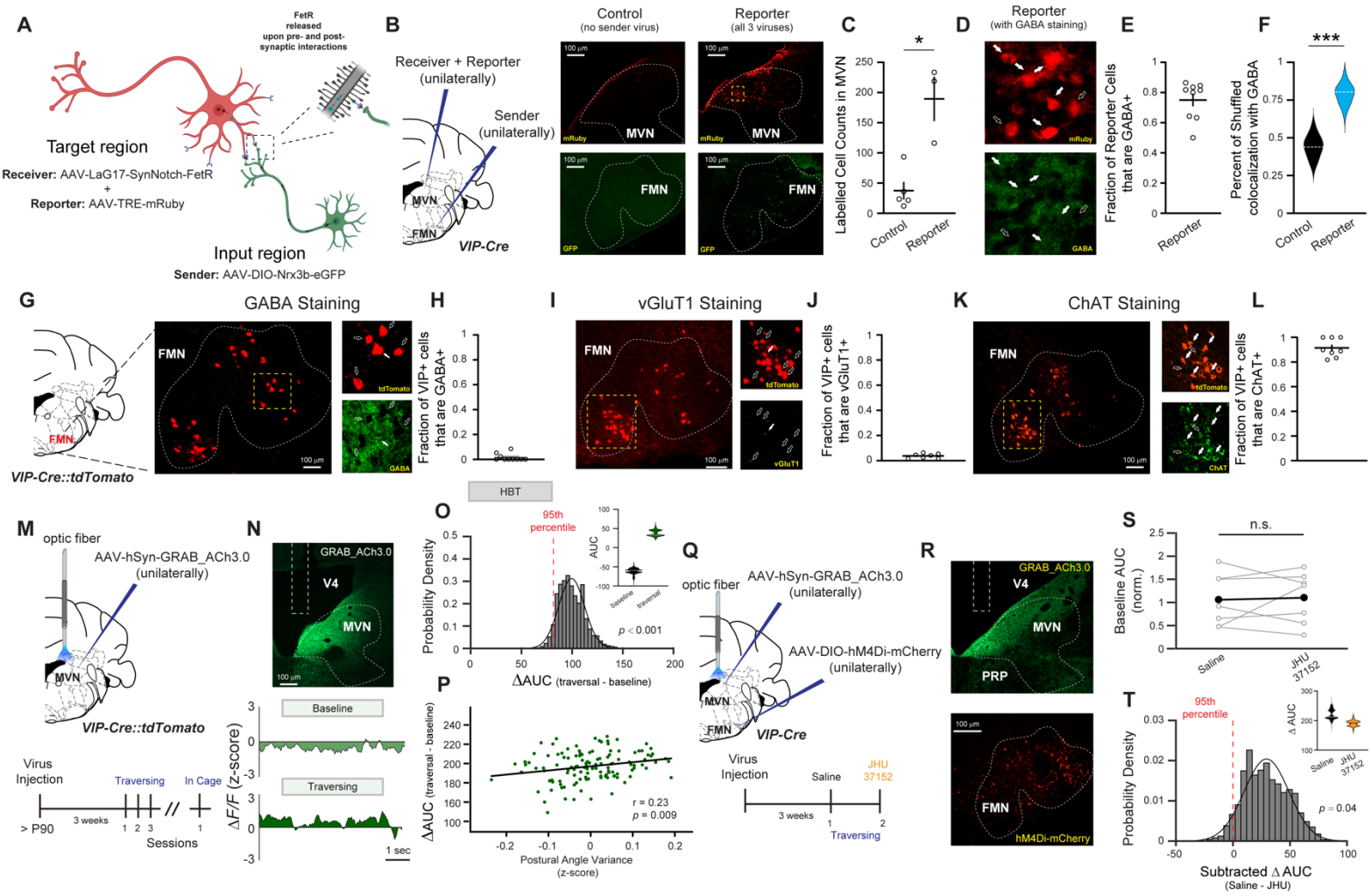

Figure 3. FMN^{VIP} neurons provide cholinergic input onto GABAergic MVN cells and regulate balance-evoked ACh release.

(A-F) Employing the Trans-synaptic Anterograde Circuit Readout (TRACR) to test FMN^{VIP} inputs onto MVN cells: **(A)** Schematic of the TRACR anterograde circuit-mapping system. **(B)** Left: VIP-Cre animals received unilateral injections of the Receiver virus (AAV-LaG17-SynNotch-FetR) and the Reporter virus (AAV-TRE-mRuby) into MVN. At the ipsilateral FMN, the Cre-dependent Sender virus (AAV-DIO-Nrx3b-GFP) was injected to drive Nrx3b-GFP expression selectively in FMN^{VIP} neurons. Right: Representative coronal sections compare control animals (Receiver + Reporter only) and TRACR reporter animals (all three viruses). Control animals showed very few mRuby-expressing cells in MVN and no GFP signals in FMN (left). Reporter animals showed a higher number of mRuby-expressing cells in MVN. The GFP-labeled cells in FMN confirmed Sender expressions in FMN (right). The yellow dashed box indicates the region shown at higher magnification in panel D. **(C)** Scatter plot shows the number of mRuby-expressing cells in MVN. Reporter animals showed a significantly higher number of TRACR-labeled cells than control animals (Control:

N = 5 animals; Reporter: N = 3 animals; two-tailed Mann-Whitney U test). **(D)** High-magnification images taken from the yellow dashed ROI in panel B (Reporter). Top: mRuby-expressing TRACR-labeled cells in MVN. Bottom: GABA immunostaining in the same region. Solid arrows denote $mRuby^+/GABA^+$ co-localized cells, and open arrows indicate $mRuby^+$ cells that did not co-localize with GABA. **(E)** Scatter plot shows the fraction of Reporter TRACR-labeled MVN cells that were $GABA^+$ (n = 9 samples). **(F)** Shuffled analysis demonstrated higher GABA co-localization in Reporter TRACR-labeled animals compared with control animals (one-sided empirical test). Dashed horizontal lines indicate group means. ***P < 0.001, *P < 0.05.

(G-L) Characterizing neurotransmitter expression in FMN^{VIP} neurons: (G) Representative images from VIP-Cre::Ai14 animals show tdTomato-labeled VIP cells and GABA immunostaining within FMN (dashed outline). The yellow dashed box marks the high-magnification region shown at right. In the enlarged panels, filled arrows indicate $VIP^+/GABA^+$ cells, and open arrows denote VIP^+ cells lacking GABA signals. **(H)** Fraction of VIP^+ FMN cells that showed low co-localization with GABA (n = 10 samples). **(I)** Representative images from VIP-Cre::Ai14 animals show tdTomato-labeled VIP cells and vGlut1 immunostaining within FMN (dashed outline). The yellow dashed box marks the high-magnification region shown at right. In the enlarged panels, filled arrows indicate $VIP^+/vGlut1^+$ cells, and open arrows denote VIP^+ cells lacking vGlut1signals. **(J)** Fraction of VIP^+ FMN cells that showed low co-localization with vGlut1 (n = 7 samples). **(K)** Representative images from VIP-Cre::Ai14 animals show tdTomato-labeled VIP cells and ChAT immunostaining within FMN (dashed outline). The yellow dashed box marks the high-magnification region shown at right. In the enlarged panels, filled arrows indicate $VIP^+/ChAT^+$ cells, and open arrows denote VIP^+ cells lacking ChAT signals. **(L)** Fraction of VIP^+ FMN cells that showed high co-localization with ChAT (n = 8 samples).

(M-P) *In vivo* photometry recording of ACh release in MVN during horizontal beam test traversal (FP + HBT traversal): **(M)** Top: schematic of unilateral ACh sensor recordings in MVN of VIP-Cre::Ai14 animals. AAV-hSyn-GRAB-ACh3.0 was injected into MVN, and an optic-fiber was implanted above the injection site. Bottom: The experimental timeline. **(N)** Top: representative GRAB-ACh3.0 expression (green) in MVN (dashed outline). The rectangular dashed box marks the optic-fiber tip. Bottom: Representative z-scored ΔF/F traces illustrate activity during baseline and traversal epochs; shaded regions indicate AUCs. **(O)** The AUCs during traversal were significantly higher than baseline. Probability density plot shows the distribution of bootstrapped median ΔAUC values (ΔAUC = traversal - baseline, 10,000x, N = 8 animals; one-sided empirical test). The vertical dashed line marks its 95th percentile, and the inset violin plots show the distributions of bootstrapped median AUC values for baseline and traversal epochs. Dashed horizontal lines indicate group means. **(P)** Traversal-evoked ACh release in MVN was positively correlated with the postural-angle variance (Pearson correlation). Scatter plot shows bootstrapped mean of z-scored postural-angle variance and ΔAUC (traversal - baseline).

(Q-T) Chemogenetic silencing of FMN^{VIP} neurons followed by *in vivo* photometry recording of ACh release in MVN during horizontal beam test traversal (hM4Di + FP + HBT traversal): **(Q)** Top: schematic of the dual-viral injections. In VIP-Cre animals, AAV-hSyn-GRAB-ACh3.0 was injected unilaterally into MVN with an optic-fiber implanted above the injection site, and AAV-DIO-hM4Di-mCherry was injected ipsilaterally into FMN. Bottom: The experimental timeline shows two HBT traversal + FPS sessions performed on consecutive days with Saline (Day 1) and JHU (Day 2). **(R)** Top: A representative image shows GRAB-ACh3.0 expression (green) in MVN (dashed outline), and the rectangular dashed box marks the optic-fiber tip above MVN injection site. Bottom: A representative image shows hM4Di mCherry-expressing cells within FMN. **(S)** Normalized AUC during baseline epochs. The ACh baseline levels did not significantly change following FMN^{VIP} activity inhibition. (N = 7 animals; paired permutation test). **(T)** Balance-evoked ACh release was significantly reduced following FMN^{VIP} activity inhibition. Probability density plot shows the distribution of bootstrapped median ΔAUC values (ΔAUC = Saline ΔAUC - JHU ΔAUC, 10,000x, N = 7 animals; one-sided empirical test). The vertical dashed line marks its 95th percentile, and the inset violin plots show the distributions of bootstrapped median ΔAUC values for Saline and JHU sessions. Dashed horizontal lines indicate group means. n.s., not significant.

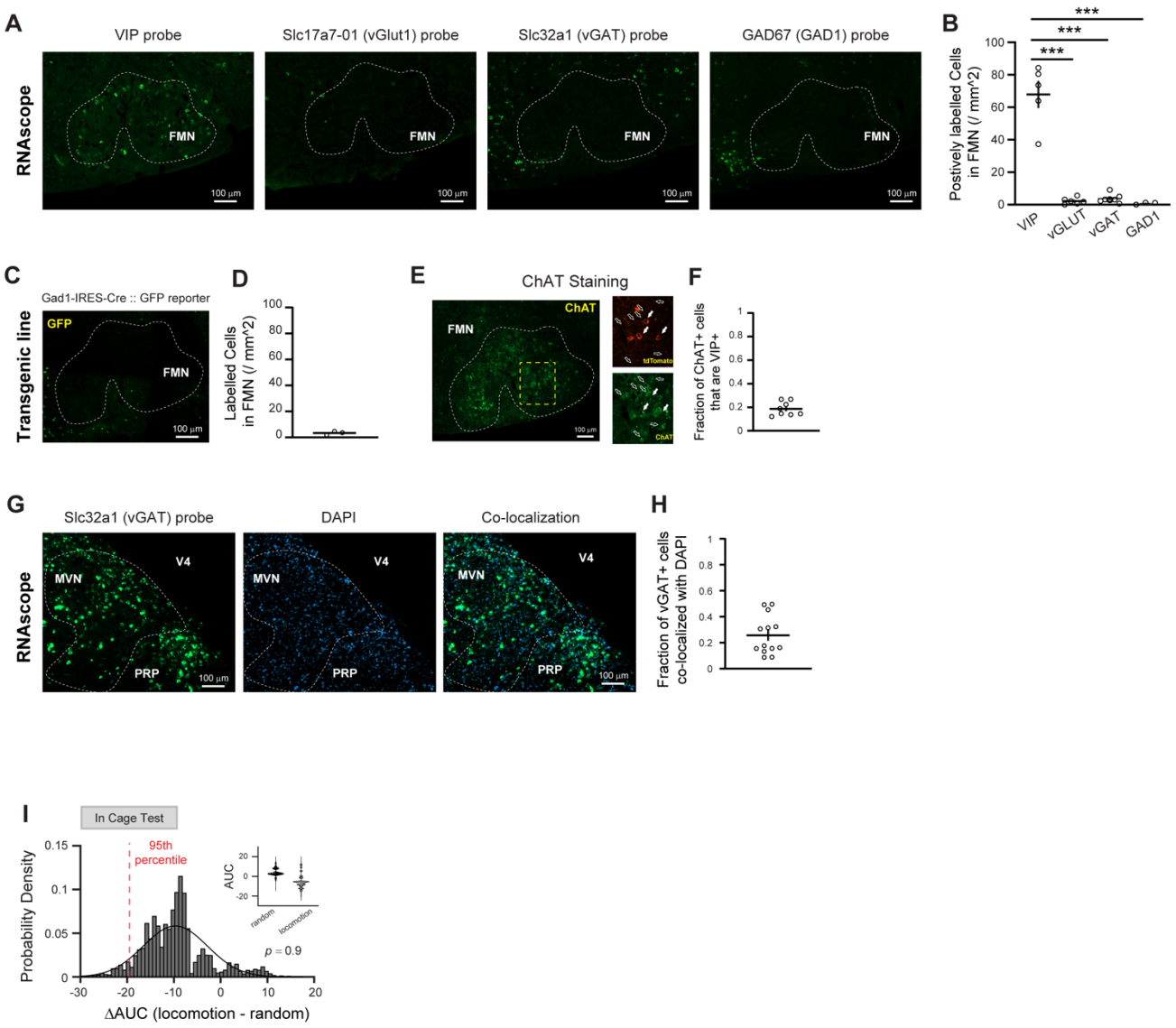

Supplementary Figure 2.

(A-C) RNAscope and reporter labeling reveal very few glutamatergic and GABAergic neurons in FMN: (A) RNAscope images from WT animals show probe-specific labeling within FMN (dashed outline). Separate panels display VIP, Slc17a7 (vGlut1), Slc32a1 (vGAT), and Gad67 (GAD1) probes. **(B)** Scatter plot shows the density of probe-positive cells within FMN, and VIP density was significantly higher than vGlut1-, vGAT-, and GAD1- (VIP: n = 5 samples; vGlut1: n = 5 samples; vGAT: n = 7 samples; GAD1: n = 3 samples; two-tailed Mann-Whitney U test). ***P < 0.001. **(C)** Coronal section from a Gad1-IRES-Cre::GFP reporter animal shows transgenic labeling of GABAergic (GAD1-labeled) cells outside, but not within FMN (dashed outline). **(D)** Scatter plot shows the density of GFP-labeled cells within FMN (n = 3 samples).

(E-F) VIP expresses within a small subset of cholinergic cells in FMN. (**E)** Representative images from VIP-Cre::Ai14 animals show tdTomato-labeled VIP cells and ChAT immunostaining within FMN (dashed outline). The yellow dashed box marks the high-magnification region shown at right. In the enlarged panels, filled arrows indicate $ChAT^+$ cells that co-express VIP ($ChAT^+/VIP^+$), and open arrows denote $ChAT^+$ cells lacking VIP signal. **(F)** Fraction of $ChAT^+$ FMN cells that were VIP^+ indicates that only a small subset of cholinergic cells in FMN express VIP (n = 7 samples).

(G-H) vGAT expresses in a large population of cells in MVN. (G) Left: An RNAscope image from a WT animal shows Slc32a1- (vGAT-positive) probe labeling (green) within MVN (dashed outline). Middle: DAPI-positive nuclei (blue). Right: A merged image shows vGAT probe and DAPI co-localized cells **(H)** Fraction of $DAPI^+$ MVN cells that co-localized with vGAT ($DAPI^+/vGAT^+$) within MVN (n = 13 samples).

(I) ACh release in MVN does not increase during in-cage locomotion: Locomotion on a stable surface did not increase Ach level in MVN. Probability density plot shows the distribution of bootstrapped median ΔAUC values (ΔAUC = locomotion - random, 10,000x, N = 5 animals; one-sided empirical test). The vertical dashed line marks its 95th percentile, and the inset violin plots show the distributions of bootstrapped median AUC values for random and locomotion epochs. Dashed horizontal lines indicate group means.

7. Anatomical dissection of inputs and outputs of the FMN^{VIP} -MVN pathway

Our immunostaining data indicate that FMN^{VIP} neurons constitute a distinct subpopulation of cholinergic neurons within FMN. This raised the question of whether they receive inputs from specific brain regions that could delineate how FMN^{VIP} neurons contribute to postural control. We employed monosynaptic retrograde rabies virus (RV) tracing and performed brain-wide mapping to identify the presynaptic regions to FMN^{VIP} neurons. A Cre-dependent AAV helper virus (AAV-DIO-TVA-P2A-eGFP-2A-oG) was unilaterally injected into FMN of VIP-Cre animals. Three weeks later, the EnvA-pseudotyped rabies virus (EnvA-RVΔG-mCherry) was injected at the same site (Fig. 4A). The helper virus drove the expression of the avian leukosis virus subgroup A receptor (TVA) in FMN^{VIP} neurons, permitting the EnvA-pseudotyped rabies to enter, and also supplied rabies glycoprotein (oG) to enable trans-synaptic spread and mCherry labeling of presynaptic input neurons (Fig. 4B). One week after the rabies delivery, brain samples were harvested, and coronal sections were collected at 100 μm intervals. Images were registered to the Allen Mouse Brain Atlas using QuickNII/VisuAlign workflow (180), and RV-mCherry labeled input neurons were automatically detected across the whole brain with an interactive machine-learning pipeline (ilastik) (total cells: 2195; Fig. 4C) (181,182). Rostro-caudal analysis showed a pronounced input distribution in the caudal regions, with almost all the presynaptic neurons located in the hindbrain (forebrain: 3.04% ± 0.90%; hindbrain: 96.96% ± 0.90%; $p < 0.0001$; Fig. 4D). Among the labeled regions, the largest fractions of inputs arose from caudal medullary reticular nuclei, particularly the gigantocellular (Gi), intermediate (IRt), and parvicellular (PARN) reticular nuclei (Gi: 24.64% ± 9.11%; IRt: 21.35% ± 3.62%; PARN: 18.47% ± 7.17%; Fig. 4E-G). These regions are classically described as key premotor hubs that integrate multimodal sensory signals and regulate posture and locomotor tone (15,183,184). In comparison, the strongest forebrain contributors were the medial amygdalar nucleus (MA/MeA), zona incerta (ZI), and piriform-amygdalar area (PirA), but each only accounted for a small fraction of the total FMN^{VIP} input neurons (MA: 2.05% ± 1.37%; ZI: 0.18% ± 0.18%; PirA: 0.16% ±

0.16%; Fig. 4E-G). Collectively, the rabies tracing revealed that FMN^{VIP} neurons are embedded within a hindbrain-centered sensorimotor network with limited forebrain input. This pattern positions FMN^{VIP} neurons as a key component of a convergence hub, which has never been reported, that links the reticular nuclei and vestibular nuclei for posture and balance control.

Lastly, we asked whether FMN^{VIP} neurons or their downstream GABAergic neurons in MVN project directly to spinal motor circuits, which can control the muscle pools responsible for posture and balance. Previous studies have shown that subsets of MVN neurons give rise to medial vestibulospinal projections (MVST) that terminate in cervical spinal segments, where they mediate vestibulocollic reflexes (VCR) for balance (61,185). To identify these spinal projections, we unilaterally injected AAV-DIO-GFP together with AAV-Cre into MVN of WT animals to unbiasedly label all the neurons in MVN. Three weeks later, we dissected the cervical spinal cord and immunostained for ChAT to label cholinergic motoneurons in the ventral horn. We observed dense MVN-projecting GFP-positive axons throughout both the dorsal and ventral horns of the cervical spinal cord, including fibers closely apposed to ChAT-positive motoneurons (Fig. 4H). To determine whether FMN^{VIP} neurons also project to the cervical spinal cord, we unilaterally injected AAV-DIO-GFP into FMN of VIP-Cre animals to selectively label FMN^{VIP} neurons. In this case, we did not observe any GFP-positive axonal projections in the cervical spinal cord (Fig. 4I). Lastly, we examined cervical spinal cord sections from the TRACR-labeled samples (Fig. 4J), in which MVN neurons targeted by FMN^{VIP} neurons (identified as GABAergic) were labeled with mRuby. Similar to FMN^{VIP} neurons, we did not observe any axonal projections in the spinal cord (MVN-GFP: 3.98 ± 0.26; FMN^{VIP}: 1.531 ± 0.01; TRACR: 1.13 ± 0.002; $p < 0.0001$; Fig. 4K). Together, these anatomical tracing studies demonstrate that a population of neurons in MVN provides the primary descending vestibulospinal output to cervical circuits (MVST), but neither FMN^{VIP} neurons nor their downstream GABAergic neurons in MVN project directly to the cervical

spinal cord. This pattern suggests that the FMN^{VIP}-MVN pathway acts as an upstream modulator of vestibulospinal circuits, in which FMN^{VIP} neurons target GABAergic neurons in MVN via ACh release to rapidly inhibit the spinal-projecting MVN neurons, and thereby regulate balance and postural maintenance.

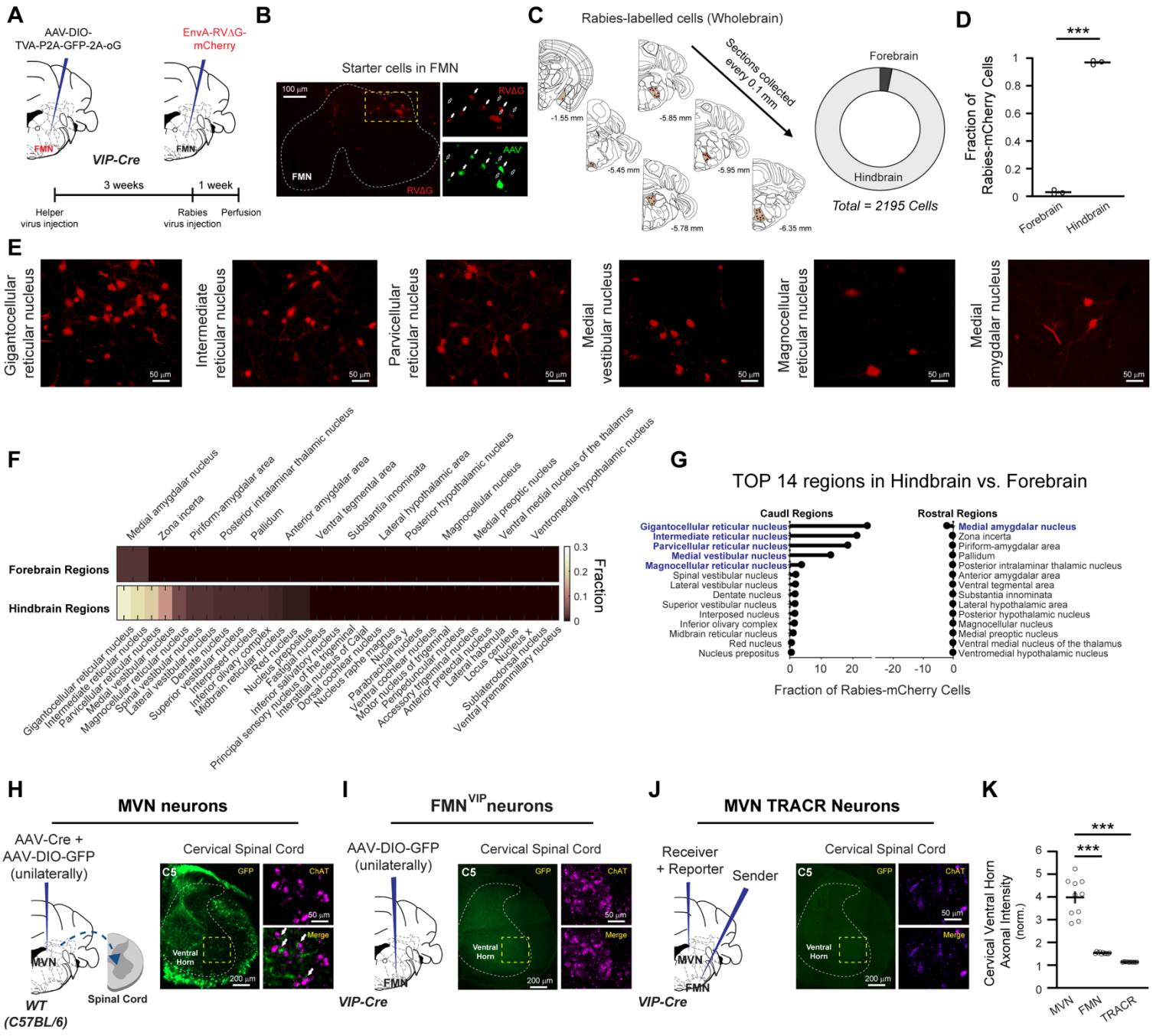

Figure 4. Rabies tracing shows most inputs to FMN^{VIP} neurons are from the hindbrain, and FMN^{VIP} or TRACR-labeled cells do not directly target the spinal cord.

(A-G) Monosynaptic rabies tracing from FMN^{VIP} neurons. (A) Top: Experimental setup. VIP-Cre animals received unilateral FMN injections of helper viruses (AAV-DIO-TVA-P2A-GFP-2A-oG), followed three weeks later by EnvA-RVΔG-mCherry delivery. Bottom: experimental timeline. **(B)** A representative FMN section shows RVΔG-mCherry-

expressing cells within FMN (dashed outline). The yellow dashed box marks the region shown at higher magnification on the right. Top: RVΔG mCherry-expressing cells. Bottom: helper GFP-expressing cells in the same region. Solid arrows denote starter FMN^{VIP} neurons co-labeled for $RV\Delta G^{+}$/$helper^{+}$ ($mCherry^{+}$/GFP^{+}), and open arrows indicate presynaptic-only RVΔG-labeled cells. **(C)** Example atlas-registered whole-brain mapping of RVΔG-labeled presynaptic cells. Coronal sections were imaged every 0.1 mm along the AP neuraxis. Right: Doughnut plot shows the mean fraction of RVΔG-labeled cells located in the forebrain (rostral; > -4.5 mm from bregma) and the hindbrain (caudal; ≤ -4.5 mm from bregma) across animals (mean total ≈ 2,195 cells; N = 3 animals). **(D)** Scatter plot shows the fraction of RVΔG-labeled cells located in the hindbrain that was significantly higher than the labeled cells in the forebrain (N = 3 animals; Welch's t-test). **(E)** Representative high-magnification images of RVΔG mCherry-expressing presynaptic cells in major caudal input regions, including the gigantocellular (Gi), intermediate (IRt), parvicellular (PARN), and magnocellular (MARN) reticular nuclei and the medial vestibular nucleus (MVN). A representative image also illustrates presynaptic labeling in the medial amygdalar nucleus (MeA). **(F)** Heat map shows the average fraction of RVΔG-labeled cells across all anatomically identified regions (N = 3 animals), plotted separately for the hindbrain and forebrain regions. Each value represents the fraction of total labeled cells. **(G)** Ranked bar plot of the top input regions. ***P < 0.001.

(H-K) Descending projections from MVN, FMN^{VIP}, and TRACR-labeled cells in the cervical spinal cord: (H) Left: schematic of unilateral AAV-DIO-GFP + AAV-Cre injections targeting MVN in WT animals. Right: A representative image of a cervical C5 section shows GFP-positive axons from MVN with ChAT immunostaining within the ventral horn (dashed outline). The yellow dashed box marks the high-magnification region shown at right. Solid arrows indicate GFP-positive axons apposed to ChAT-positive motoneurons. **(I)** Representative images from VIP-Cre animals after unilateral AAV-DIO-GFP injection into FMN. The representative image of a C5 cervical section shows no detectable GFP-positive axons apposed to ChAT-positive motoneurons within the ventral horn. The yellow dashed box marks the high-magnification region at right. **(J)** Representative images from VIP-Cre animals after unilateral TRACR virus injections into FMN and MVN. The representative image of a C5 cervical section shows no TRACR-positive axons (mRuby-positive, green channel) near ChAT-positive motoneurons within the ventral horn. The yellow dashed box marks the high-magnification region at right. **(K)** Scatter plot shows normalized axonal fluorescence intensity in the cervical ventral horn. MVN projections showed significantly higher fluorescence intensity than both FMN^{VIP} and TRACR-MVN groups (n = 10 samples per group; two-tailed Mann-Whitney U test). ***P < 0.001.

CHAPTER 3: DISCUSSION AND CONCLUSION

When balance is challenged, the vestibular nuclei generate responses to correct posture within tens of milliseconds to prevent a fall. In this thesis, we have identified a previously unrecognized population of VIP-expressing neurons in FMN that project to MVN, unveiling a new pathway in the brainstem that contributes to this rapid postural control. Ablating or transiently silencing FMN^{VIP} neurons disrupted postural balance without affecting general motor and oculomotor functions. Anatomical and molecular examinations demonstrated that FMN^{VIP} neurons are cholinergic neurons, and they are synaptically connected with GABAergic neurons in MVN. Photometry Ca^{2+} recordings of FMN^{VIP} population activity and their ACh release in MVN revealed that FMN^{VIP} activation drives ACh release in MVN when balance is in demand. Most importantly, the magnitude of FMN^{VIP} activity and ACh release were correlated with the degree of postural instability. Monosynaptic rabies tracing revealed that FMN^{VIP} neurons receive inputs mainly from hindbrain regions, with the strongest inputs arising from the reticular nuclei; hence, the identification of the FMN^{VIP}-MVN pathway provides a bridge that links the reticular nuclei with vestibular nuclei (VN) that directly drive spinal circuits for postural control.

1. Beyond cortical VIP interneurons: brainstem VIP-expressing cholinergic neurons in the facial motor nucleus (FMN)

Systematic screening of VIP-Cre::Ai14 reporter animals revealed an unexpected cluster of VIP-expressing neurons in FMN with axons oriented toward the ipsilateral MVN (Fig. 1A-C). RNAscope staining in adult animals (>P90) confirmed robust VIP mRNA expression in FMN, demonstrating that this population is maintained in the mature brainstem (Fig. S2A). Consistent with our observations, the Allen Mouse Brain Atlas

shows similar discrete VIP mRNA signals within FMN (Allen Institute for Brain Science, 2024; experiment ID: 77371835), and the Human Protein Atlas reports moderate to strong VIP immunoreactivity in the medulla and pons that labels VIP-positive cells in FMN (155). However, the neurotransmitter diversity, circuit connectivity, and behavioral function of FMN^{VIP} neurons have remained undiscovered. In the neocortex, VIP-, PV-, and SST-expressing interneurons form a disinhibitory motif in which VIP-expressing neurons preferentially inhibit local inhibitory neurons to regulate the activity of pyramidal neurons (153,186). In contrast to this cortical microcircuit motif, we found that FMN lacks detectable PV- and SST-expressing cells (Fig. S1A-C). RNAscope showed FMN also does not express vGAT and GAD1 mRNAs (Fig. S2A-B), indicating that FMN^{VIP} neurons are unlikely involved in disinhibiting local circuits within FMN. However, in VIP-Cre::Ai14 animals, we did observe tdTomato-labeled axonal fibers within FMN itself, so FMN^{VIP} neurons may still modulate local circuits through ACh release, a possibility that warrants future testing. Consistent with our observation of long-range FMN^{VIP} projections to MVN, work in other systems has shown that neurons expressing classical interneuron markers can also function as long-range projection neurons. Distinct VIP-expressing neuronal populations in other brain regions give rise to long-range projections to cortical and subcortical targets, including the auditory and motor cortices, hippocampus, thalamus, amygdala, and hindbrain, where they modulate distant targets rather than local microcircuits (187–189). In the motor and auditory cortices, VIP-expressing GABAergic neurons send long-range projections to the dorsal striatum, amygdala, and contralateral cortex. These inhibitory projections are thought to shape the activity in distant motor and limbic circuits and modulate movement- and emotion-related processing in these targets (190). Comparable long-range inhibitory projections have also been described for SST- and PV-expressing neurons. SST-expressing inhibitory neurons in the medial entorhinal cortex send long-range projections to the hippocampal CA1, where they preferentially target dendrite-projecting interneurons that provide distal dendritic inhibition of pyramidal neurons and shape spatial coding in CA1. In the auditory and motor cortices,

SST-expressing neurons form inhibitory corticostriatal pathways that directly inhibit spiny projection neurons in the dorsal striatum and modulate striatal output and motor activity (191–193). Similarly, PV-expressing neurons in the medial prefrontal cortex (mPFC) send long-range callosal inhibitory projections to the contralateral mPFC. These projections synchronize interhemispheric gamma activity, reshape prefrontal network dynamics, and they are required for behavioral flexibility during rule-shift learning (188). Together, these examples show that neurons defined by classical interneuron markers can exert powerful long-range influence on distant circuits. However, despite forming a long-range projection, FMN^{VIP} neurons are not GABAergic. GABA immunostaining showed no co-localization with VIP-expressing neurons in FMN (Fig. 3G-H). Consistently, RNAscope probing for the GABAergic markers, vGAT and Gad1, also did not detect expression of these mRNAs in FMN. Lastly, the Gad1-IRES-Cre::GFP mouse line likewise exhibited no Gad1-labeled cells in this nucleus (Fig. S2A-D). Instead, several lines of evidence suggest that VIP-expressing neurons in FMN can be glutamatergic. In the inferior colliculus, glutamatergic VIP-expressing neurons send long-range axons to the auditory thalamus and brainstem, as well as to the superior colliculus and periaqueductal gray. These relays allow them to influence auditory computations across multiple downstream regions (194). VIP-expressing neurons have also been identified in the thalamus, amygdala, and hindbrain, where they exert excitatory or modulatory control over local and long-range targets (195–197). SST-expressing glutamatergic neurons in the lateral and ventrolateral periaqueductal gray send long-range excitatory projections to the rostral ventromedial medulla. Activation of this pathway promotes mechanical and thermal hypersensitivity in neuropathic pain models, whereas its inhibition alleviates pain (198). In parallel, PV-expressing glutamatergic neurons in the entopeduncular nucleus project to motor thalamus and brainstem, which provide a major sensorimotor output channel of the basal ganglia (199). However, our immunostaining for vGlut1 did not show co-labeling with FMN^{VIP} neurons (Fig. 3I-J), and RNAscope probing for vGlut1 also did not show any mRNA expression within FMN (Fig. S2A-B). Given FMN's cholinergic

milieu and the absence of GABAergic and glutamatergic labeling in VIP-expressing neurons, we next asked whether FMN^{VIP} neurons share the cholinergic identity of the broader motoneuron pool. Immunostaining for ChAT revealed dense cholinergic labeling throughout FMN, and the vast majority of FMN^{VIP} neurons co-expressed ChAT, indicating that FMN^{VIP} neurons are predominantly cholinergic. Conversely, only ~20% of ChAT-positive FMN neurons were VIP-labeled, identifying FMN^{VIP} neurons as a molecularly distinct VIP-ChAT subpopulation within the larger ChAT-positive motoneuron pool in FMN (Fig. 3K-L & S2E-F). VIP-expressing neurons that co-express ChAT have also been reported in cortex. A sparse subset of ChAT-VIP interneurons resides in the superficial layers of mPFC, where they provide fast cholinergic excitation to nearby interneurons and pyramidal neurons via nicotinic receptors (200,201). Behaviorally, these cortical ChAT-VIP neurons support sustained attention independently of basal forebrain cholinergic input.

2. FMN^{VIP} neurons form a reticulo-vestibular circuit for balance control

Across species, FMN afferent organization differs markedly. In non-human primates, anterograde tracing from multiple frontal motor areas demonstrates dense, topographically organized corticobulbar projections to musculotopically defined subsectors of FMN. These cortical projections provide a structural basis for fine voluntary control of facial musculature (202,203). In rodents, retrograde tracing from FMN reveals dense inputs from the midbrain, pontine, and medullary premotor nuclei but only sparse cortical labeling (141,204,205). Recent anterograde studies from vibrissa and orofacial motor cortex show that direct corticofacial projections are weak and largely restricted to whisker motoneurons (vibrissae-projecting FMN (vFMN)). However, most cortical outputs target the intermediate reticular nucleus (IRt) and the oral and rostral spinal trigeminal nuclei (SpVO and SpVIr) that relay signals to FMN, indicating that cortical influence on FMN is largely indirect in rodents (142). Our rabies tracing aligns with the rodent literature, in which FMN activity is chiefly governed by hindbrain regions (206). Previous rodent maps identified the reticular nuclei as

the major input source to vFMN. In these studies, monosynaptic rabies tracing from neurons in vFMN revealed a compact input network in the intermediate (IRt) and gigantocellular (Gi) reticular nuclei. Trigeminal and respiratory hubs, including SpV, the Kölliker-Fuse nucleus (KF), pre-Bötzinger complex (preBötC), and Bötzinger complex (BötC), were also labeled but with smaller contributions. They also performed retrograde tracing from all neurons in FMN and observed the same input regions, along with additional labeled cells in the reticular nuclei (206). Our FMN^{VIP} monosynaptic rabies results yielded a similar map, in which the densest inputs arose from IRt and Gi. This suggests that the IRt and Gi neurons we identified as presynaptic to FMN^{VIP} neurons likely correspond to the same additional labeled cells in the reticular nuclei labeled in whole-FMN retrograde tracing in that study (Fig.4A-G). Interestingly, none of the trigeminal or respiratory hubs identified in the vFMN input map were detected in our dataset, indicating that FMN^{VIP} neurons form a specific input-defined population that is distinct from other FMN motoneurons. Similarly, the dorsal medullary reticular formation (MdD), a trigeminal sensorimotor interface adjacent to the spinal trigeminal nucleus (SpC), was also absent in the FMN^{VIP} dataset. Instead, we detected labeling in the medial, spinal, and lateral vestibular nuclei (MVN, SVN, LVN). This pattern is consistent with classic retrograde studies showing that neurons in MVN project to FMN, the cell types of the FMN neurons receiving this vestibulofacial input were not examined (204). We also found labeling in the parvicellular and magnocellular reticular formations (PARN and MARN), historically grouped as the parvocellular reticular nucleus (PCRt). The strong representation suggests that while IRt and Gi act as general facial premotor hubs, PARN likely functions as a cranial premotor region that provides FMN input for head and neck control (15,17,65,184), whereas MARN provides a major source of reticulospinal drive for postural tone, locomotor rhythm generation, and balance control. These differences in input regions of FMN^{VIP} neurons, compared with previously described vFMN maps, mark the differential role of FMN^{VIP} neurons in regulating balance rather than orofacial control. Future studies will

involve testing how PARN and MARN subdivisions connect with FMN^{VIP} neurons and the vestibular nuclei. Pathway-specific manipulations that selectively silence upstream vestibular or reticular partners and record the activity of FMN^{VIP} neurons during balance behavior could help to identify the circuit directionality. These experiments could assess reciprocal vestibular feedback and establish the causal architecture of the proposed reticulo-vestibular linkage.

Consistent with their positioning in the reticulo-vestibular circuits, the activity of FMN^{VIP} neurons was tightly correlated with the degree of balance instability. During walking on a stable surface, when head and body motion are well controlled and balance demands are low, vestibular drive to postural pathways, including those that give rise to medial vestibulospinal outputs (MVST), remains relatively low (10). This is consistent with our Ca^{2+} photometry recordings showing no changes in FMN^{VIP} activity during in-cage locomotion on a stable surface (Fig. 2J-L). This also aligns with our ablation assays, in which ablating FMN^{VIP} neurons did not affect general motor performance across standard tests (Fig. S1G-I). Together, the lack of FMN^{VIP} recruitment during walking on a stable in-cage surface and the preserved general motor performance following their ablation indicates that FMN^{VIP} neurons are not required when balance demands are low. In contrast, during the narrow-beam traversal, the postural system needs to operate in a higher-precision regime, in which small displacements of the center of mass relative to the support surface can destabilize body postures. Hence, a continuous recalibration of sensory weighting is required. As limb-related proprioceptive cues become less reliable on the narrow, unstable surface, the control system increases the relative gain assigned to vestibular signals. This state-dependent shift is a hallmark of sensory reweighting in postural control (21,207,208). Consistent with this framework, MVN and FMN^{VIP} ablation increased postural-angle variance (wobbling) during the balance-demanding beam traversal (Fig. 1L-P), a phenotype of impaired vestibular-dependent postural stabilization, reinforcing the established role of MVN in balance and implicating FMN^{VIP}

neurons as an important component of this system (209). Furthermore, we found that FMN^{VIP} activity increased significantly during balance traversal, and the level of the population response was correlated with the degree of postural instability (Fig. 2B-E), suggesting a graded engagement of these neurons in vestibular-mediated posture control. This proportional activation mirrors the scaling of vestibular drive within the system and the increased requirement for descending commands from MVN (via the MVST) to cervical and upper-thoracic segments as postural control becomes more dependent on balance (210). Moreover, sudden balance perturbation evoked a sharp increase in FMN^{VIP} activity, and the degree of activity did not correlate with the latency of the postural recovery (Fig. 2F-I). This observation suggests that under sudden balance perturbations, the system shifts from the graded modulation to all-or-none recruitment of FMN^{VIP} neurons to prevent imminent loss of balance. This aligns with established models of postural control, in which small deviations from upright stance, such as those occurring during beam traversal, are corrected by low-amplitude reflex responses (low-gain loops) in spinal and brainstem circuits, including MVN (210). In contrast, when the degree of perturbation increases and the vestibular error signals at MVN become larger, the system engages high-gain vestibulospinal and reticulospinal responses to restore equilibrium (210,211). This relationship indicates that FMN^{VIP} activity follows the established state-dependent patterns of MVN recruitment during balance control.

Furthermore, ACh release in MVN increased during balance tasks but not during walking on a stable surface. The ACh release correlated positively with the level of instability, mirroring the proportional rise in FMN^{VIP} activity with balance demand (Fig. 3O-P & S2I). Chemogenetic silencing of FMN^{VIP} neurons markedly reduced the balance-evoked ACh increase in MVN without changing the basal level of ACh (Fig. 3S-T), indicating a state-dependent ACh release by FMN^{VIP} neurons during postural demand. The remaining levels of balance-evoked ACh in MVN after FMN^{VIP} silencing could arise from the pedunculopontine and laterodorsal tegmental nuclei (PPTg/LDTg) inputs to MVN (121,212,213). These PPTg/LDTg systems have

well-established roles in arousal, suggesting that they provide a diffuse, state-dependent modulatory background rather than the precise, balance-locked ACh release mediated by FMN^{VIP} neurons. Thus, within the broader hindbrain cholinergic architecture, these results suggest that FMN^{VIP} neurons are uniquely positioned to supply balance-specific modulations that dynamically adjust vestibular output when postural stability is at risk.

3. Cholinergic control of MVN by FMN^{VIP} neurons

The TRACR results revealed a direct connection between FMN^{VIP} neurons and MVN, and the post-hoc immunostaining identified most of the TRACR-labeled MVN neurons as GABAergic cells (Fig. 3A-F). This aligns with the whole-brain rabies tracing study identifying FMN among putative presynaptic sources to MVN GABAergic neurons (106). However, the work did not further identify the cell types of the input cells in FMN. This thesis adds new insight to these large-scale tracing studies by revealing a specific subpopulation of neurons in FMN (FMN^{VIP} neurons) that provides ACh inputs to GABAergic neurons in MVN. One question that remains is how FMN^{VIP}-ACh signaling shapes MVN output. It is known that ACh acts on two receptor families, ionotropic nicotinic and metabotropic muscarinic receptors, and both are expressed in MVN. Studies show MVN GABAergic neurons prominently express α7-containing nicotinic receptors, whereas glutamatergic neurons express non-α7 nicotinic receptors (214). Functionally, α7 activation produces rapid, transient depolarization of inhibitory neurons, which is capable of shaping the timing and gain of vestibular responses on millisecond timescales, such as the fast postural adjustments mediated by FMN^{VIP} neurons. Future work using pharmacological receptor blockade with selective α7 antagonists (e.g., methyllycaconitine or α-bungarotoxin) could test whether disrupting α7-mediated signaling induces the wobble-like beam traversal phenotype observed after FMN^{VIP} silencing (Fig. 1V) (215). In contrast, muscarinic receptors

provide slower, modulatory control. In MVN, M2 (Gi/o) and M3 (Gq) subtypes are both expressed but have divergent functions. Presynaptic M2 suppresses vestibular-afferent glutamatergic EPSCs, whereas postsynaptic M3 increases the intrinsic excitability of cerebellum-projecting MVN neurons (122). Both receptors change the strength and firing of MVN neurons over hundreds of milliseconds to seconds. The slower modulation likely supports the tuning of vestibular excitability or sensorimotor gain over a longer period of time, rather than the immediate balance-locked responses attributed to FMN^{VIP} signaling (28). In addition to ACh, VIP peptide itself could act as a co-transmitter via VPAC1 or VPAC2 receptors, both of which are Gs-coupled and signal through cAMP and ERK pathways. In other systems, such as the suprachiasmatic nucleus and hippocampus, VIP-VPAC signaling also operates on slow, modulatory timescales, and they function to reshape network synchrony, excitability, and transcriptional programs rather than immediate synaptic transmission (216). Given the short latency of balance correction, VIP-VPAC signaling is unlikely to mediate the acute FMN^{VIP} to MVN transmission, but again it may instead contribute to slower adjustments of MVN excitability over longer timescales. Future experiments employing selective receptor antagonists, such as PG97-269 and PG99-465 (VPAC1 and VPAC2 antagonists, respectively), with *in vivo* photometry recordings at MVN will be essential to dissect how individual receptors may contribute to the observed FMN^{VIP} modulation in MVN during postural control.

Moreover, the specific inhibitory neuronal subtypes in MVN that are targeted by FMN^{VIP} neurons remain unidentified. The MVN contains a rich diversity of inhibitory neurons, such as PV- and SST-expressing inhibitory neurons, and broadly vGAT-expressing cells that coordinate bilateral vestibular tone and regulate reflex gain (217,218). PV neurons in MVN, in particular, contribute to balance recovery after unilateral vestibular lesions, where restoring their bilateral activity accelerates compensation (70). They are also thought to provide local and commissural control rather than descending spinal output, which distinguishes them from the spinal-projecting MVN neurons that are predominantly excitatory (210). This is consistent with our tracing

experiments, which revealed the absence of TRACR-labeled MVN GABAergic axonal innervation in the cervical spinal cord (Fig. 4J-K). Future experiments combining the FMN^{VIP}-MVN TRACR with RNAscope for PV and SST mRNA could determine which inhibitory subclasses receive the FMN^{VIP} input. In contrast, we observed MVN descending axons in the cervical spinal levels when we labeled all neurons in MVN (Fig. 4H), consistent with the classical studies that showed VCR and VSR reflex pathways are mediated by the excitatory neurons in MVN (10,185,210). In rodent MVN, excitatory neurons are broadly divided into vestibular-only (VO) and eye-movement-sensitive (ES) subtypes, distinguished by their sensory integration and output targets (217,218). Whereas ES neurons primarily contribute to ocular premotor circuits such as the OKR, VO neurons integrate vestibular inputs and drive vestibulospinal pathways that encode head orientation and body motion through the vestibulocollic and vestibulospinal reflexes (VCR/VSR) (39,40,185,210). The observed GFP-labeled descending MVN fibers in the cervical spinal cord likely arise from VO neurons. Therefore, we predict that FMN^{VIP} neurons target the GABAergic neurons in MVN to modulate the activity of VO glutamatergic neurons, which in turn project to the spinal cord. The intact OKR following FMN^{VIP} ablation (Fig 1.H) suggests that the FMN^{VIP} pathway is unlikely involved in modulating the gaze-stabilizing ES neurons in MVN.

Lastly, our tracing clearly demonstrates that MVN is a principal target of FMN^{VIP} neurons; however, it does not preclude that FMN^{VIP} neurons also project to additional long-range targets beyond the vestibular nucleus. Broader projection-mapping remains an important next step. The anterograde tools available to date have been the limiting factor in addressing this question. For example, AAV1-Cre enables virus-mediated trans-synaptic tracing of axonal outputs but cannot restrict labeling to a specific cell type at the input site. Newer anterograde systems also show relatively low and variable labeling efficiency, further constraining their use for broad FMN^{VIP}-specific output mapping (219–224). Future work using newly

developed anterograde viral tracing tools or single-cell reconstruction will be required to enumerate the complete downstream targets of FMN^{VIP} neurons and correlate them with distinct behavioral outputs. Overall, in our proposed model, FMN^{VIP} neurons excite the GABAergic neurons in MVN via ACh release acting on α7-type nicotinic receptors. This, in turn, inhibits the spinal-projecting excitatory VO neurons in MVN. The FMN^{VIP}-mediated cholinergic input can provide rapid, state-dependent modulation of MVN response gain based on reticulovestibular feedback, and this mechanism helps adjust vestibulospinal output (VCR/VSR) on a moment-to-moment basis to stabilize balance during perturbations. This layered modulation complements the MVN's multimodal organization for postural maintenance.

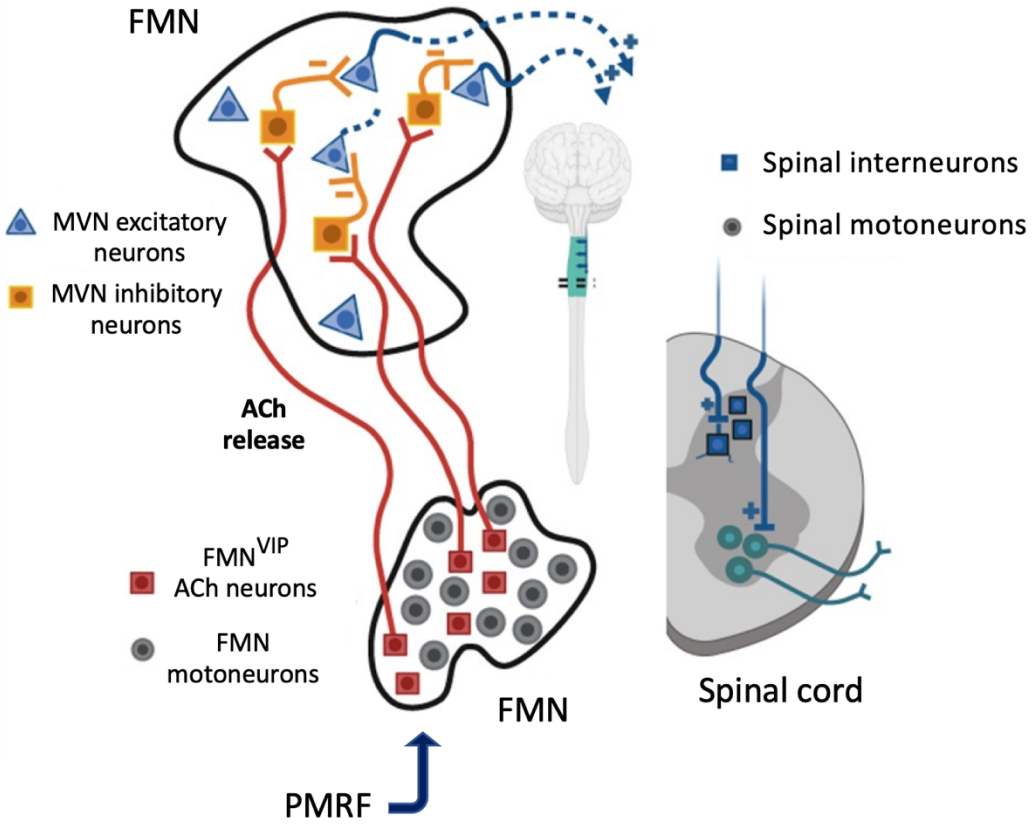

Figure III. Proposed working model of FMN^{VIP}-mediated cholinergic modulation of vestibulospinal control. VIP-expressing cholinergic neurons in the facial motor nucleus (FMN^{VIP}) release acetylcholine (ACh) onto inhibitory interneurons within the medial vestibular nucleus (MVN). The cholinergic input modulates MVN output by shaping the balance between inhibitory and excitatory vestibular neurons, thereby regulating downstream vestibulospinal drive. Through this pathway, FMN^{VIP} neurons influence spinal circuits to adjust cervical and postural reflexes during balance-challenging conditions, integrating reticular formation inputs (PMRF) with vestibular control of posture.

CHAPTER 4: METHODS

1. Animals

All procedures were approved by the University of Ottawa Animal Care Committee and followed Canadian Council on Animal Care (CCAC) guidelines. Mice were housed in groups in standard plastic cages with food and water ad libitum. Housing rooms were temperature- and humidity-controlled and operated on a reversed 12:12-hr light-dark cycle. The following transgenic lines were used: PV-Cre (JAX 008069), SST-Cre (JAX 013044), VIP-Cre (JAX 010908), Ai14 tdTomato (JAX 007914), and the B6129SF1/J background strain (JAX 101043). We also used Gad1-EGFP transgenic mice (Tg(Gad1-EGFP)94Agmo/J; JAX 006334). VIP-, PV-, and SST-Cre::Ai14 colonies were generated by crossing VIP-, PV-, or SST-Cre females with Ai14 males. Cre-driver and reporter lines were used in separate anatomical and circuit-mapping experiments. Adult male and female mice were used for all behavior, photometry, and anatomical studies. Animals were randomly assigned to experimental groups. Animals that showed signs of distress or failed to meet predefined humane endpoint criteria were removed from the study.

2. Viral vectors

All viral vectors were stored at -80 °C and kept on ice during surgery. Ablation experiments included AAV1-FLEX-taCasp3-TEVp (Addgene; cat. no. 45580-AAV1; $\geq 7\times10^{12}$ GC/mL) with or without AAV1-CMV-PI-Cre-rBG (Addgene; cat. no. 105537-AAV1; $\geq 1\times10^{13}$ GC/mL) for MVN-ablation and FMN^{VIP} ablation, respectively. Sham was injected with AAV1-CAG-FLEX-EGFP-WPRE (Addgene; cat. no. 51502-AAV1; $\geq 1\times10^{13}$ GC/mL) and AAV1-CMV-PI-Cre-rBG (Addgene; cat. no. 105537-AAV1; $\geq 1\times10^{13}$ GC/mL). For chemogenetic experiments, AAV2/9-hSyn-DIO-hM4D (Gi)-mCherry (Université Laval; cat. no. AAV796;

1.8×10^{13} GC/mL) was used. For fiber photometry calcium imaging, AAV1-Syn-Flex-GCaMP8m-WPRE (Addgene; cat. no. 162378-AAV1; 1.7×10^{13} GC/mL), and acetylcholine sensor imaging pAAV-hSyn-GRAB-ACh3.0.AAV09 (Addgene; cat. no. v216530; 1.6×10^{13} GC/mL) were used. For the TRACR experiments, Sender virus AAV1-hSyn-Flex-Nrx3b-eGFP-T2A-ChR2 (H132R)-YFP-WPRE-bGH (1.3×10^{13} GC/mL) was injected in the input region FMN. The receiver virus AAV1-hSyn-LaG17-SynNotch-FetR (1.3×10^{13} GC/mL) and the reporter virus AAV2/9-dp-99-pAAV-TRE-mRuby2 (1.7×10^{12} GC/mL) were together injected into MVN. The receiver and reporter viruses were mixed at a 1:1 ratio immediately before injections. All three TRACR components were generated by the laboratory of Dr. Julie Lefebvre (The Hospital for Sick Children, Toronto). For the retrograde monosynaptic rabies tracing, EnvA-RVΔG-mCherry (Charité ACF Viral Core; cat. no. RV03/PN-2127; 4.24 X 10^7 GC/mL) and AAV-hSyn-FLEX-TVA-P2A-eGFP-2A-oG (Université Laval Viral Core; cat. no. AAV1137; 1.3×10^{13} GC/mL) were used.

3. Stereotaxic surgeries

All procedures were performed under aseptic conditions. Mice were anesthetized with isoflurane (4-5% induction and 1-2.5% maintenance in 100% O_2). The anesthetized mice were placed in a stereotaxic frame with the skull leveled between bregma and lambda. Body temperature was maintained on a servo-controlled heating pad, and ophthalmic ointment was applied to prevent corneal drying. The skin was cleaned with 70% ethanol and disinfected with betadine, and EMLA cream (lidocaine/prilocaine) was applied pre-incision for additional local analgesia. A midline incision exposed the skull, which was cleaned before drilling small craniotomies above the target sites. Viral injections were delivered using a 1 µL Hamilton Microliter™ #701 syringe mounted on an infusion pump. Infusions were made at 30 nL/min. The needle was lowered slowly to reduce tissue displacement, rested for 5 min before infusion, and remained for 10 min afterward to allow diffusion. When multiple depths were required, the deepest site was injected first. The needle was withdrawn slowly to minimize backflow. For FMN-targeted procedures, the injector was positioned at anteroposterior

(AP) -5.8 mm, mediolateral (ML) 1.2 mm, and dorsoventral (DV) -5.9 and -5.7 mm relative to bregma. VIP-Cre mice received bilateral FMN injections (250 nL per depth; max total 500 nL) of rAAV-FLEX-taCasp3-TEVp for ablation, AAV-Flex-eGFP for sham controls, AAV1-Syn-Flex-GCaMP8m-WPRE for Ca^{2+} photometry, AAV2/9-hSyn-DIO-hM4D(Gi)-mCherry for chemogenetic inhibition, or the TRACR Sender AAV1-hSyn-Flex-Nrx3b-eGFP-T2A-ChR2(H132R)-YFP-WPRE-bGH. For MVN-targeted procedures, the injector was positioned at AP -5.7 mm, ML 0.7 mm, DV -4.3 and -3.7 mm. Wild-type mice received unilateral MVN injections of AAV9-hSyn-GRAB-ACh3.0 for ACh photometry (250 nL per depth; max total 500 nL). AAV-hSyn-LaG17-SynNotch-FetR and AAV-TRE-mRuby2 (1:1) were injected for TRACR experiments. For ablation, AAV1-CMV-PI-Cre-rBG was mixed 1:1 with rAAV/FLEX-taCasp3-TEVp, and for sham controls or MVN-spinal projection labeling it was mixed 1:1 with AAV1-CAG-Flex-eGFP-WPRE-bGH. Monosynaptic rabies tracing was performed by unilaterally injecting EnvA-RVΔG-mCherry into FMN of mice that had received the AAV-hSyn-FLEX-TVA-P2A-eGFP-2A-oG three weeks earlier. Mice were perfused 7 days after the rabies delivery. For Ca^{2+} photometry experiments, an optic fiber cannula (400 µm core, NA 0.48) mounted on a 3D-printed plastic microdrive was implanted 200 µm above the injection site and secured with Metabond Quick. The microdrive allowed post-surgical dorsoventral adjustments. For ACh photometry, an optic fiber was implanted 200 µm above MVN injection site. At closure, dexamethasone (2 mg/kg subcutaneously (SC)) was administered to reduce edema. Buprenorphine (0.1 mg/kg SC) was administered at induction and again 4-6 hrs later, with additional doses on Day 1 as needed. Baytril (5 mg/kg SC) was given at induction and once daily for the following two days. Animals recovered in a warmed cage and received 1 mL warm saline SC. They were monitored twice on the day of surgery and daily thereafter according to ACVS requirements. Mice were allowed at least three weeks for viral expression before behavioral testing, photometry, or histology, except for rabies experiments requiring a shorter survival time.

4. Histology and post-hoc analyses

4.1. Perfusion and sectioning

Mice were deeply anesthetized and transcardially perfused with 4% paraformaldehyde (PFA) in phosphate-buffered saline (PBS). Brains were post-fixed overnight in 4% PFA at 4 °C and then transferred to 30% sucrose in PBS containing 0.1% sodium azide at 4 °C until they sank (~48-72 h). Brains were then sectioned on a freezing sliding microtome (Leica SM2000R), and 40 µm coronal sections were collected free-floating in PBS with 0.1% sodium azide and stored at 4 °C. For RNAscope, cervical spinal cord or brain tissue blocks were embedded in OCT compound, and 16 µm transverse cryosections were cut on an HM525NX cryostat and collected free-floating in 24-well plates to keep AP slice order.

4.2. Immunostaining

For immunohistochemistry, free-floating sections were washed in 1x phosphate-buffered saline (PBS) and then in PBT (0.1% Triton X-100 in PBS). Sections were incubated in blocking solution in PBT containing 5% normal donkey serum, 1% bovine serum albumin (BSA), and 0.5% gelatin with gentle agitation at 4 °C. Incubations were performed in 12-well plates (2 mL per well). Primary antibodies were diluted 1:500 in fresh blocking solution. The following primaries were used: chicken anti-GFP (Aves Labs, GFP-1020), goat anti-ChAT (Millipore AB144), rabbit anti-GABA (Sigma A2052), guinea pig anti-NeuN (Synaptic Systems 266004), and rabbit anti-DsRed (Takara 632496). All virally expressed fluorophores, including GCaMP, ACh sensors, and TRACR reporter, were amplified using the appropriate anti-GFP or anti-DsRed primary antibodies. Sections were incubated in primary antibody for 48 h at 4 °C on a shaker. After washing in PBS and then PBT, sections were incubated with secondary antibodies diluted 1:500 in blocking solution at 4 °C in the dark. Secondary antibodies used were donkey anti-chicken IgY-Alexa Fluor Plus 488 (Jackson ImmunoResearch 703-546-155), donkey anti-goat IgG-Alexa Fluor 647 (Invitrogen A21447), donkey anti-

rabbit IgG-Alexa Fluor 647 (Thermo Fisher Scientific A-31573), and donkey anti-rabbit IgG-Alexa Fluor 594 (Invitrogen A-21206). Following secondary incubation, sections were washed in PBS, mounted onto Superfrost Plus slides in PBS, air-dried briefly, and coverslipped with Vectashield HardSet with DAPI (cat. no. H-1800-10). Slides were allowed to sit at room temperature for ~1 h and stored at 4 °C until imaging.

4.3. RNAscope assay

Fluorescent *in situ* hybridization was performed on fixed-frozen brain sections using the RNAscope® Multiplex Fluorescent Reagent Kit v2 (Advanced Cell Diagnostics; cat. 323100) following the manufacturer's instructions for fixed-frozen tissue (user manual UM-323100) with minor adjustments. Mice were perfused with 4% paraformaldehyde (PFA), and tissue was post-fixed for 6-12 h at 4 °C. Samples were cryoprotected for 72 h in 70% sucrose, embedded in OCT, and sectioned at 16 µm on a cryostat at -20 °C onto Superfrost Plus charged slides. On the day of the assay, slides were equilibrated to room temperature, post-fixed briefly in 4% PFA, dehydrated in graded ethanol, and pretreated with RNAscope Hydrogen Peroxide (cat. 322335), Target Retrieval reagent (cat. 322000), and Protease Plus (cat. 322331) in a HybEZ™ oven at 40 °C. Targeted RNAs were detected with RNAscope probes assigned to channels C1-C3 and hybridized for 2 h at 40 °C. Standard AMP1, AMP2, and AMP3 amplification steps were followed by HRP-C1, HRP-C2, and HRP-C3 incubations using the Multiplex Fluorescent Detection Kit v2 (cat. 323110). Signals were visualized with TSA Vivid dyes 520 and 650 (ACD Bio; cats. 323271 and 323273) diluted 1:750 in RNAscope Multiplex TSA Buffer (cat. 322810). Slides were counterstained with Vectashield HardSet with DAPI (Cat. no. H-1800-10) and coverslipped. Negative and positive controls were processed in parallel using the 3-plex DapB negative control probe (cat. 320871) and the 3-plex mouse positive control probe Polr2a/Ppib/Ubc (cat. 320881). The following mouse target probes (ACD Bio) were used: Mm-Vip (415961, C1), Mm-Slc17a7 (481851, C1), Mm-Gad1 (400951, C2), and Mm-Slc32a1 (319191, C3).

5. Imaging

Fluorescence sections were imaged on a Zeiss AxioImager M2 upright fluorescence microscope with motorized stage control. For whole-section overview imaging, tiled acquisitions were performed across the entire brain or spinal cord section, and mosaics were reconstructed using ZEN (Zeiss) software. Higher-magnification fields (e.g., starter cells, local circuit regions, cervical spinal cord) were acquired using a 20× objective. Laser illumination, detector gain, exposure time, and offset were held constant across all samples within each experiment. Images were exported as TIFF files and processed in Fiji/ImageJ. Only linear brightness and contrast adjustments (applied uniformly across the dataset) were permitted.

5.1. Cell counting

5.1.1. Whole-brain rabies cell mapping

Rabies-labeled cells were quantified using an atlas-registered workflow that combined ImageJ preprocessing, QUINT-based atlas alignment, ilastik segmentation, and Nutil regional assignment (180,225,226). Coronal images were preprocessed in Fiji/ImageJ and aligned to the Allen Mouse Brain Atlas (CCFv3) using QuickNII, with final refinements performed in VisuAlign (227) and with atlas maps adapted to match section orientations. Cell segmentation was carried out in ilastik (Pixel Classification) using a Random Forest classifier trained to detect rabies-positive cells based on intensity and texture features (181). The classifier was validated on representative slices and then applied in batch mode to all sections. Binary segmentation masks were exported and loaded into Nutil Quantifier together with the VisuAlign-refined atlas maps, the QuickNII metadata, and the Allen reference atlas (225). Using object-count mode, Nutil assigned each segmented soma to its atlas-defined region and produced per-slice cell-count tables. Region-level outputs from Nutil were subsequently processed in Python. Non-neuronal structures (ventricles, aqueducts, corpus callosum, major white-matter

tracts, and other non-grey-matter structures) were removed, and parent structures were excluded to retain only subregions. For each slice, we obtained region-level cell counts (number of rabies-labeled cells per region per slice), and these slice-wise counts were summed to produce one value per region per animal. Regions were then classified as forebrain (rostral) or hindbrain (caudal) using a fixed AP boundary of -4.5 mm from bregma (anterior = rostral to -4.5 mm; caudal = at or posterior to -4.5 mm). For each animal, anterior and caudal totals were computed by summing region-level counts within each category and dividing by the animal's whole-brain rabies count to yield fractional anterior and fractional caudal input distributions.

5.1.2. Neuronal and axonal detection

Fluorescent cell density and co-labeling were quantified in QuPath. Multichannel TIFF sections were imported into a QuPath (v0.4) project, and regions of interest (ROIs) were manually drawn over defined nuclei or spinal gray-matter ventral horn compartments. DAPI was used to confirm the presence of a nucleus within each ROI. Positivity and co-localization were defined using the fluorophore channels of interest. Within each ROI, QuPath's cell-detection tools were used to identify cells. Intensity thresholds for marker positivity were derived from background regions in the same sections where the marker is not expected to be expressed. For each experiment, ROIs were marked in marker-negative tissue, the fluorescence intensity distribution was measured, and the positivity threshold was defined as mean background intensity plus three standard deviations. This threshold was then applied uniformly to all ROIs and animals within that experiment, in line with established QuPath workflows for immunofluorescence quantification in rodent brain tissue. For cell density, QuPath reported the number of marker-positive cells per ROI area (cells/mm^2). For co-labeling analyses, QuPath exported cell-level co-labeling for each ROI. These data were analyzed on MATLAB or Python to compute the fraction of VIP-tdTomato cells that were positive for each immunostained marker within a given ROI. For spinal cord axon density measurements, atlas-matched ROIs were drawn bilaterally

around ChAT-positive motoneurons at cervical levels (C1-C7), and the same workflow was applied to all projection groups (MVN-GFP, FMN^{VIP}-GFP, and TRACR-reporter). In QuPath, each ChAT-positive cell was segmented, and a 10 μm cytoplasmic ring was generated, within which mean fluorescence intensity was extracted from the relevant axonal channel. For each group, intensities were then normalized to background fluorescence measured in axon-free regions of representative sections from the same imaging session. These background-normalized axonal intensities were pooled across multiple sections and animals and used for statistical analysis of spinal projection strength.

5.2. Image analysis:

To map the AP distribution of VIP cells in FMN, fixed brainstem sections from VIP-Cre::Ai14 mice were imaged across the full FMN span (-5.55 to -6.18 mm from bregma). For each animal, seven AP levels (subregions) were selected according to the Allen Mouse Brain Atlas (Mouse Coronal, v1 2008). ROI areas were derived from the atlas-matched FMN contour and used to convert raw counts into cell density (cells/mm^2). For each AP level, density values were averaged across animals. For PV- and SST-expressing cell density, FMN cell density was quantified from PV-Cre::Ai14 and SST-Cre::Ai14 mice, processed in parallel with VIP-Cre::Ai14 tissue. DAPI-guided nucleus detection was applied, and tdTomato fluorescence was used to classify PV- or SST-positive cells according to genotype. When more than one section sampled a given level in an animal, counts were averaged to yield a single density value for that level, expressed as cells/mm^2, using the same ROI areas defined for the VIP analysis.

FMN^{VIP} ablation was quantified by measuring the loss of tdTomato-positive VIP cells across predefined FMN subregions using QuPath. For each mouse, all sections corresponding to a given subregion were pooled bilaterally, and their counts were averaged to yield a single tdTomato value per FMN subregion. Sham animals provided the anatomical reference. For each subregion, the sham averages were computed across all sham mice and used as the normalization baseline. In FMN-taCasp animals, subregion wise tdTomato counts were

divided by their respective sham reference means to obtain the fraction of surviving VIP cells. Sham mice were normalized in the same way (each data point relative to the sham group mean). To summarize the ablation efficiency per animal, the highest subregion ablation rate was taken as that animal's fraction of ablation. Immunostaining co-localization analysis was performed within FMN regions using QuPath software by evaluating whether, for every VIP-positive cell, the nucleus and surrounding cytoplasmic signal overlapped with the marker channel of interest (GABA, vGlut1, or ChAT). Reverse co-labeling (ChAT cells co-localized with VIP) used the same procedure but treated ChAT-positive cells as the reference population. For each slice assigned to an anatomically defined FMN level, we computed the proportion of reference cells showing probe overlap, yielding a bilateral co-localization ratio per slice. All detection thresholds, puncta-classification settings, and ROI definitions were held constant across slices and animals. Analyses were conducted with the experimenter blind to probe identity and expected direction of co-labeling.

5.2.1. TRACR Image analysis

TRACR-labeled cells in MVN were quantified in QuPath. For each slice, MVN regions of interest (ROIs) were drawn to match the Allen Mouse Brain Atlas (AMBA) MVN boundaries and then reused across sections at the same AP level, so that QuPath's automated cell-detection and classification were applied within standardized atlas-matched ROIs. Reporter-positive cells (mRuby-positive) were detected with the QuPath cell-detection module using a uniform intensity threshold defined from non-target regions (not targeted by receiver and reporter) to avoid false positives. Within each animal, reporter counts were averaged across slices belonging to the same MVN region. These region means were then summed across all sampled regions to yield a single TRACR labeling index per animal. Image analysis for TRACR-GABA co-localization was carried out in QuPath using atlas-matched MVN ROIs. Within each MVN ROI, cell bodies expressing the TRACR reporter (mRuby-positive) were detected using QuPath's cell-detection module. GABAergic cells

were identified using anti-GABA immunostaining. Co-localization was determined at the single-cell level by assessing whether each TRACR-labeled soma overlapped with the GABA signal within its cytoplasmic boundary. For each slice, the co-localization ratio was computed as the number of co-localized cells divided by the total TRACR-labeled cells in that slice. Because slice availability differed across MVN AP levels, a balanced sampling strategy was applied to avoid overweighting regions represented by more slices. All valid slices were first grouped by anatomical level based on the atlas. From each of the three subregions, representing MVN, three valid slice-level ratios were randomly selected without replacement across all animals, generating a balanced dataset. These ratios were used to compute the group mean and SEM for TRACR-GABA co-localization in the reporter cohort. All analyses were performed blind to animal identity and anatomical level. For shuffled analysis each labeled cell was therefore classified as 1 (co-localized) or 0 (not co-localized), generating a binary co-localization vector per MVN region. All valid slices per animal were pooled to yield one binary dataset for the reporter group and one for the control group. These pooled binary datasets formed the input for the shuffling-based statistical test. For the shuffled-co-localization procedure, 30 binary values were randomly drawn with replacement from each group per iteration, and a co-localization ratio (fraction of 1's) was computed. This procedure was repeated 1,000 times for both groups to generate two empirical distributions of shuffled co-localization ratios. The empirical one-sided p-value was defined as the proportion of iterations where the control ratio was greater than or equal to the reporter ratio, testing the hypothesis that TRACR-labeled inputs have higher GABA co-localization in the reporter group. For TRACR-labeled projections, axonal intensity in the cervical spinal cord was quantified by measuring mean mRuby fluorescence intensity within 10 μm cytoplasmic rings around ChAT-positive motoneurons in QuPath as described above.

5.3. RNAscope probe quantification

RNAscope fluorescent *in situ* hybridization was quantified in QuPath using a standardized, probe-specific workflow that captured puncta counts at region-level densities. The subcellular-detection module was used to detect individual RNAscope puncta within each segmented cell. Thresholds for puncta detection were set separately for each probe using negative-control sections to ensure true probe specificity. Cells were classified as probe-positive when their puncta count exceeded the threshold for that probe. For each anatomically defined FMN region of interest (ROI), QuPath exported the number of probe-positive cells and the ROI area (μm^2). Cell density was computed as probe-positive cells per mm^2. If multiple slices sampled the same region within an animal or hemisphere, the values were averaged to yield a single density estimate for that anatomical level. The density values were then collapsed to a single mean per region per probe for plotting. After region-level values were obtained, each available anatomical region contributed one data point for each probe.

6. Behavior

6.1. Optokinetic reflex (OKR) assay

OKR behavior was measured in head-fixed mice positioned at the center of a three-monitor visual stimulus arena. Vertical sinusoidal gratings (spatial frequency 0.16 cycles/degree; luminance 45 cd/m^2; contrast 1.0) were drifted horizontally from right to left (temporonasal direction for the right eye). Each stimulus lasted 8 s and was separated by a 5 s inter-trial interval. Seven temporal frequencies were presented, and each was repeated 25 times per session. OKR testing was performed in mice aged 2-3 months. Eye movements were recorded using infrared video-oculography and processed offline after removing fast-phase nystagmus components. The OKR gain, which quantifies the accuracy of visual tracking, was calculated as the ratio of the amplitude of the eye movement to the amplitude of drum motion (Gain = Amp-eye / Amp-drum). A gain

of 1 indicates perfect tracking (the eye moves by the same amplitude as the grating); a gain of 0 indicates no tracking, and negative values indicate that the eye moves in the opposite direction of stimulus motion.

6.2. Vertical pole test (VPT)

Balance performance was assessed using a vertical pole test adapted from standard protocols with a rough-surfaced pole (161). Mice were tested at the University of Ottawa Animal Behavior and Physiology Core in the testing room under dim red-light illumination. The pole consisted of a vertical beam (20 mm diameter, 95 cm height) wrapped in rough sandpaper-backed paper to provide a non-slippery surface. On the test day, mice were brought to the room in their home cage and allowed to habituate for 10 min at the base of the apparatus. Each animal then underwent a single session of ten trials, with 1 min inter-trial interval during which the mouse was resting in its home cage. At the start of each trial, the mouse was placed head-up at the top of the pole and allowed to orient itself, rotate, and descend. Behavior was recorded with an ELP 2.0-megapixel USB camera (model ELP-USBFHD01M-BL28IR), and analysis was performed offline by a blinded experimenter. To minimize novelty effects, the first three trials were treated as habituation and excluded from quantification. For each trial, we counted the number of torsional movements during descent by scoring both full 360° axial spiral movement ("full turns") and 180° rotations ("half turns"), with half turns contributing 0.5 to the spiral count. For each mouse, the mean spiral count across analyzed trials was computed and normalized to the mean spiral count of sham-treated animals to yield a spiral motion intensity index (SMI = individual trial spiral count / overall mean sham spirals). For quantitative comparisons, all trial counts from sham (or saline) animals were pooled to compute the reference spiral mean. Each individual trial was then normalized by dividing its spiral count by this reference mean to yield a spiral motion intensity**.**

6.3. Open field locomotion

Baseline locomotion and gait were assessed in a square open-field arena (45 × 45 × 45 cm) in the University of Ottawa Animal Behavior and Physiology Core, using custom-built opaque acrylic arenas and EthoVision XT tracking software (Canus Plastics; Noldus Information Technology). On the test day, mice were brought to the behavioral room in their home cage and allowed to habituate for at least 30 min before testing. Each mouse was then placed in the center of the arena and allowed to explore freely for 10 min under infrared light. Behavior was recorded with an overhead camera, and x-y position was extracted frame-by-frame with EthoVision XT, which is commonly used for open-field animal movement-velocity measurement protocols. From these trajectories, we calculated mean locomotor velocity. Baseline gait was defined as the mean locomotor velocity across the 10-min session, providing a simple index of spontaneous locomotor performance that is comparable to other open-field locomotor assays (228–230)

6.4. Accelerating rotarod

Motor coordination and balance were evaluated on an accelerating rotarod in the University of Ottawa Animal Behavior and Physiology Core, using mouse rotarod systems from IITC Life Sciences or Ugo Basile. On the test day, each mouse received one habituation trial at constant speed (4 rpm, 60 s) to familiarize it with the apparatus, similar to standard conditioning procedures. For the main test, the rod was set to accelerate linearly from 4 to 45 rpm over 5 min, an accelerating paradigm closely matching those used to assess neuromuscular coordination in mice. Each mouse underwent 3 days of testing with four accelerating trials separated by 30-45 min inter-trial intervals. For each animal, the latency to fall of the last trial of the last day was used for quantitative assessment (231,232).

6.5. Forelimb grip strength test

Forelimb muscle strength was measured using a digital force transducer (Chatillon DFE series, Columbus Instruments/AMETEK), which relies on a horizontal bar attached to a Chatillon force gauge. Mice were acclimatized to the testing room for at least 30 min before the assay. For each trial, the mouse was held by the base of the tail and allowed to grasp a horizontal metal grid bar with its forepaws only, in line with commonly used forelimb-only configurations. Once the animal established a firm, symmetric grip, the experimenter gently pulled the mouse straight back in a horizontal plane until the grip was released, and the device recorded the peak force in gram of force. Each mouse performed 7 consecutive trials separated by 30 s. The trials in which the mouse failed to grasp the bar properly were discarded and repeated. For analysis, the mean peak force across the trials was calculated for each animal (233,234).

6.6. Horizontal beam test (HBT)

Balance during traversal on a narrow surface was evaluated with a Horizontal Beam Test (HBT) adapted from Dr. Tom Jessel's laboratory (41). The apparatus consisted of a 5-mm-wide, 40-cm-long metal beam mounted 20 cm above the base inside a closed behavioral box. The distal end faced the animal's home cage, positioned across a 2 cm gap. The box was illuminated with red infrared (IR) light to suppress visual cues. Mice were single housed for at least 72 hrs before testing. Before each HBT session, the animal's home cage was placed on the raised platform inside the HBT box, and mice were allowed to habituate to this configuration for 30 min under IR lighting. For each trial, mice were placed on the start platform at one end of the beam and allowed at least 10 s to orient its head forward before initiating the traverse. Animals walked freely toward their home cage without any additional appetitive or aversive stimuli. An ELP 2.0-megapixel USB camera (model ELP-USBFHD01M-BL28IR) mounted 40 cm above the beam, recorded the entire traverse for later scoring, and videos were used for DeepLabCut® (DLC) analysis. Each animal completed 5 trials in a single session for traversal experiments, or 15 trials (consisting of left-, right-, or no-perturbation trials) for the perturbation

combined with fiber photometry experiments. Animals were allowed 1-min rest periods atop the home cage between trials. Three extra trials were performed at the beginning of each session and treated as habituation and excluded from analysis. Trials were excluded if the mouse (1) refused to walk, (2) paused and remained stationary for more than 5 s during the traverse, (3) paused and turned more than 90° toward the start direction, or (4) flipped its body and attempted to walk inverted along the beam. A fall was defined as any loss of balance where the abdomen dropped below the top edge of the beam, regardless of whether the mouse fully left the beam or briefly recovered. Chemogenetic HBT experiments used the same apparatus, trial structure, habituation procedures, and exclusion criteria. Each mouse performed two traversal sessions on separate days, one 40 min after saline intraperitoneal (IP) injection and one 40 min after JHU37160 (JHU) delivery.

For the fiber photometry HBT experiments, 3 weeks after the surgery animals were connected to a photometry patch cord and placed on the start platform at the beginning of each trial, then allowed to sit for 30 s before traversing the beam. Calcium or ACh signals were acquired through the photometry system while the overhead ELP 2.0-megapixel USB camera (model ELP-USBFHD01M-BL28IR), mounted 40 cm above the beam, recorded the full traverse for DLC analysis. For perturbation trials during fiber-photometry HBT sessions, the same beam and recording setup were used. In this context the already mounted beam was actuated for movement by a motorized axis driven by a TowerPro SG-5010 servo motor (Adafruit cat. no. 155) and controlled by an Arduino Uno R3 interfaced with MATLAB, allowing precise yaw-axis transitions. Perturbations were triggered remotely by the experimenter when monitoring the live behavioral video stream. The experimenter initiated the perturbation when the animal reached a marked location in the distal portion of the beam (last one-third of the beam). A custom MATLAB script sent a digital output pulse from the Arduino, which rotated the servo to produce a brief lateral displacement. Perturbations consisted of short leftward or rightward beam displacement (0.8 cm at 95 cm/s). Each session included 5 left-, 5 right-, and 5 five no-

perturbation trials. The pattern of the trials was generated randomly, and was kept fixed across animals on that day, ensuring consistency while remaining unpredictable to the mouse during the session.

Traversal success was defined as a trial that the animal completed the entire beam without falling or slipping off the surface. Trials meeting the traversal exclusion conditions (mentioned above) were consider as unsuccessful. For each animal, the success rate was computed as the proportion of successful trials out of the five scored traversal trials.

6.7. In-cage locomotion

In-cage activity was recorded in a standard mouse home cage (30 × 19 × 13 cm, filled with bedding, same dimensions as the animal's regular housing cage). For imaging, the floor of a clean cage was covered with a sheet of black plastic to increase contrast between the animal and the background. The cage was placed in a dark enclosure illuminated only with infrared (IR) light, and behavior was recorded using an overhead camera ELP 2.0-megapixel USB camera, model ELP-USBFHD01M-BL28IR). Before the start of the recording, mice were connected to the fiber photometry patch cord and allowed to habituate in the home cage for 30 min under IR illumination. During the acquisition, animals were allowed to move freely, and calcium or ACh signals were acquired continuously in parallel with the behavior video recording. For subsequent analysis, we manually labeled the four cage corners in each video to define the in-cage boundaries and tracked the animal's head as the position marker for its location within the box. These coordinates were used to define in-cage territories and locomotor epochs and to train DLC for batch video labeling.

7. DeepLabCut (DLC) pose estimation

All behavioral videos were processed with DeepLabCut® using the standard single-animal workflow. Independent landmarks were labeled for these assays (235). Independent landmarks were labeled for these assays that captured whole-body orientation and movement during beam traversal and in-cage locomotion. Representative frames were extracted uniformly from all animals and recording sessions (~20-45 frames per

video; total ~1485 frames) and annotated manually for the DLC training. Selected frames covered the full range of behavior. A ResNet-50 network was trained using default DLC hyperparameters. DLC automatically generated training and test sets (95% training, 5% test). Network performance was evaluated using the training loss and the pixel error on the held-out test set. Additional outlier frames were extracted and relabeled when necessary, and training was repeated until test error stabilized at its minimum (<0.95 pixels). Final pose extraction was performed using the analyze-videos function. Frames with landmark likelihood below 0.90 were flagged and excluded from analysis. The final coordinate data (x, y, likelihood) for all landmarks were exported at ~30 Hz. For HBT traversal analysis, DLC coordinates for each frame was extracted, which included the coordinates for the start of the beam (SB), end of the beam (EB), sacrum (S), and head (H). Using these points, we computed the angle subtended by SB-H-S for the body orientation of the animal on HBT in each frame. The angle was then calculated using an atan2-based three-point formula and converted the result to degrees; this yields an absolute (0-180°) measure of postural deviation from the beam axis. Frames were removed when any landmark likelihood fell below the DLC threshold. Within each trial, outlier rejection was applied using the median-absolute-deviation (MAD) method with a threshold of 3.5 times the MAD on the pooled frame angles. To calculate posture-angle variance of the animal's traversal movement for an individual trial, the variance (calculated as the relative variance) was divided by the mean of the angles (per trial). To compare chemogenetic manipulation effects on beam traversal, we applied the same analysis pipeline as for the taCasp-Sham comparison, except that trials were grouped by treatment day (saline Day 1 vs. JHU Day 2). For HBT perturbation trials, perturbation onset was marked by a TTL pulse generated by the Arduino when the motor initiated the beam transition. Latency to postural recovery was then quantified from the DLC-derived body angle, computed frame by frame as the internal angle between SB-H-S. The pre-perturbation angle in the pre-perturbation frame was taken as the reference posture. Post-perturbation angles were tracked until they reached their maximal deviation and then began a sustained return toward this baseline. The first frame

showing this sustained return was defined as recovery initiation. Latency to postural recovery was calculated as the frame difference between perturbation onset and recovery initiation. During in-cage epochs, mouse position was tracked using the head marker. We used four points to mark the cage corners and to calculate the spatial limits of the cage. On each frame, we extracted the head position and classified the mouse as inside the cage (in-cage) when the head lay within these bounds. This binary inside/outside label was then scanned over time to segment the recording into continuous in-cage epochs. When the head left the cage, we allowed up to 15 consecutive outside frames (buffer) before terminating a epoch, preventing brief tracking noise or posture-related misdetections from fragmenting epochs. After segmentation, we retained only in-cage epochs whose duration exceeded 300 frames (~10 s), ensuring that each epoch provided a stable window of in-cage behavior. These epoch indices were subsequently used to extract time-matched random segments from the aligned photometry signal.

8. Fiber photometry setup (FPS)

Fiber photometry recordings were performed with a single-channel Fiber Photometry Console (Doric FPC) coupled to a four-port Fluorescence MiniCube (ilFMC4-G2_IE (400-410)_E (460-490)_F (500-550)_S). Excitation at 405 nm (isosbestic) and 460 nm (Ca^{2+}/ACh-sensitive) was delivered through low-autofluorescence 200-µm, NA 0.57 patch cords (MFP series), routed through a 1×1 rotary joint (FRJ_1x1_PT_200/230/LWMJ-0.57) mounted on a gimbal, and coupled to implanted 200-µm, NA 0.57 optical cannulas (5-6 mm, MF1.25 ferrule). Patch cords were joined using 1.25-mm zirconia sleeves (SLEEVE_ZR_1.25-BK). Signals were acquired with Doric Neuroscience Studio. For Ca^{2+} recordings, mice received unilateral FMN injections of AAV-DIO-GCaMP8m. For ACh recordings, mice received unilateral MVN injections of the AAV-ACh sensor, and the fiber was implanted ~200 µm above the injection site and secured with C&B Metabond® Quick Adhesive Cement System. Mice recovered for at least three weeks to allow stable expression. Both LEDs were operated in low-power mode with the driver current limited to 200

mA. Excitation power at the fiber tip was set to 6 µW at 405 nm and 12 µW at 460 nm, within the ~5–20 µW range commonly used in *in vivo* fiber photometry to maintain signal quality while minimizing photobleaching and phototoxicity (236,237). The two excitation wavelengths were sinusoidally modulated at distinct lock-in carrier frequencies (~208.6 Hz for 405 nm and ~572.2 Hz for 460 nm). Independent demodulation produced channels that were low-pass filtered at 12 Hz. The console sampled at 12 kS/s and saved decimated traces at ~60 Hz. Each recording day began with a 1 h high-power pre-bleaching step performed with the patch cord disconnected from the animal to reduce autofluorescence. After connecting to the implanted ferrule, LEDs remained on at recording intensity for 10 min to allow fluorescence and residual fiber signal to stabilize. Behavior was recorded under infrared illumination with an overhead ELP 2-MP USB camera (ELP-USBFHD01M-BL28IR).

8.1. Signal processing

The fiber photometry Doric files contain two lock-in channels (isosbestic reference and sensor channel). The recording sampling rate was estimated from the median inter-frame interval (~60 frames/s). The isosbestic and sensor traces were first smoothed with a 10-frame moving average to reduce high-frequency noise and then baseline-corrected using the airPLS algorithm ($\lambda = 5 \times 10^9$, order = 2, wep = 0.1, p = 0.5, 50 iterations). The baseline-subtracted traces were z-scored. To remove motion and bleaching components, the z-scored isosbestic signal was fitted to the z-scored sensor signal using non-negative robust linear regression (first-order polynomial), and the fitted reference trace was subtracted from the sensor trace to obtain a motion-corrected z-scored $\Delta F/F$ signal. Samples with extreme values ($|z| > 4$) were treated as artifacts and replaced by linear interpolation between neighboring valid points.

For area under the curve (AUC) calculations during beam traversal, behavioral HBT keypress events (start and end of the traversal) were recorded in Doric and exported. On the processed z-scored $\Delta F/F$ trace, the traversal window was defined between the keypress onset (mouse stepping onto the beam) and keypress offset (mouse

reaching the end of the beam). AUC during each traversal window was computed in MATLAB using the built-in trapezoidal numerical integration function (trapz), a common approach in FPS analyses that summarize fluorescence changes over defined behavioral epochs (238–240). To obtain a matched baseline, we took an equal-duration segment at the end of the recording, after the beam walk was completed, when the mouse remained quiet in its home cage. Recordings were routinely extended by at least 60 s after traversal to ensure a stable post-behavior period for baseline. AUC for this end segment was calculated with the same integration method and used as a time-matched baseline for each trial. These paired ΔAUC measures (traverse AUC - baseline AUC) were then used to quantify balance traversal-evoked changes.

To assess the effect of neuronal inhibition on ACh release in MVN during beam traversal, we applied the same AUC calculation workflow used for the calcium recordings. Trials were grouped by treatment day (saline or JHU) and ΔAUCs were compared between treatments. To test whether chemogenetic inhibition altered baseline ACh dynamics in MVN, we quantified baseline (non-traversal) AUC from the raw, non-z-scored ΔF/F signal rather than the processed z-scored traces. For each trial, we then extracted a time-fixed non-traversal baseline window and computed AUC over this window. Mean AUC was computed from the saline trials and used to normalize all baseline AUCs across both treatments. For each mouse, we calculated the mean normalized baseline AUC under saline and JHU and compared.

For peak signal calculation in the beam perturbation trials**,** we used the same processed z-score ΔF/F signal described above and aligned the signal to the perturbation time point (Arduino-triggered TTL pulse). We extracted a fixed pre-perturbation baseline window (over the 1s before perturbation) and a post-perturbation window (over the 2s after perturbation). Within each window, we calculated the peak z-score ΔF/F value, yielding a baseline peak and a post-perturbation peak for each trial. Peak values were then normalized by dividing each trial's perturbation peak by the mean baseline peak across all trials from all animals to obtain a fold-change measure.

In-cage signals were recorded (either FMN Ca^{2+} or MVN ACh) for 30 min while animal freely behaved in the cage. The *in vivo* and behavioral recordings were acquired concurrently. To align signals with DLC kinematic recordings, we first dynamically estimated the signal and video frame rates and linearly interpolated the ΔF/F trace onto the video frame timestamps. Within each accepted in-cage epoch (detected by DLC), we quantified AUC of a 5 s segment centered on the epoch midpoint. To construct a time-matched baseline, we drew random segments from the whole recording (5 s windows). For each random segment, AUC was computed identically. This yielded paired in-cage epoch and random epoch AUC values.

Correlations were computed by pairing a neural measure with one DLC-derived motor metric for each trial. Pearson correlation and bootstrap resampling were then used to quantify the relationship between these measures. For no-perturbation beam-traversal trials, traversal ΔAUC was paired with the z-scored relative posture-angle variance. For MVN ACh recordings, ACh ΔAUC was paired with the corresponding motor metric using the same approach. For perturbation HBT trials, normalized post-perturbation signal fold change was paired with the z-scored latency to postural recovery

9. Chemogenetic manipulation

For chemogenetic inhibition of FMN^{VIP} cells, mice expressing Cre-dependent hM4Di in FMN were tested using a two-day within-subject design. All behavioral assays (beam traversal and vertical pole) were performed twice per mouse with Day 1 and 2 receiving saline and DREADD agonist JHU37160, respectively. This order was kept constant across animals. Mice were briefly restrained for IP injection. On Day 1, animals received sterile saline (10 µl g^{-1}). On Day 2, mice received JHU37160 dihydrochloride (HelloBio) at 0.5 mg kg^{-1}, dissolved in saline containing ≤10% DMSO for solubility. The dose and timing were based on prior DREADD validation studies using the same ligand. Mice were returned to their home cage for 40 min after injection before behavioral testing to allow full activation of hM4Di signaling. For each assay, mice performed multiple trials per day as described for HBT and VPT behaviors (168).

10. Statistical analysis and data visualization

For all data acquisition and analyses in this study, experimenters were blinded to the manipulations. Statistical tests included two-sided Mann-Whitney U tests, unpaired t-tests with Welch's correction (for approximately normally distributed data as assessed by the Shapiro-Wilk test), Shapiro-Wilk tests for normality, non-parametric bootstrap resampling (with empirical confidence intervals and p values), and paired permutation tests for within-animal treatment comparisons. Data were visualized using scatter plots with group mean ± SEM, violin plots showing bootstrapped distributions, density histograms, cumulative distribution plots, polar (radar) plots for multi-trial spiral-motion profiles, success-rate bar/scatter plots, and donut charts, generated in GraphPad Prism, MATLAB, and Python.

References

1. McGraw Hill Medical [Internet]. 2021 [cited 2025 Dec 15]. Principles of Neural Science. Available from: https://neurology.mhmedical.com/content.aspx?sectionid=254326744&bookid=3024

2. Takakusaki K. Functional Neuroanatomy for Posture and Gait Control. J Mov Disord. 2017 Jan 18;10(1):1–17.

3. Akalu Y, Frazer AK, Howatson G, Pearce AJ, Siddique U, Rostami M, et al. Identifying the role of the reticulospinal tract for strength and motor recovery: A scoping review of nonhuman and human studies. Physiol Rep. 2023 July 20;11(14):e15765.

4. Highstein SM, Holstein GR. The Anatomical and Physiological Framework for Vestibular Prostheses. Anat Rec. 2012;295(11):2000–9.

5. McCall AA, Miller DM, Yates BJ. Descending Influences on Vestibulospinal and Vestibulosympathetic Reflexes. Front Neurol. 2017;8:112.

6. Morton SM, Bastian AJ. Cerebellar control of balance and locomotion. Neurosci Rev J Bringing Neurobiol Neurol Psychiatry. 2004 June;10(3):247–59.

7. Manto M, Bower JM, Conforto AB, Delgado-García JM, da Guarda SNF, Gerwig M, et al. Consensus paper: roles of the cerebellum in motor control--the diversity of ideas on cerebellar involvement in movement. Cerebellum Lond Engl. 2012 June;11(2):457–87.

8. Kiehn O. Decoding the organization of spinal circuits that control locomotion. Nat Rev Neurosci. 2016 Apr;17(4):224–38.

9. Angelaki DE, Cullen KE. Vestibular system: the many facets of a multimodal sense. Annu Rev Neurosci. 2008;31:125–50.

10. Goldberg JM, Cullen KE. Vestibular control of the head: possible functions of the vestibulocollic reflex. Exp Brain Res. 2011 May 1;210(3):331–45.

11. Gdowski GT, McCrea RA. Neck proprioceptive inputs to primate vestibular nucleus neurons. Exp Brain Res. 2000 Dec;135(4):511–26.

12. Medrea I, Cullen KE. Multisensory integration in early vestibular processing in mice: the encoding of passive vs. active motion. J Neurophysiol. 2013 Dec;110(12):2704–17.

13. Carriot J, Brooks JX, Cullen KE. Multimodal integration of self-motion cues in the vestibular system: active versus passive translations. J Neurosci Off J Soc Neurosci. 2013 Dec 11;33(50):19555–66.

14. Peterson BW. Reticulospinal projections to spinal motor nuclei. Annu Rev Physiol. 1979;41:127–40.

15. Brownstone RM, Chopek JW. Reticulospinal Systems for Tuning Motor Commands. Front Neural Circuits. 2018;12:30.

16. Matsuyama K, Drew T. Vestibulospinal and reticulospinal neuronal activity during locomotion in the intact cat. I. Walking on a level surface. J Neurophysiol. 2000 Nov;84(5):2237–56.

17. Wilson VJ, Peterson BW. Peripheral and central substrates of vestibulospinal reflexes. Physiol Rev. 1978 Jan;58(1):80–105.

18. Cullen KE. The vestibular system: multimodal integration and encoding of self-motion for motor control. Trends Neurosci. 2012 Mar;35(3):185–96.

19. Laurens J, Angelaki DE. A unified internal model theory to resolve the paradox of active versus passive self-motion sensation. eLife. 2017 Oct 18;6:e28074.

20. Yakusheva TA, Shaikh AG, Green AM, Blazquez PM, Dickman JD, Angelaki DE. Purkinje cells in posterior cerebellar vermis encode motion in an inertial reference frame. Neuron. 2007 June 21;54(6):973–85.

21. Assländer L, Peterka RJ. Sensory reweighting dynamics in human postural control. J Neurophysiol. 2014 May;111(9):1852–64.

22. Peterka RJ. Sensorimotor integration in human postural control. J Neurophysiol. 2002 Sept;88(3):1097–118.

23. Brandt T, Dieterich M, Danek A. Vestibular cortex lesions affect the perception of verticality. Ann Neurol. 1994 Apr;35(4):403–12.

24. MacNeilage PR, Ganesan N, Angelaki DE. Computational approaches to spatial orientation: from transfer functions to dynamic Bayesian inference. J Neurophysiol. 2008 Dec;100(6):2981–96.

25. Cullen KE, Roy JE. Signal processing in the vestibular system during active versus passive head movements. J Neurophysiol. 2004 May;91(5):1919–33.

26. Zhang L, Feldman AG, Levin MF. Vestibular and corticospinal control of human body orientation in the gravitational field. J Neurophysiol. 2018 Dec 1;120(6):3026–41.

27. Green AM, Angelaki DE. Internal models and neural computation in the vestibular system. Exp Brain Res. 2010 Jan;200(3–4):197–222.

28. Highstein SM, Holstein GR. The anatomy of the vestibular nuclei. Prog Brain Res. 2006;151:157–203.

29. Ishiyama G, Lopez I, Williamson R, Acuna D, Ishiyama A. Subcellular immunolocalization of NMDA receptor subunit NR1, 2A, 2B in the rat vestibular periphery. Brain Res. 2002 May 10;935(1–2):16–23.

30. Cullen KE. Vestibular processing during natural self-motion: implications for perception and action. Nat Rev Neurosci. 2019 June;20(6):346–63.

31. Kalluri R, Xue J, Eatock RA. Ion channels set spike timing regularity of mammalian vestibular afferent neurons. J Neurophysiol. 2010 Oct;104(4):2034–51.

32. Fernandez C, Goldberg JM. Physiology of peripheral neurons innervating semicircular canals of the squirrel monkey. II. Response to sinusoidal stimulation and dynamics of peripheral vestibular system. J Neurophysiol. 1971 July;34(4):661–75.

33. Sadeghi SG, Minor LB, Cullen KE. Response of vestibular-nerve afferents to active and passive rotations under normal conditions and after unilateral labyrinthectomy. J Neurophysiol. 2007 Feb;97(2):1503–14.

34. Moon Y, Sung J, An R, Hernandez ME, Sosnoff JJ. Gait variability in people with neurological disorders: A systematic review and meta-analysis. Hum Mov Sci. 2016 June;47:197–208.

35. Brodal A, Pompeiano O. The vestibular nuclei in cat. J Anat. 1957 Oct;91(4):438–54.

36. Vidal PP, Cullen K, Curthoys IS, Lac SD, Holstein G, Idoux E, et al. The Vestibular System. In: The Rat Nervous System: Fourth Edition [Internet]. Elsevier Inc.; 2015 [cited 2025 Dec 15]. p. 805–64. Available from: https://pure.johnshopkins.edu/en/publications/the-vestibular-system-3/

37. Barmack NH. Central vestibular system: vestibular nuclei and posterior cerebellum. Brain Res Bull. 2003 June 15;60(5–6):511–41.

38. Yoo H, Mihaila DM. Neuroanatomy, Vestibular Pathways. In: StatPearls [Internet]. Treasure Island (FL): StatPearls Publishing; 2025 [cited 2025 Dec 15]. Available from: http://www.ncbi.nlm.nih.gov/books/NBK557380/

39. Shinoda Y, Sugiuchi Y, Izawa Y, Hata Y. Long descending motor tract axons and their control of neck and axial muscles. Prog Brain Res. 2006;151:527–63.

40. Uchino Y, Kushiro K. Differences between otolith- and semicircular canal-activated neural circuitry in the vestibular system. Neurosci Res. 2011 Dec;71(4):315–27.

41. Murray AJ, Croce K, Belton T, Akay T, Jessell TM. Balance Control Mediated by Vestibular Circuits Directing Limb Extension or Antagonist Muscle Co-activation. Cell Rep. 2018 Jan 30;22(5):1325–38.

42. McCall AA, Miller DM, Balaban CD. Integration of vestibular and hindlimb inputs by vestibular nucleus neurons: multisensory influences on postural control. J Neurophysiol. 2021 Apr 1;125(4):1095–110.

43. Miller DM, Cotter LA, Gandhi NJ, Schor RH, Cass SP, Huff NO, et al. Responses of caudal vestibular nucleus neurons of conscious cats to rotations in vertical planes, before and after a bilateral vestibular neurectomy. Exp Brain Res. 2008 June;188(2):175–86.

44. Wada Y, Matsunaga T, Tsumoto T. Responses of neurons in the rat vestibular nuclei to static tilt stimulation. Acta Oto-Laryngol Suppl. 1991;481:224–6.

45. Lacava SA, Isilak N, Ranawat N, Katzke J, Hoedemaker JFH, Yoshida Y, et al. A vestibulospinal pathway for context-dependent motor control of the mouse tail. Cell Rep. 2025 July 22;44(7):115957.

46. Brandt T, Dieterich M. The vestibular cortex. Its locations, functions, and disorders. Ann N Y Acad Sci. 1999 May 28;871:293–312.

47. Karnath HO, Ferber S, Dichgans J. The neural representation of postural control in humans. Proc Natl Acad Sci U S A. 2000 Dec 5;97(25):13931–6.

48. Modianos DT, Pfaff DW. Brain stem and cerebellar lesions in female rats. I. Tests of posture and movement. Brain Res. 1976 Apr 16;106(1):31–46.

49. Tarlov E. The postural effect of lesions of the vestibular nuclei: a note on species differences among primates. J Neurosurg. 1969 Aug;31(2):187–95.

50. Montardy Q, Wei M, Liu X, Yi T, Zhou Z, Lai J, et al. Selective optogenetic stimulation of glutamatergic, but not GABAergic, vestibular nuclei neurons induces immediate and reversible postural imbalance in mice. Prog Neurobiol. 2021 Sept;204:102085.

51. Bartikofsky D, Hertz MJ, Bauer DS, Altschuler R, King WM, Stewart CE. Balance beam crossing times are slower after noise exposure in rats. Front Integr Neurosci [Internet]. 2023 July 11 [cited 2025 Dec 15];17. Available from: https://www.frontiersin.org/journals/integrative-neuroscience/articles/10.3389/fnint.2023.1196477/full

52. Dutheil S, Lacour M, Tighilet B. Neurogenic Potential of the Vestibular Nuclei and Behavioural Recovery Time Course in the Adult Cat Are Governed by the Nature of the Vestibular Damage. PLOS ONE. 2011 Aug 11;6(8):e22262.

53. Niwa M, Bauer D, Anderson M, Kanicki A, Keller K, Altschuler RA, et al. Noise-induced changes in rat head stability and orientation correlate with dysfunction of otolith irregular afferents. 2023 Oct 29 [cited 2025 Dec 15]; Available from: http://biorxiv.org/lookup/doi/10.1101/2023.10.26.563800

54. Rastoldo G, Marouane E, El Mahmoudi N, Péricat D, Bourdet A, Timon-David E, et al. Quantitative Evaluation of a New Posturo-Locomotor Phenotype in a Rodent Model of Acute Unilateral Vestibulopathy. Front Neurol [Internet]. 2020 June 5 [cited 2025 Dec 15];11. Available from: https://www.frontiersin.org/journals/neurology/articles/10.3389/fneur.2020.00505/full

55. Wang J, Tian E, Zhang Y, Guo Z, Chen J, Kong W, et al. The Effects of Unilateral Labyrinthectomy on Monoamine Neurotransmitters in the Medial Vestibular Nucleus of Rats. Biomolecules. 2023 Nov 10;13(11):1637.

56. Hamling KR, Harmon K, Kimura Y, Higashijima SI, Schoppik D. The Vestibulospinal Nucleus Is a Locus of Balance Development. J Neurosci Off J Soc Neurosci. 2024 July 24;44(30):e2315232024.

57. Smith PF, Zheng Y. From ear to uncertainty: vestibular contributions to cognitive function. Front Integr Neurosci. 2013 Nov 26;7:84.

58. Gottesman-Davis A, Shao M, Hirsch JC, Peusner KD. Electrophysiological properties of morphologically-identified medial vestibular nucleus neurons projecting to the abducens nucleus in the chick embryo. Neuroscience. 2011 Jan 13;172:494–509.

59. Kolkman KE, McElvain LE, Lac S du. Diverse Precerebellar Neurons Share Similar Intrinsic Excitability. J Neurosci. 2011 Nov 16;31(46):16665–74.

60. Perlmutter SI, Iwamoto Y, Baker JF, Peterson BW. Interdependence of spatial properties and projection patterns of medial vestibulospinal tract neurons in the cat. J Neurophysiol. 1998 Jan;79(1):270–84.

61. Shinoda Y, Ohgaki T, Sugiuchi Y, Futami T, Kakei S. Functional synergies of neck muscles innervated by single medial vestibulospinal axons. Ann N Y Acad Sci. 1992 May 22;656:507–18.

62. Roy JE, Cullen KE. Selective Processing of Vestibular Reafference during Self-Generated Head Motion. J Neurosci. 2001 Mar 15;21(6):2131–42.

63. Boyle R. Vestibulo-Spinal Pathways in Tetrapods. In: The Senses: A Comprehensive Reference [Internet]. Elsevier; 2020 [cited 2025 Dec 15]. p. 334–43. Available from: https://linkinghub.elsevier.com/retrieve/pii/B9780128093245238157

64. Wilson VJ, Boyle R, Fukushima K, Rose PK, Shinoda Y, Sugiuchi Y, et al. The vestibulocollic reflex. J Vestib Res Equilib Orientat. 1995;5(3):147–70.

65. Wilson VJ, Peterson BW, Fukushima K, Hirai N, Uchino Y. Analysis of vestibulocollic reflexes by sinusoidal polarization of vestibular afferent fibers. J Neurophysiol. 1979 Mar;42(2):331–46.

66. Guillaud E, Faure C, Doat E, Bouyer LJ, Guehl D, Cazalets JR. Ancestral persistence of vestibulospinal reflexes in axial muscles in humans. J Neurophysiol. 2020 May 1;123(5):2010–23.

67. Hess BJ. Vestibular signals in self-orientation and eye movement control. News Physiol Sci Int J Physiol Prod Jointly Int Union Physiol Sci Am Physiol Soc. 2001 Oct;16:234–8.

68. Wiboonsaksakul KP, Leavitt Brown OME, Cullen KE. Restoring vestibular function during natural self-motion: Progress and challenges. eLife. 2024 Dec 17;13:e99516.

69. Yoder RM, Taube JS. The vestibular contribution to the head direction signal and navigation. Front Integr Neurosci. 2014;8:32.

70. Zhang Y, Chu G, Leng Y, Lin X, Zhou H, Lu Y, et al. Parvalbumin-positive neurons in the medial vestibular nucleus contribute to vestibular compensation through commissural inhibition. Front Cell Neurosci [Internet]. 2023 Nov 8 [cited 2025 Dec 15];17. Available from: https://www.frontiersin.org/journals/cellular-neuroscience/articles/10.3389/fncel.2023.1260243/full

71. Bagnall MW, Stevens RJ, du Lac S. Transgenic mouse lines subdivide medial vestibular nucleus neurons into discrete, neurochemically distinct populations. J Neurosci Off J Soc Neurosci. 2007 Feb 28;27(9):2318–30.

72. Voogd J. What we do not know about cerebellar systems neuroscience. Front Syst Neurosci. 2014;8:227.

73. Carriot J, McAllister G, Hooshangnejad H, Mackrous I, Cullen KE, Chacron MJ. Sensory adaptation mediates efficient and unambiguous encoding of natural stimuli by vestibular thalamocortical pathways. Nat Commun. 2022 May 12;13(1):2612.

74. Ibitoye RT, Mallas EJ, Bourke NJ, Kaski D, Bronstein AM, Sharp DJ. The human vestibular cortex: functional anatomy of OP2, its connectivity and the effect of vestibular disease. Cereb Cortex N Y N 1991. 2023 Jan 5;33(3):567–82.

75. Indovina I, Bosco G, Riccelli R, Maffei V, Lacquaniti F, Passamonti L, et al. Structural connectome and connectivity lateralization of the multimodal vestibular cortical network. NeuroImage. 2020 Nov 15;222:117247.

76. zu Eulenburg P, Caspers S, Roski C, Eickhoff SB. Meta-analytical definition and functional connectivity of the human vestibular cortex. NeuroImage. 2012 Mar;60(1):162–9.

77. Baker SN. The primate reticulospinal tract, hand function and functional recovery. J Physiol. 2011;589(23):5603–12.

78. Boyne P, DiFrancesco M, Awosika OO, Williamson B, Vannest J. Mapping the human corticoreticular pathway with multimodal delineation of the gigantocellular reticular nucleus and high-resolution diffusion tractography. J Neurol Sci. 2022 Mar 15;434:120091.

79. Jang SH, Lee SJ. Corticoreticular Tract in the Human Brain: A Mini Review. Front Neurol [Internet]. 2019 Nov 12 [cited 2025 Dec 15];10. Available from: https://www.frontiersin.org/journals/neurology/articles/10.3389/fneur.2019.01188/full

80. Tellegen AJ, Arends JJ, Dubbeldam JL. The vestibular nuclei and vestibuloreticular connections in the mallard (Anas platyrhynchos L.). An anterograde and retrograde tracing study. Brain Behav Evol. 2001;58(4):205–17.

81. Dieringer N. "Vestibular compensation": neural plasticity and its relations to functional recovery after labyrinthine lesions in frogs and other vertebrates. Prog Neurobiol. 1995 June;46(2–3):97–129.

82. Grottel K, Jakielska-Bukowska D. The reticulovestibular projection in the rabbit: an experimental study with the retrograde horseradish peroxidase method. Neurosci Res. 1993 Dec;18(3):179–93.

83. Hernandez E, Das JM. Neuroanatomy, Nucleus Vestibular. In: StatPearls [Internet]. Treasure Island (FL): StatPearls Publishing; 2025 [cited 2025 Dec 15]. Available from: http://www.ncbi.nlm.nih.gov/books/NBK562261/

84. Bouvier G, Sanzeni A, Hamada E, Brunel N, Scanziani M. Inter- and intrahemispheric sources of vestibular signals to V1. Proc Natl Acad Sci U S A. 122(41):e2503181122.

85. Hayashi M, Hinckley CA, Driscoll SP, Moore NJ, Levine AJ, Hilde KL, et al. Graded Arrays of Spinal and Supraspinal V2a Interneuron Subtypes Underlie Forelimb and Hindlimb Motor Control. Neuron. 2018 Feb 21;97(4):869-884.e5.

86. Giolli RA, Blanks RHI, Lui F. The accessory optic system: basic organization with an update on connectivity, neurochemistry, and function. Prog Brain Res. 2006;151:407–40.

87. Simpson JI. The accessory optic system. Annu Rev Neurosci. 1984;7:13–41.

88. Büttner U, Büttner-Ennever JA. Present concepts of oculomotor organization. Prog Brain Res. 2006;151:1–42.

89. Ito M. Cerebellar control of the vestibulo-ocular reflex--around the flocculus hypothesis. Annu Rev Neurosci. 1982;5:275–96.

90. Thier P, Ilg UJ. The neural basis of smooth-pursuit eye movements. Curr Opin Neurobiol. 2005 Dec;15(6):645–52.

91. Bryan AS, Angelaki DE. Optokinetic and Vestibular Responsiveness in the Macaque Rostral Vestibular and Fastigial Nuclei. J Neurophysiol. 2008 Dec 10;101(2):714.

92. Dichgans J, Brandt T. Optokinetic motion sickness and pseudo-Coriolis effects induced by moving visual stimuli. Acta Otolaryngol (Stockh). 1973 Nov;76(5):339–48.

93. Waespe W, Henn V. Vestibular nuclei activity during optokinetic after-nystagmus (OKAN) in the alert monkey. Exp Brain Res. 1977 Nov 1;30(2):323–30.

94. Katzenberger B, Brosch F, Besnard S, Grill E. Chronic Vestibular Hypofunction Is Associated with Impaired Sleep: Results from the DizzyReg Patient Registry. J Clin Med. 2023 Sept 11;12(18):5903.

95. van Leeuwen RB, Schermer TR, Bienfait HP. The relationship between dizziness and sleep: a review of the literature. Front Neurol. 2024 Aug 29;15:1443827.

96. Nakatsuka D, Kanda T, Sato M, Ishikawa Y, Cherasse Y, Yanagisawa M. A novel GABAergic population in the medial vestibular nucleus maintains wakefulness and gates rapid eye movement sleep. iScience. 2024 Mar 15;27(3):109289.

97. Kong D, Kong L, Liu C, Wu Q, Wang J, Dai C. Commissural and monosynaptic inputs to medial vestibular nucleus GABAergic neurons in mice. Front Neurol [Internet]. 2024 Oct 8 [cited 2025 Dec 16];15. Available from: https://www.frontiersin.org/journals/neurology/articles/10.3389/fneur.2024.1484488/full

98. Holstein GR, Friedrich VLJ, Martinelli GP. Glutamate and GABA in Vestibulo-Sympathetic Pathway Neurons. Front Neuroanat [Internet]. 2016 Feb 8 [cited 2025 Dec 16];10. Available from: https://www.frontiersin.org/journals/neuroanatomy/articles/10.3389/fnana.2016.00007/full

99. Kong D, Kong L, Liu C, Wu Q, Wang J, Dai C. Commissural and monosynaptic inputs to medial vestibular nucleus GABAergic neurons in mice. Front Neurol. 2024 Oct 8;15:1484488.

100. Scudder CA, Fuchs AF. Physiological and behavioral identification of vestibular nucleus neurons mediating the horizontal vestibuloocular reflex in trained rhesus monkeys. J Neurophysiol. 1992 July;68(1):244–64.

101. Roy JE, Cullen KE. Dissociating self-generated from passively applied head motion: neural mechanisms in the vestibular nuclei. J Neurosci Off J Soc Neurosci. 2004 Mar 3;24(9):2102–11.

102. Roy JE, Cullen KE. Brain stem pursuit pathways: dissociating visual, vestibular, and proprioceptive inputs during combined eye-head gaze tracking. J Neurophysiol. 2003 July;90(1):271–90.

103. Zhang Y, Partsalis AM, Highstein SM. Properties of superior vestibular nucleus flocculus target neurons in the squirrel monkey. II. Signal components revealed by reversible flocculus inactivation. J Neurophysiol. 1995 June;73(6):2279–92.

104. Cullen KE. The neural encoding of self-generated and externally applied movement: implications for the perception of self-motion and spatial memory. Front Integr Neurosci [Internet]. 2014 Jan 13 [cited 2025 Dec 16];7. Available from: https://www.frontiersin.org/journals/integrative-neuroscience/articles/10.3389/fnint.2013.00108/full

105. Abe C, Yamaoka Y, Maejima Y, Mikami T, Yokota S, Yamanaka A, et al. VGLUT2-expressing neurons in the vestibular nuclear complex mediate gravitational stress-induced hypothermia in mice. Commun Biol. 2020 May 8;3(1):227.

106. Shi XB, Wang J, Li FT, Zhang YB, Qu WM, Dai CF, et al. Whole-brain monosynaptic outputs and presynaptic inputs of GABAergic neurons in the vestibular nuclei complex of mice. Front Neurosci [Internet]. 2022 Aug 26 [cited 2025 Dec 16];16. Available from: https://www.frontiersin.org/journals/neuroscience/articles/10.3389/fnins.2022.982596/full

107. Barmack NH, Baughman RW, Eckenstein FP, Shojaku H. Secondary vestibular cholinergic projection to the cerebellum of rabbit and rat as revealed by choline acetyltransferase immunohistochemistry, retrograde and orthograde tracers. J Comp Neurol. 1992 Mar 15;317(3):250–70.

108. Zhou W, Zhou LQ, Shi H, Leng YM, Liu B, Zhang SL, et al. Expression of glycine receptors and gephyrin in rat medial vestibular nuclei and flocculi following unilateral labyrinthectomy. Int J Mol Med. 2016 Nov;38(5):1481–9.

109. Gliddon CM, Darlington CL, Smith PF. GABAergic systems in the vestibular nucleus and their contribution to vestibular compensation. Prog Neurobiol. 2005 Jan;75(1):53–81.

110. Peusner K. Basic Concepts in Understanding Recovery of Function in Vestibular Reflex Networks during Vestibular Compensation. Front Neurol [Internet]. 2012 Feb 20 [cited 2025 Dec 16];3. Available from: https://www.frontiersin.org/journals/neurology/articles/10.3389/fneur.2012.00017/full

111. R HS, Hk T, Js B, Dm B. Type B GABA receptors contribute to the restoration of balance during vestibular compensation in mice. Neuroscience [Internet]. 2010 Nov 8 [cited 2025 Dec 16];169(1). Available from: https://pubmed.ncbi.nlm.nih.gov/20394801

112. Yates BJ, Bolton PS, Macefield VG. Vestibulo-sympathetic responses. Compr Physiol. 2014 Apr;4(2):851–87.

113. Bergquist F, Ludwig M, Dutia MB. Role of the commissural inhibitory system in vestibular compensation in the rat. J Physiol. 2008 Sept 15;586(18):4441–52.

114. Furuya N, Yabe T, Koizumi T. Neurotransmitters in the vestibular commissural system of the cat. Ann N Y Acad Sci. 1992 May 22;656:594–601.

115. Malinvaud D, Vassias I, Reichenberger I, Rössert C, Straka H. Functional Organization of Vestibular Commissural Connections in Frog. J Neurosci. 2010 Mar 3;30(9):3310–25.

116. Bagnall MW, Zingg B, Sakatos A, Moghadam SH, Zeilhofer HU, Lac S du. Glycinergic Projection Neurons of the Cerebellum. J Neurosci. 2009 Aug 12;29(32):10104–10.

117. Halberstadt AL, Balaban CD. Organization of projections from the raphe nuclei to the vestibular nuclei in rats. Neuroscience. 2003;120(2):573–94.

118. Han L, Wu KLK, Kwan PY, Chua OWH, Shum DKY, Chan YS. 5-HT1A receptor-mediated attenuation of synaptic transmission in rat medial vestibular nucleus impacts on vestibular-related motor function. J Physiol. 2021 Jan;599(1):253–67.

119. Zhang XY, Yu L, Zhuang QX, Peng SY, Zhu JN, Wang JJ. Postsynaptic mechanisms underlying the excitatory action of histamine on medial vestibular nucleus neurons in rats. Br J Pharmacol. 2013 Sept;170(1):156–69.

120. Witts EC, Mathews MA, Murray AJ. The locus coeruleus directs sensory-motor reflex amplitude across environmental contexts. Curr Biol. 2023 Nov 6;33(21):4679-4688.e3.

121. Woolf NJ, Butcher LL. Cholinergic systems in the rat brain: IV. Descending projections of the pontomesencephalic tegmentum. Brain Res Bull. 1989 Dec;23(6):519–40.

122. Zhu Y, Chen SR, Pan HL. Muscarinic receptor subtypes differentially control synaptic input and excitability of cerebellum-projecting medial vestibular nucleus neurons. J Neurochem. 2016 Apr;137(2):226–39.

123. Deliagina TG, Beloozerova IN, Zelenin PV, Orlovsky GN. Spinal and supraspinal postural networks. Brain Res Rev. 2008 Jan;57(1):212–21.

124. Iles JF, Ali AS, Savic G. Vestibular-evoked muscle responses in patients with spinal cord injury. Brain J Neurol. 2004 July;127(Pt 7):1584–92.

125. Liechti M, Müller R, Lam T, Curt A. Vestibulospinal responses in motor incomplete spinal cord injury. Clin Neurophysiol Off J Int Fed Clin Neurophysiol. 2008 Dec;119(12):2804–12.

126. Strupp M, Dlugaiczyk J, Bettina Ertl-Wagner B, Rujescu D, Westhofen M, Dieterich M. Vestibular Disorders. Dtsch Ärztebl Int. 2020 Apr;117(17):300–10.

127. Chow MR, Ayiotis AI, Schoo DP, Gimmon Y, Lane KE, Morris BJ, et al. Posture, Gait, Quality of Life, and Hearing with a Vestibular Implant. N Engl J Med. 2021 Feb 10;384(6):521–32.

128. Hall CD, Goebel JA, al et. Vestibular rehabilitation for peripheral vestibular hypofunction: An updated clinical practice guideline from the Academy of Neurologic Physical Therapy of the American Physical Therapy Association. J Neurol Phys Ther. 2022 Apr 1;46(2):118–77.

129. Tenney AP, Livet J, Belton T, Prochazkova M, Pearson EM, Whitman MC, et al. Etv1 Controls the Establishment of Non-overlapping Motor Innervation of Neighboring Facial Muscles during Development. Cell Rep. 2019 Oct 8;29(2):437-452.e4.

130. Sürmeli G, Akay T, Ippolito G, Tucker PW, Jessell TM. Patterns of Spinal Sensory-Motor Connectivity Prescribed by a Dorsoventral Positional Template. Cell. 2011 Oct 28;147(3):653–65.

131. Sofroniew NJ, Vlasov YA, Hires SA, Freeman J, Svoboda K. Neural coding in barrel cortex during whisker-guided locomotion. Nelson SB, editor. eLife. 2015 Dec 23;4:e12559.

132. Warren RA, Zhang Q, Hoffman JR, Li EY, Hong YK, Bruno RM, et al. A rapid whisker-based decision underlying skilled locomotion in mice. Goldberg JH, Calabrese RL, Goldberg JH, editors. eLife. 2021 Jan 11;10:e63596.

133. Arakawa H, Erzurumlu RS. Role of whiskers in sensorimotor development of C57BL/6 mice. Behav Brain Res. 2015;287:146–55.

134. Grant RA, Mitchinson B, Prescott TJ. The development of whisker control in rats in relation to locomotion. Dev Psychobiol. 2012 Mar;54(2):151–68.

135. Bergmann R, Sehara K, Dominiak SE, Kremkow J, Larkum ME, Sachdev RNS. Coordination between Eye Movement and Whisking in Head-Fixed Mice Navigating a Plus Maze. eNeuro. 2022;9(4):ENEURO.0089-22.2022.

136. Ichikawa T, Shimizu T. Organization of choline acetyltransferase-containing structures in the cranial nerve motor nuclei and spinal cord of the monkey. Brain Res. 1998 Jan 1;779(1):96–103.

137. Fong AY, Stornetta RL, Foley CM, Potts JT. Immunohistochemical localization of GAD67-expressing neurons and processes in the rat brainstem: Subregional distribution in the nucleus tractus solitarius. J Comp Neurol. 2005 Dec 12;493(2):274–90.

138. Gotts J, Atkinson L, Edwards IJ, Yanagawa Y, Deuchars SA, Deuchars J. Co-expression of GAD67 and choline acetyltransferase reveals a novel neuronal phenotype in the mouse medulla oblongata. Auton Neurosci. 2015 Dec;193:22–30.

139. Li YQ, Takada M, Kaneko T, Mizuno N. Distribution of GABAergic and glycinergic premotor neurons projecting to the facial and hypoglossal nuclei in the rat. J Comp Neurol. 1997 Feb 10;378(2):283–94.

140. Li C, Guan Z, Chan Y, Zheng Y. Projections from facial nucleus interneurons to the respiratory groups of brainstem in the rat. Neurosci Lett. 2004 Sept 16;368(1):25–8.

141. Isokawa-Akesson M, Komisaruk BR. Difference in projections to the lateral and medial facial nucleus: anatomically separate pathways for rhythmical vibrissa movement in rats. Exp Brain Res. 1987;65(2):385–98.

142. Mercer Lindsay N, Knutsen PM, Lozada AF, Gibbs D, Karten HJ, Kleinfeld D. Orofacial Movements Involve Parallel Corticobulbar Projections from Motor Cortex to Trigeminal Premotor Nuclei. Neuron. 2019 Nov 20;104(4):765-780.e3.

143. Meincke J, Hewitt M, Reischl M, Rupp R, Schmidt-Samoa C, Liebetanz D. Cortical representation of auricular muscles in humans: A robot-controlled TMS mapping and fMRI study. PLOS ONE. 2018 July 27;13(7):e0201277.

144. Morecraft RJ, Binneboese A, Stilwell-Morecraft KS, Ge J. Localization of orofacial representation in the corona radiata, internal capsule and cerebral peduncle in Macaca mulatta. J Comp Neurol. 2017 Nov 1;525(16):3429–57.

145. Morecraft RJ, Louie JL, Herrick JL, Stilwell-Morecraft KS. Cortical innervation of the facial nucleus in the non-human primate: A new interpretation of the effects of stroke and related subtotal brain trauma on the muscles of facial expression. Brain. 2001 Jan 1;124(1):176–208.

146. Müri RM. Cortical control of facial expression. J Comp Neurol. 2016;524(8):1578–85.

147. Kubin L. Neural Control of the Upper Airway: Respiratory and State-Dependent Mechanisms. Compr Physiol. 2016 Sept 15;6(4):1801–50.

148. Mogoseanu D, Smith AD, Bolam JP. Monosynaptic innervation of facial motoneurones by neurones of the parvicellular reticular formation. Exp Brain Res. 1994 Oct 1;101(3):427–38.

149. Ter Horst GJ, Copray JC, Liem RS, Van Willigen JD. Projections from the rostral parvocellular reticular formation to pontine and medullary nuclei in the rat: involvement in autonomic regulation and orofacial motor control. Neuroscience. 1991;40(3):735–58.

150. Cattaneo L, Pavesi G. The facial motor system. Neurosci Biobehav Rev. 2014 Jan 1;38:135–59.

151. Lam KS. Vasoactive intestinal peptide in the hypothalamus and pituitary. Neuroendocrinology. 1991;53 Suppl 1:45–51.

152. Rudy B, Fishell G, Lee S, Hjerling-Leffler J. Three Groups of Interneurons Account for Nearly 100% of Neocortical GABAergic Neurons. Dev Neurobiol. 2011 Jan 1;71(1):45–61.

153. Tremblay R, Lee S, Rudy B. GABAergic interneurons in the neocortex: From cellular properties to circuits. Neuron. 2016 July 20;91(2):260–92.

154. ISH Data :: Allen Brain Atlas: Mouse Brain [Internet]. [cited 2025 Dec 16]. Available from: https://mouse.brain-map.org/search/show?page_num=0&page_size=27&no_paging=false&exact_match=false&search_term=Vip&search_type=gene

155. Uhlén M, Fagerberg L, Hallström BM, Lindskog C, Oksvold P, Mardinoglu A, et al. Tissue-based map of the human proteome. Science. 2015 Jan 23;347(6220):1260419.

156. Angelaki DE, Cullen KE. Vestibular system: the many facets of a multimodal sense. Annu Rev Neurosci. 2008;31:125–50.

157. Harvey RJ, De'sperati C, Strata P. The Early Phase of Horizontal Optokinetic Responses in the Pigmented Rat and the Effects of Lesions of the Visual Cortex. Vision Res. 1997 June 1;37(12):1615–25.

158. van Alphen B, Winkelman BHJ, Frens MA. Three-Dimensional Optokinetic Eye Movements in the C57BL/6J Mouse. Invest Ophthalmol Vis Sci. 2010 Jan 1;51(1):623–30.

159. Beraneck M, Cullen KE. Activity of vestibular nuclei neurons during vestibular and optokinetic stimulation in the alert mouse. J Neurophysiol. 2007 Sept;98(3):1549–65.

160. Murphy GJ, Du Lac S. Postnatal development of spike generation in rat medial vestibular nucleus neurons. J Neurophysiol. 2001 May;85(5):1899–906.

161. Matsuura K, Kabuto H, Makino H, Ogawa N. Pole test is a useful method for evaluating the mouse movement disorder caused by striatal dopamine depletion. J Neurosci Methods. 1997 Apr 25;73(1):45–8.

162. Ruan J, Yao Y. Behavioral tests in rodent models of stroke. Brain Hemorrhages. 2020 Dec;1(4):171–84.

163. Grillner S, Hongo T, Lund S. The vestibulospinal tract. Effects on alpha-motoneurones in the lumbosacral spinal cord in the cat. Exp Brain Res. 1970;10(1):94–120.

164. Deacon RMJ. Measuring motor coordination in mice. J Vis Exp JoVE. 2013 May 29;(75):e2609.

165. Eltokhi A, Kurpiers B, Pitzer C. Comprehensive characterization of motor and coordination functions in three adolescent wild-type mouse strains. Sci Rep. 2021 Mar 22;11(1):6497.

166. Seibenhener ML, Wooten MC. Use of the Open Field Maze to measure locomotor and anxiety-like behavior in mice. J Vis Exp JoVE. 2015 Feb 6;(96):e52434.

167. Poth KM, Texakalidis P, Boulis NM. Chemogenetics: Beyond Lesions and Electrodes. Neurosurgery. 2021 Apr 29;89(2):185–95.

168. Bonaventura J, Eldridge MAG, Hu F, Gomez JL, Sanchez-Soto M, Abramyan AM, et al. High-potency ligands for DREADD imaging and activation in rodents and monkeys. Nat Commun. 2019 Oct 11;10(1):4627.

169. Kielbinski M, Bernacka J. Fiber photometry in neuroscience research: principles, applications, and future directions. Pharmacol Rep. 2024;76(6):1242–55.

170. Simpson EH, Akam T, Patriarchi T, Blanco-Pozo M, Burgeno LM, Mohebi A, et al. Lights, fiber, action! A primer on *in vivo* fiber photometry. Neuron. 2024 Mar 6;112(5):718–39.

171. Zhang Y, Rózsa M, Liang Y, Bushey D, Wei Z, Zheng J, et al. Fast and sensitive GCaMP calcium indicators for imaging neural populations. Nature. 2023 Mar;615(7954):884–91.

172. Lewis KT, Oles LR, MacDougald OA. Tetracycline response element driven Cre causes ectopic recombinase activity independent of transactivator element. Mol Metab. 2022 July 1;61:101501.

173. Kumoi K, Saito N, Tanaka C. Immunohistochemical localization of γ-aminobutyric acid- and aspartate-containing neurons in the guinea pig vestibular nuclei. Brain Res. 1987 July 21;416(1):22–33.

174. Saito K, Kakizaki T, Hayashi R, Nishimaru H, Furukawa T, Nakazato Y, et al. The physiological roles of vesicular GABA transporter during embryonic development: a study using knockout mice. Mol Brain. 2010 Dec 30;3(1):40.

175. Saunders A, Macosko EZ, Wysoker A, Goldman M, Krienen FM, de Rivera H, et al. Molecular Diversity and Specializations among the Cells of the Adult Mouse Brain. Cell. 2018 Aug 9;174(4):1015-1030.e16.

176. Bellavance MA, Takatoh J, Lu J, Demers M, Kleinfeld D, Wang F, et al. Parallel Inhibitory and Excitatory Trigemino-Facial Feedback Circuitry for Reflexive Vibrissa Movement. Neuron. 2017 Aug 2;95(3):673-682.e4.

177. Jing M, Li Y, Zeng J, Huang P, Skirzewski M, Kljakic O, et al. An optimized acetylcholine sensor for monitoring in vivo cholinergic activity. Nat Methods. 2020 Nov;17(11):1139–46.

178. Kügler S, Lingor P, Schöll U, Zolotukhin S, Bähr M. Differential transgene expression in brain cells in vivo and in vitro from AAV-2 vectors with small transcriptional control units. Virology. 2003 June 20;311(1):89–95.

179. Wang HL, Morales M. Pedunculopontine and laterodorsal tegmental nuclei contain distinct populations of cholinergic, glutamatergic and GABAergic neurons in the rat. Eur J Neurosci. 2009 Jan;29(2):340–58.

180. Puchades MA, Csucs G, Ledergerber D, Leergaard TB, Bjaalie JG. Spatial registration of serial microscopic brain images to three-dimensional reference atlases with the QuickNII tool. PLOS ONE. 2019 May 29;14(5):e0216796.

181. Berg S, Kutra D, Kroeger T, Straehle CN, Kausler BX, Haubold C, et al. ilastik: interactive machine learning for (bio)image analysis. Nat Methods. 2019 Dec;16(12):1226–32.

182. Sommer CM, Straehle C, Köthe U, Hamprecht FA. Ilastik: Interactive learning and segmentation toolkit. 2011 IEEE Int Symp Biomed Imaging Nano Micro [Internet]. 2011 [cited 2025 Dec 16]; Available from: https://research-explorer.ista.ac.at/record/9943

183. Martin EM, Pavlides C, Pfaff D. Multimodal Sensory Responses of Nucleus Reticularis Gigantocellularis and the Responses' Relation to Cortical and Motor Activation. J Neurophysiol. 2010 May;103(5):2326–38.

184. Takakusaki K. Functional Neuroanatomy for Posture and Gait Control. J Mov Disord. 2017 Jan;10(1):1–17.

185. Wilson VJ, Peterson BW. Vestibulospinal and Reticulospinal Systems. Compr Physiol. 1981;1981(12S2):667–702.

186. Pfeffer CK. Inhibitory Neurons: Vip Cells Hit the Brake on Inhibition. Curr Biol. 2014 Jan 6;24(1):R18–20.

187. Apicella A junior, Marchionni I. VIP-Expressing GABAergic Neurons: Disinhibitory vs. Inhibitory Motif and Its Role in Communication Across Neocortical Areas. Front Cell Neurosci [Internet]. 2022 Feb 10 [cited 2025 Dec 16];16. Available from: https://www.frontiersin.org/journals/cellular-neuroscience/articles/10.3389/fncel.2022.811484/full

188. Goyer D, Silveira MA, George AP, Beebe NL, Edelbrock RM, Malinski PT, et al. A novel class of inferior colliculus principal neurons labeled in vasoactive intestinal peptide-Cre mice. King AJ, Lee C, Oliver D, Borst JGG, editors. eLife. 2019 Apr 18;8:e43770.

189. Urrutia-Piñones J, Morales-Moraga C, Sanguinetti-González N, Escobar AP, Chiu CQ. Long-Range GABAergic Projections of Cortical Origin in Brain Function. Front Syst Neurosci. 2022 Mar 22;16:841869.

190. Melzer S, Monyer H. Diversity and function of corticopetal and corticofugal GABAergic projection neurons. Nat Rev Neurosci. 2020 Sept;21(9):499–515.

191. Melzer S, Gil M, Koser DE, Michael M, Huang KW, Monyer H. Distinct Corticostriatal GABAergic Neurons Modulate Striatal Output Neurons and Motor Activity. Cell Rep. 2017 May 2;19(5):1045–55.

192. Melzer S, Michael M, Caputi A, Eliava M, Fuchs EC, Whittington MA, et al. Long-Range–Projecting GABAergic Neurons Modulate Inhibition in Hippocampus and Entorhinal Cortex. Science. 2012 Mar 23;335(6075):1506–10.

193. Rock C, Zurita H, Wilson C, Apicella A junior. An inhibitory corticostriatal pathway. eLife. 5:e15890.

194. Goyer D, Silveira MA, George AP, Beebe NL, Edelbrock RM, Malinski PT, et al. A novel class of inferior colliculus principal neurons labeled in vasoactive intestinal peptide-Cre mice. eLife. 8:e43770.

195. Krabbe S, Paradiso E, d'Aquin S, Bitterman Y, Courtin J, Xu C, et al. Adaptive disinhibitory gating by VIP interneurons permits associative learning. Nat Neurosci. 2019 Nov;22(11):1834–43.

196. Lee SH, Cox CL. Vasoactive intestinal peptide selectively depolarizes thalamic relay neurons and attenuates intrathalamic rhythmic activity. J Neurophysiol. 2003 Aug;90(2):1224–34.

197. Palkovits M, Léránth C, Eiden LE, Rotsztejn W, Williams TH. Intrinsic vasoactive intestinal polypeptide (VIP)-containing neurons in the baroreceptor nucleus of the solitary tract in rat. Brain Res. 1982 July 29;244(2):351–5.

198. Zhang Y, Huang X, Xin WJ, He S, Deng J, Ruan X. Somatostatin Neurons from Periaqueductal Gray to Medulla Facilitate Neuropathic Pain in Male Mice. J Pain. 2023 June;24(6):1020–9.

199. Wallace ML, Saunders A, Huang KW, Philson AC, Goldman M, Macosko EZ, et al. Genetically Distinct Parallel Pathways in the Entopeduncular Nucleus for Limbic and Sensorimotor Output of the Basal Ganglia. Neuron. 2017 Apr 5;94(1):138-152.e5.

200. Granger AJ, Wang W, Robertson K, El-Rifai M, Zanello AF, Bistrong K, et al. Cortical ChAT+ neurons co-transmit acetylcholine and GABA in a target- and brain-region-specific manner. Brown SP, Swartz KJ, McBain CJ, Shabel S, editors. eLife. 2020 July 2;9:e57749.

201. von Engelhardt J, Eliava M, Meyer AH, Rozov A, Monyer H. Functional Characterization of Intrinsic Cholinergic Interneurons in the Cortex. J Neurosci. 2007 May 23;27(21):5633–42.

202. Morecraft RJ, Louie JL, Herrick JL, Stilwell-Morecraft KS. Cortical innervation of the facial nucleus in the non-human primate: a new interpretation of the effects of stroke and related subtotal brain trauma on the muscles of facial expression. Brain J Neurol. 2001 Jan;124(Pt 1):176–208.

203. Urban PP, Wicht S, Vucorevic G, Fitzek S, Marx J, Thömke F, et al. The course of corticofacial projections in the human brainstem. Brain. 2001 Sept 1;124(9):1866–76.

204. Hinrichsen CF, Watson CD. Brain stem projections to the facial nucleus of the rat. Brain Behav Evol. 1983;22(2–3):153–63.

205. Travers JB, Norgren R. Afferent projections to the oral motor nuclei in the rat. J Comp Neurol. 1983 Nov 1;220(3):280–98.

206. Takatoh J, Nelson A, Zhou X, Bolton MM, Ehlers MD, Arenkiel BR, et al. New Modules Are Added to Vibrissal Premotor Circuitry with the Emergence of Exploratory Whisking. Neuron. 2013 Jan 23;77(2):346–60.

207. Cenciarini M, Peterka RJ. Stimulus-dependent changes in the vestibular contribution to human postural control. J Neurophysiol. 2006 May;95(5):2733–50.

208. Peterka RJ. Sensorimotor integration in human postural control. J Neurophysiol. 2002 Sept;88(3):1097–118.

209. Baloh RW, Jacobson KM, Beykirch K, Honrubia V. Static and dynamic posturography in patients with vestibular and cerebellar lesions. Arch Neurol. 1998 May;55(5):649–54.

210. McCall AA, Miller DM, Yates BJ. Descending Influences on Vestibulospinal and Vestibulosympathetic Reflexes. Front Neurol. 2017;8:112.

211. Naranjo EN, Allum JHJ, Inglis JT, Carpenter MG. Increased gain of vestibulospinal potentials evoked in neck and leg muscles when standing under height-induced postural threat. Neuroscience. 2015 May 7;293:45–54.

212. Scammell TE, Arrigoni E, Lipton JO. Neural Circuitry of Wakefulness and Sleep. Neuron. 2017 Feb 22;93(4):747–65.

213. Van Dort CJ, Zachs DP, Kenny JD, Zheng S, Goldblum RR, Gelwan NA, et al. Optogenetic activation of cholinergic neurons in the PPT or LDT induces REM sleep. Proc Natl Acad Sci U S A. 2015 Jan 13;112(2):584–9.

214. Zhang Y, Yanagawa Y, Saito Y. Nicotinic acetylcholine receptor-mediated responses in medial vestibular and prepositus hypoglossi nuclei neurons showing distinct neurotransmitter phenotypes. J Neurophysiol. 2016 June 1;115(5):2649–57.

215. Turek JW, Kang CH, Campbell JE, Arneric SP, Sullivan JP. A sensitive technique for the detection of the alpha 7 neuronal nicotinic acetylcholine receptor antagonist, methyllycaconitine, in rat plasma and brain. J Neurosci Methods. 1995;61(1–2):113–8.

216. Caulino-Rocha A, Rodrigues NC, Ribeiro JA, Cunha-Reis D. Endogenous VIP VPAC1 Receptor Activation Modulates Hippocampal Theta Burst Induced LTP: Transduction Pathways and GABAergic Mechanisms. Biology. 2022 Apr 20;11(5):627.

217. Camp AJ, Callister RJ, Brichta AM. Inhibitory synaptic transmission differs in mouse type A and B medial vestibular nucleus neurons in vitro. J Neurophysiol. 2006 May;95(5):3208–18.

218. Gliddon CM, Darlington CL, Smith PF. GABAergic systems in the vestibular nucleus and their contribution to vestibular compensation. Prog Neurobiol. 2005 Jan;75(1):53–81.

219. Hui Y, Zheng X, Zhang H, Li F, Yu G, Li J, et al. Strategies for Targeting Neural Circuits: How to Manipulate Neurons Using Virus Vehicles. Front Neural Circuits [Internet]. 2022 Apr 29 [cited 2025 Dec 16];16. Available from: https://www.frontiersin.org/journals/neural-circuits/articles/10.3389/fncir.2022.882366/full

220. Li E, Guo J, Oh SJ, Luo Y, Oliveros HC, Du W, et al. Anterograde transneuronal tracing and genetic control with engineered yellow fever vaccine YFV-17D. Nat Methods. 2021 Dec;18(12):1542–51.

221. Qiu L, Zhang B, Gao Z. Lighting Up Neural Circuits by Viral Tracing. Neurosci Bull. 2022 Nov 1;38(11):1383–96.

222. Tsai NY, Wang F, Toma K, Yin C, Takatoh J, Pai EL, et al. Trans-Seq maps a selective mammalian retinotectal synapse instructed by Nephronectin. Nat Neurosci. 2022 May;25(5):659–74.

223. Xu X, Holmes TC, Luo MH, Beier KT, Horwitz GD, Zhao F, et al. Viral vectors for neural circuit mapping and recent advances in trans-synaptic anterograde tracers. Neuron. 2020 Sept 23;107(6):1029–47.

224. Zingg B, Dong HW, Tao HW, Zhang LI. Application of AAV1 for Anterograde Transsynaptic Circuit Mapping and Input-Dependent Neuronal Cataloging. Curr Protoc. 2022 Jan;2(1):e339.

225. Groeneboom NE, Yates SC, Puchades MA, Bjaalie JG. Nutil: A Pre- and Post-processing Toolbox for Histological Rodent Brain Section Images. Front Neuroinformatics [Internet]. 2020 Aug 21 [cited 2025 Dec 16];14. Available from: https://www.frontiersin.org/journals/neuroinformatics/articles/10.3389/fninf.2020.00037/full

226. Yates SC, Groeneboom NE, Coello C, Lichtenthaler SF, Kuhn PH, Demuth HU, et al. QUINT: Workflow for Quantification and Spatial Analysis of Features in Histological Images From Rodent Brain. Front Neuroinformatics [Internet]. 2019 Dec 3 [cited 2025 Dec 16];13. Available from: https://www.frontiersin.org/journals/neuroinformatics/articles/10.3389/fninf.2019.00075/full

227. Schindelin J, Arganda-Carreras I, Frise E, Kaynig V, Longair M, Pietzsch T, et al. Fiji: an open-source platform for biological-image analysis. Nat Methods. 2012 June 28;9(7):676–82.

228. Kraeuter AK, Guest PC, Sarnyai Z. The Open Field Test for Measuring Locomotor Activity and Anxiety-Like Behavior. Methods Mol Biol Clifton NJ. 2019;1916:99–103.

229. Noldus LP, Spink AJ, Tegelenbosch RA. EthoVision: a versatile video tracking system for automation of behavioral experiments. Behav Res Methods Instrum Comput J Psychon Soc Inc. 2001 Aug;33(3):398–414.

230. Tatem KS, Quinn JL, Phadke A, Yu Q, Gordish-Dressman H, Nagaraju K. Behavioral and locomotor measurements using an open field activity monitoring system for skeletal muscle diseases. J Vis Exp JoVE. 2014 Sept 29;(91):51785.

231. Sutton ER, Beauvais A, Yaworski R, De Repentigny Y, Reilly A, Alves de Almeida MM, et al. Liver SMN restoration rescues the *Smn*2B/- mouse model of spinal muscular atrophy. eBioMedicine. 2024 Dec 1;110:105444.

232. Tillotson R, Yan K, Ruston J, DeYoung T, Córdova A, Turcotte-Cardin V, et al. A new mouse model of ATR-X syndrome carrying a common patient mutation exhibits neurological and morphological defects. Hum Mol Genet. 2023 Aug 1;32(15):2485–501.

233. Cabe PA, Tilson HA, Mitchell CL, Dennis R. A simple recording grip strength device. Pharmacol Biochem Behav. 1978 Jan;8(1):101–2.

234. IMPReSS | International Mouse Phenotyping Resource of Standardised Screens [Internet]. [cited 2025 Dec 16]. Grip Strength Protocol. Available from: https://www.mousephenotype.org/impress/ProcedureInfo?action=list&procID=468

235. Mathis A, Mamidanna P, Cury KM, Abe T, Murthy VN, Mathis MW, et al. DeepLabCut: markerless pose estimation of user-defined body parts with deep learning. Nat Neurosci. 2018 Sept;21(9):1281–9.

236. Andersen M, Tsopanidou A, Radovanovic T, Compere VN, Hauglund N, Nedergaard M, et al. Using Fiber Photometry in Mice to Estimate Fluorescent Biosensor Levels During Sleep. Bio-Protoc. 2023 Aug 5;13(15):e4734.

237. Zhou ZC, Gordon-Fennell A, Piantadosi SC, Ji N, Smith SL, Bruchas MR, et al. Deep-brain optical recording of neural dynamics during behavior. Neuron. 2023 Dec 6;111(23):3716–38.

238. Sherathiya VN, Schaid MD, Seiler JL, Lopez GC, Lerner TN. GuPPy, a Python toolbox for the analysis of fiber photometry data. Sci Rep. 2021 Dec 20;11(1):24212.

239. Walle R, Petitbon A, Fois GR, Varin C, Montalban E, Hardt L, et al. Nucleus accumbens D1- and D2-expressing neurons control the balance between feeding and activity-mediated energy expenditure. Nat Commun. 2024 Mar 21;15(1):2543.

240. Zhou WL, Kim K, Ali F, Pittenger ST, Calarco CA, Mineur YS, et al. Activity of a direct VTA to ventral pallidum GABA pathway encodes unconditioned reward value and sustains motivation for reward. Sci Adv. 8(42):eabm5217.